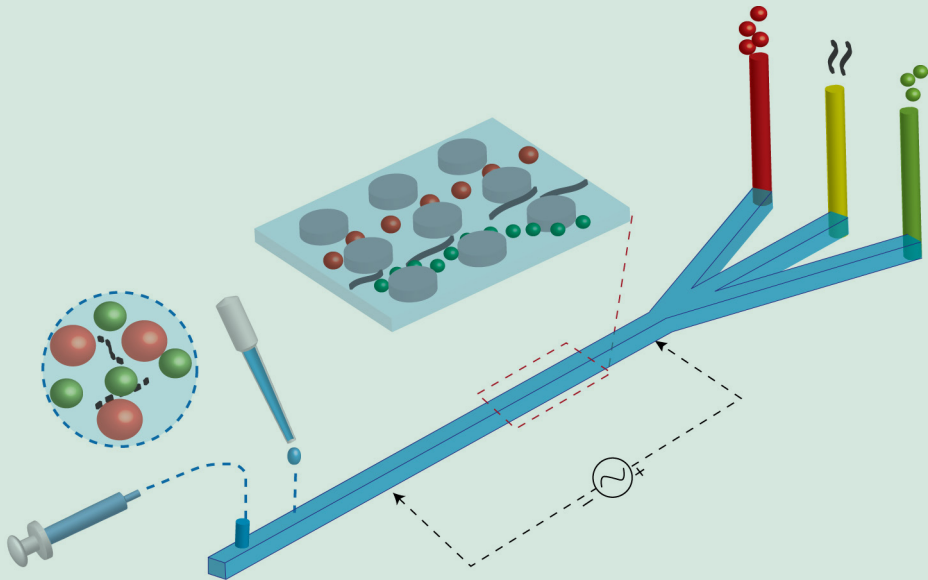


Deterministic Lateral Displacement for Cell Separation

TRUNG SI HOAI TRAN

FACULTY OF ENGINEERING | LUND UNIVERSITY



Deterministic Lateral Displacement for Cell Separation

Trung Si Hoai Tran



LUND
UNIVERSITY

DOCTORAL DISSERTATION

by due permission of the Faculty of Engineering, Lund University, Sweden.
To be defended at Rydbergssalen, Sölvegatan 14. Date June 14th, and time 09:15.

Faculty opponent:

Professor Nikolaj Gadegaard

University of Glasgow

Organization LUND UNIVERSITY Department of Physics Professorsgatan 1 223 63 Lund, Sweden Author(s) Trung Si Hoai Tran	Document name DOCTORAL DISSERTATION	
	Date of disputation 2019-06-14	
	Sponsoring organization	
Title and subtitle Deterministic Lateral Displacement for Cell Separation		
Abstract In the fields of medicine and biology, the separation of particles is a central step in many preparative and analytical processes. <i>Deterministic Lateral Displacement (DLD)</i> has been a promising technique in the field of microfluidic particle and cell sorting, specifically for label-free separation with several applications of sorting by size, morphology, and deformation reported in the literature over the last decade. Separation of cancer cells from a heterogeneous sample is known as a challenging task due to the similarity of the cells involved. Deformability is a potential bio-marker for cell isolation where specific molecular markers are lacking. In the thesis, we demonstrate an efficient measurement tool for cell deformation in the DLD device as well as a sorting tool for cell isolation based on deformability among breast cancer cells (MCF7), human breast cells (MCF10A) and metastasizing breast cancer cells (MDA-MB-231). (Paper 2). Many sorting problems require careful optimization for a successful result. We have approached this problem in two ways: a combination of electrokinetics and DLD for controlling the rotation of RBCs (Paper 3) or through the deformation of the DLD devices by control of the driving pressure (Paper 5). An important limitation of microfluidics is that conventional pumps are difficult to transport, need trained personnel and are associated with high running costs. They are often not fully compatible with point-of-care applications, especially in resource-poor settings. The second part of this thesis therefore focuses on alternative ways to operate microfluidic DLD devices, to ensure portability and user friendliness. A combination of an open DLD device and a paper-based pump is a key component of this approach (Paper 1). Several sorting applications involving blood fractionation, trypanosome enrichment, and breast cancer cell extraction are performed efficiently in terms of potential purity and capture rate. Moreover, our open-fluidics platform is shown to have advantages with regards to easy cleaning, reusability and electrokinetic integration. Finally, an approach for fast and easy fabrication for devices based on single or multilayer stacks is discussed in Paper 4.		
Key words Label-free separation, Deterministic Lateral Displacement, Deformability-based sorting		
Classification system and/or index terms (if any)		
Supplementary bibliographical information	Language English	
ISSN and key title	ISBN 978-91-7895-139-0 (print) 978-91-7895-140-6 (pdf)	
Recipient's notes	Number of pages 125	Price
	Security classification	

I, the undersigned, being the copyright owner of the abstract of the above-mentioned dissertation, hereby grant to all reference sources permission to publish and disseminate the abstract of the above-mentioned dissertation.

Signature



Date 2019-05-09

Deterministic Lateral Displacement for Cell Separation

Trung Si Hoai Tran



LUND
UNIVERSITY

Cover illustration front and back by Trung Si Hoai Tran.

Copyright pp 1-67 (Trung Si Hoai Tran)

Paper 1 © The authors CC BY 4.0

Paper 2 © 2019 by the Authors (Manuscript unpublished)

Paper 3 © 2019 by the Authors (Manuscript unpublished)

Paper 4 © 2019 by the Authors (Manuscript unpublished)

Paper 5 © 2019 by the Authors (Manuscript unpublished)

Faculty of Engineering,
Department of Physics

978-91-7895-139-0 (print)

978-91-7895-140-6 (pdf)

Printed in Sweden by Media-Tryck, Lund University
Lund 2019



Media-Tryck is an environmentally certified and ISO 14001:2015 certified provider of printed material. Read more about our environmental work at www.mediatryck.lu.se

MADE IN SWEDEN 

To my parents and family

Table of Contents

Abstract	8
Popular Summary in English	9
Acknowledgements	10
List of Publications	11
List of Abbreviations	13
Cancer Cell Analysis and Microfluidics: Cell Separation	15
Microfluidic approaches for cancer analysis.....	15
Cell separation in microfluidic devices	17
Deterministic Lateral Displacement: Multiple sorting capability	21
Passive sorting technique	21
High resolution separation	23
Highly tunable and integrated tool.....	26
Sample-oriented sorting applications	29
Size and morphology based sorting	29
Dielectrophoresis – an external field.....	30
Device deformation for tunable separation	32
Deformability as a marker for cell sorting	34
Challenges	40
Simplifying microfluidic separation devices	41
Open channel approach	41
Paper fluidics.....	45
Device fabrication and sample preparation	47
Glue-based mold and multi-layer device	47
PDMS device fabrication	49
Paper fabrication	49
Sample preparation.....	50

Image Acquisition and analysis.....	51
Summary of results and outlook	53
Paper 1. Open DLD channel for particles and cell sorting.....	54
Paper 2. Softness sorting for cancer cells in deterministic lateral displacement.....	55
Paper 3. Electrokinetic rotation of Red blood cells in DLD devices.....	56
Paper 4. Rapid duplication and alignment for multilayers of microfluidic PDMS devices	57
Paper 5. Tunable separation in deterministic lateral displacement by pressure control on varying PDMS stiffness.....	58
Appendix	59
References	61

Abstract

In the fields of medicine and biology, the separation of particles is a central step in many preparative and analytical processes. *Deterministic Lateral Displacement (DLD)* has been a promising technique in the field of microfluidic particle and cell sorting, specifically for label-free separation with several applications of sorting by size, morphology, and deformation reported in the literature over the last decade.

Separation of cancer cells from a heterogeneous sample is known as a challenging task due to the similarity of the cells involved. Deformability is a potential biomarker for cell isolation where specific molecular markers are lacking. In the thesis, we demonstrate an efficient measurement tool for cell deformation in the DLD device as well as a sorting tool for cell isolation based on deformability among breast cancer cells (MCF7), human breast cells (MCF10A) and metastasizing breast cancer cells (MDA-MB-231) (Paper 2).

Many sorting problems require careful optimization for a successful result. We have approached this problem in two ways: a combination of electrokinetics and DLD for controlling the rotation of RBCs (Paper 3) or through the deformation of the DLD devices by control of the driving pressure (Paper 5).

An important limitation of microfluidics is that conventional pumps are difficult to transport, need trained personnel and are associated with high running costs. They are often not fully compatible with point-of-care applications, especially in resource-poor settings. The second part of this thesis therefore focuses on alternative ways to operate microfluidic DLD devices, to ensure portability and user friendliness. A combination of an open DLD device and a paper-based pump is a key component of this approach (Paper 1). Several sorting applications involving blood fractionation, trypanosome enrichment, and breast cancer cell extraction are performed efficiently in terms of potential purity and capture rate. Moreover, our open-fluidics platform is shown to have advantages with regards to easy cleaning, reusability and electrokinetic integration. Finally, an approach for fast and easy fabrication for devices based on single or multilayer stacks is discussed in Paper 4.

Popular Summary in English

Cancer is the second leading cause of death globally (only after heart disease according to the World Health Organization (WHO) 2018). Early diagnosis is the key to higher survival rates, reduced morbidity and treatment costs. Enormous research effort has been dedicated to create diagnosis tools with high efficiency, low cost, reduced time consumption and ease of operation.

Microfluidics, the handling of fluids in micro-scale environments, has great potential to address these challenges. The field has grown rapidly and demonstrated high impact on life science research and diagnosis techniques in the last two decades. In cancer, microfluidics shows promise for better diagnosis, and also serves as an emerging tool to study cancer biology. With the benefits of small sample volumes, multiplexing capabilities, quick operation, and highly sensitive analysis, microfluidics is valuable for cancer detection and investigation. Microfluidic systems have provided an advantageous environment for cancer cell studies such as cellular transduction, cell growth and division, and drug screening. In addition, to detect, isolate and enrich cancer cells, a variety of microfluidic sorting techniques have been successfully exploited.

In terms of biomedical particle separations and fractionations, microfluidic technologies, compared to traditional methods, provide the advantage of reducing operational complexity, small footprint and portability, and the possibility of multiplexing and integration. To contribute to the field of particle separation, the aim of this thesis is to propose a biomedical sorting tool with potential for high efficiency and high throughput that also has potentially low cost and high ease-of-use. By exploring different physical properties of the typical sample (normal and cancerous cells) including size, morphology, electrical/dielectric properties and deformation, this work makes advances towards high efficiency sorting for cancer cell analysis. Another aspect of this work is to simplify microfluidic separation devices. An optimization process is conducted through design automation, simplified fabrication and tunable operation. The study presented here is a modest attempt to contribute to the future of point-of-care diagnostics.

Acknowledgements

First of all, I would like to thank Prof. Jonas Tegenfeldt and Dr. Jason Beech for their support during my Ph.D. for over last four and a half years. Their knowledge and deep insight in physics, and specifically in microfluidics and Deterministic Lateral Displacement have been very valuable, and been a source of inspiration and encouragement. Thanks also to Dr. Stefan Holm for his help with microfabrication and support in the lab. My good group mates, Kush and Oskar, are also my good friends. Thanks for the nice chats and jokes. A big thank to Bao, a colleague, a friend, and a brother.

I am grateful to be a member of the biogroup: Christelle, Heiner, Jonas, Laura, Elke, Fei Fei, Mercy, Martin, Frida, Regina, Kalle, Therese, Roman, Jingyuan, Pradheebha, Ivan, who have given helpful comments about my works during our weekly meetings. I also feel thankful to the faculty, administrative, and technical staff at FTF, who have directly helped me during my PhD or have contributed to building a supportive working environment I enjoy every day: Dan, Jonas Johansson, Anneli, Anders Gustafsson, Maria, Johanna, Janne, Bengt, Håkan, Marica, Mia, Sara, Mariusz, Abdul-Rehman, Charlotte and Helena. And the list goes on. Thank you all for the time I have been at FTF.

I would also like to thank all my colleagues, for a lot of nice discussions and experienced comments that contributed to the scientific dialogue in this Ph.D dissertation, the entire Bio-group at the Division of Solid State Physics, Lund University. The vibrant atmosphere and interesting discussions in this group were a true pleasure to experience. Also, Prof. Bo Baldetorp and his colleagues have been a great help during my projects.

Last but not least, special thanks are due to my parents and family.

Con xin cảm ơn ba Toán, má Lang, bố Hòa và mẹ Thọ và các anh chị trong gia đình mình đã luôn động viên, ủng hộ và giúp đỡ em trong suốt những năm qua. Xin cảm ơn em, Thùy Dung, người đã luôn ở bên cạnh và đồng hành cùng anh trong bất cứ hoàn cảnh nào. Với tất cả yêu thương, papa xin dành tặng cho hai tình yêu nhỏ bé Thùy Nhi và Minh Duy.

List of Publications

The following research papers and manuscripts are included in this thesis:

I. Open channel deterministic lateral displacement for particle and cell sorting (published)

Trung S.H. Tran, Ho, Bao D., Beech, Jason P., Tegenfeldt, Jonas O.

Lab on a Chip, 2017. [DOI: 10.1039/C7LC00707H]

I performed the majority of the experimental work, and analyzed the data. B. Ho contributed to the experiments of electrical measurements. J.P. Beech performed confocal microscopy and macro photography. I wrote the manuscript together with J.P. Beech.

II. Softness sorting of cancer cells in deterministic lateral displacement (manuscript)

Trung S.H. Tran, Jason P. Beech and Jonas O. Tegenfeldt.

I performed all the experiments, analyzed the data and wrote the manuscript.

III. Electrokinetic Rotation of Red Blood Cells in Deterministic Lateral Displacement devices (manuscript)

Bao D. Ho*, Trung S.H. Tran*, Jason P. Beech and Jonas O. Tegenfeldt.

I contributed to conducting experiments, data analysis and wrote the manuscript together with Bao Ho. I did not contribute to investigate the electric/dielectric properties of the sample.

IV. Rapid duplication and alignment for multilayers of microfluidic PDMS devices (manuscript)

Trung S.H. Tran, Bao D. Ho, Oskar E Ström, Jason P. Beech and Jonas O. Tegenfeldt.

I performed the experiments and analyzed the data. B. Ho verified and optimized the procedure. Oskar performed scanning electron microscopy. I wrote the manuscript together with B. Ho.

V. Tunable separation in deterministic lateral displacement by pressure control on varying PDMS stiffness (manuscript)

Trung S.H. Tran, Bao D. Ho, Jason P. Beech and Jonas O. Tegenfeldt.

I performed all the experiments, analyzed the data and wrote the manuscript. Bao Ho simulated the *in-silico* model.

List of Abbreviations

CAD	Computer-Aided Design
BSA	Bovine serum albumin
DI water	Deionized water
DLD	Deterministic Lateral Displacement
G	DLD gap distance
MCF7	Michigan Cancer Foundation-7 (breast cancer cell line)
MCF10A	Michigan Cancer Foundation-10A (human breast cell line)
MDA-MB-231	M.D. Anderson – Metastasis Breast Cancer-231 (Metastasis breast cell line)
LOC	Lab-On-a-Chip
PDMS	Poly-Di-Methyl-Siloxane
PLL-(g)-PEG	Poly (L-Lysine)-graft-Polyethylene glycol
POC	Point-of-care
RBCs	Red Blood Cells
R_c	Critical Radius
WBCs	White Blood Cells
GFP	Green Fluorescent Protein

Cancer Cell Analysis and Microfluidics: Cell Separation

Cancer is a class of pathologies characterized by uncontrolled growth and division of cells. With early detection, a proper treatment can be selected and thus assist in the curing process. Within *in-vitro* cancer cell diagnostics, microfluidics is a promising approach, and an alternative to traditional techniques, to provide efficient and rapid analysis. The current section discusses the role of microfluidics in cancer analysis, with specific focus on cell separation.

Microfluidic approaches for cancer analysis

Among the growing number of potential methods for cancer analysis, microfluidics is being rapidly developed to be a highly promising approach, and has been contributing to the knowledge of cancer. In the last two decades, it has addressed several fundamental scientific questions and biomedical challenges including the areas of diabetes, stroke and cytometry. In terms of cancer analysis, these micro-devices provides new promising tools for cancer detection, cell separation, cell/tissue culture, the study of cell mechanics, and integrated analysis systems (1).

In experimental cell biology, microchips for cell culture have become more and more common. In addition to the traditional cell culture systems (polystyrene dishes, flasks or well-plates), microchips offer an advantageous platform, which mimics the cellular environment, as well as provides flexible control for administration and extraction of reagents and fluids for cell analysis. Figure 1 summarizes several key differences between the macroscopic and microfluidic cell culture. The first advantage of microfluidic cell culture is the high flexibility of the designs to target specific cells in typical experiments. Small volumes, low reagent consumption and the ability to work with a small number of cells are among the unique strengths of microfluidic systems compared to macroscopic cultures. Furthermore, microfluidics

facilitates the realization of any necessary 3D environment, co-culturing as well as real-time on-chip analysis, which cannot be conducted in conventional culturing (2).

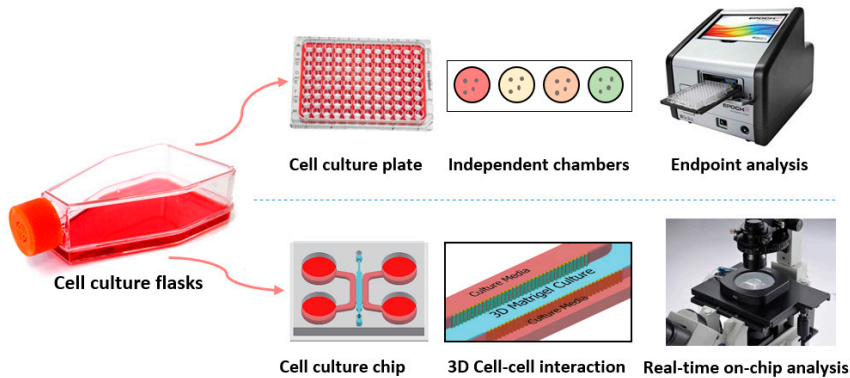


Figure 1. Traditional cell culture system and microfluidic cell culture devices.

Microfluidics makes for a great system for studying cancer cell growth, division, cell mechanics, and cell cycle, in both two- and three-dimensional environments. 3D culture chips have successfully been used to study the complex cellular environment, cell migration and invasion of cancer cells (1). Recently, there have been advances in developing tumor-on-a-chip systems (3) as a new cell culture technology, which integrates microfluidics, tissue engineering and biomaterials to create human tumor models for oncology, immunotherapy studies and drug screening. The model allows well-controlled on-chip-analysis of the interaction among tumor cells, immune cells and tissue.

In addition to cell culture, the capability of studying cell mechanics is another interesting aspect of microfluidics. For example, cancer cells with stiffnesses that differ compared to healthy cells, can be directly characterized in a microfluidic cell squeezer (4) or compressive PDMS chamber (5). By carefully controlling the flow velocities, and visualizing cell morphology using high-speed imaging, it has become possible to measure cellular deformability through real-time deformation cytometry (RT-DC) (6).

Finally, one of the most promising areas of cancer research is the development of a total-analysis-system for separation, culture and analysis of cells on a single device, to enable point-of-care systems. Although there remain several challenges in each method, several successful modular elements have been reported and are

being developed, to combine various functions into a single device as shown in Figure 2.

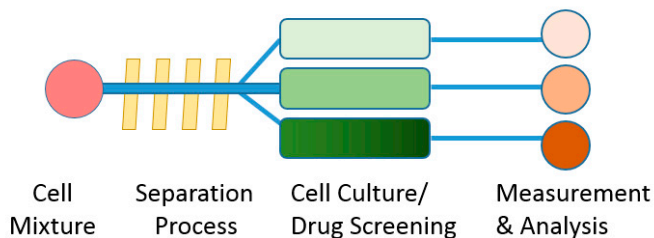


Figure 2. Schematic of a microfluidic platform which integrates cell separation, cell culture and on-chip analysis.

Cell separation in microfluidic devices

Cell separation is an essential preparative step for a vast majority of cell studies. In cancer diagnosis, several conventional cell sorting techniques including centrifugation, chromatography, fluorescent and magnetic-activated cell sorting are currently used. However, these methods have been limited in terms of yield and purity, require expertise in handling, bulky equipment or specific and expensive antibodies. These limitations have fueled the development of microfluidic sorting techniques, which have contributed greatly to the field (1).

The performance of cell separation is strongly dependent on the properties of the sample of interest. The need for isolation and sorting of cells based on different biochemical and biophysical parameters is a central component. For instance, cells can be described by intracellular properties (DNA, RNA, and protein molecule interactions) or extracellular physical properties (size, morphology and surface protein expression). Traditionally, research in the field has used flow-cytometry (7), magnetic separation (8), and density-gradient centrifugation. Novel chip-based technologies have the potential to accelerate discovery and enable sample manipulation to greatly advance the field.

Fractionation of heterogeneous biological samples is a major application of microfluidic sorting techniques. Indeed, microfluidic techniques have the ability to separate particles with high precision and resolution in terms of a variety of physical properties and principles (9). These sorting technologies are identified as either

active methods, that apply external forces to sort particles, or passive methods, that exploit channel geometries and hydrodynamic forces including inertial forces (10), obstacle arrays (11), and other mechanisms to achieve the separation.

Another way to categorize these techniques is the need for additional labels: fluorescent label-based sorting, bead-based sorting and label-free sorting. While fluorescent label-based sorting relies on molecular interactions to selectively identify types of cells, label-free separation is based on the inherent physical characteristics of cells. Such physical markers could be size, shape, deformability, density, electrical polarizability, electrical impedance, magnetic susceptibility and hydrodynamic properties.

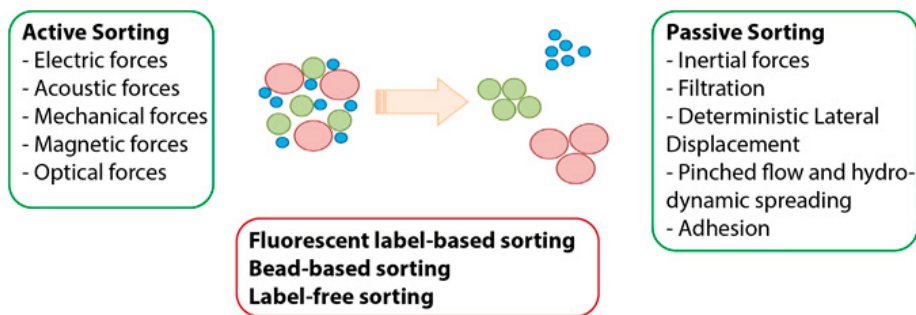


Figure 3. Microfluidic sorting techniques can be divided into by active and passive sorting methods, fluorescent label-based sorting, bead-based sorting or label-free sorting.

A short introduction to some of the most popular microfluidic sorting techniques (active and passive methods in the label-free sorting group) is given below. More details could be found elsewhere (12, 13).

- *Pinched Flow Fractionation (14)* separates particles by focusing all particles close to a wall. Based on their size, each particle then follows a separate streamline.
- *Inertial microfluidics (10)* works under specific conditions which maintain both laminar flow and inertial forces to place the particles in different positions within a flow based on their size.
- *Deterministic Lateral Displacement (11)* affects the path of particles through an obstacle or pillar array, based on the particle's effective size and the particular geometry of the array.

- *Field Flow Fractionation* (15) uses an additional force field perpendicular to the fluid flow to separate particles.
- *Acoustophoresis* (16) employs an acoustic field perpendicular to the fluid flow to achieve the separation. Size, density, compressibility are key particle parameters affecting the separation.
- *Electrophoresis* applies an electric field to temporally or spatially separate particles based on their electrophoretic mobility (for instance, gel electrophoresis and capillary electrophoresis (17)).
- *Dielectrophoresis* (18) generates a non-uniform electric field to utilize the difference in size and effective polarizability of particles, and hence enables separation.

From the microfluidic sorting techniques summarized above, Deterministic Lateral Displacement was the technique chosen for the label-free particle sorting presented in this thesis. The technique has been exploited here to separate based on particle deformation and integrated with electrokinetics, in addition to size and morphology based sorting. Furthermore, we present the capability of simplifying microfluidic devices by removing the lid and running them in opening channels. To increase the versatility of the devices, we have explored various ways of tuning the performance.

Deterministic Lateral Displacement: Multiple sorting capability

Adequate resolution, throughput and purity are basic requirements for cell sorting methods. They are also usually used as quality parameters to compare different sorting tools. However, another performance indicator is the number of sorting parameters that can be applied. Deterministic lateral displacement (DLD) is one of a few techniques which is capable of sorting using multiple sample parameters. Key capabilities of DLD are presented in detail in this section.

Passive sorting technique

Deterministic lateral displacement (DLD) is a passive particle separation technique. It was first introduced in 2004 by Huang *et al.* for separation of microspheres by size and DNA by length (11). Using an array of posts or obstacles, the main idea of separation is that the small particles move straight through the device (known as *zig-zag mode*), while bigger particles move with a specific angle (known as *displacement mode*). Figure 4 shows the sketch of a typical device, and demonstrates sorting of polystyrene particles of different sizes in a DLD array.

Due to the micro scale (with the dimensions of channels typically ranging from 100nm to 100 μ m), the Reynolds number is small and usually less than 500. Therefore, the fluid flow is completely laminar and no turbulence occurs. The sample, consisting of a heterogeneous population, is loaded into an inlet at one end of a pillar array. The particles follow different paths through the pillar array, depending on their sizes: small particles move following the flow in a zig-zag path, while the large particles are displaced relative to the flow direction. The trajectory of each particle is a function of its effective size. The effective size, in turn, is determined by a combination of, for example, size, shape, orientation and deformation of the particles at a certain position.

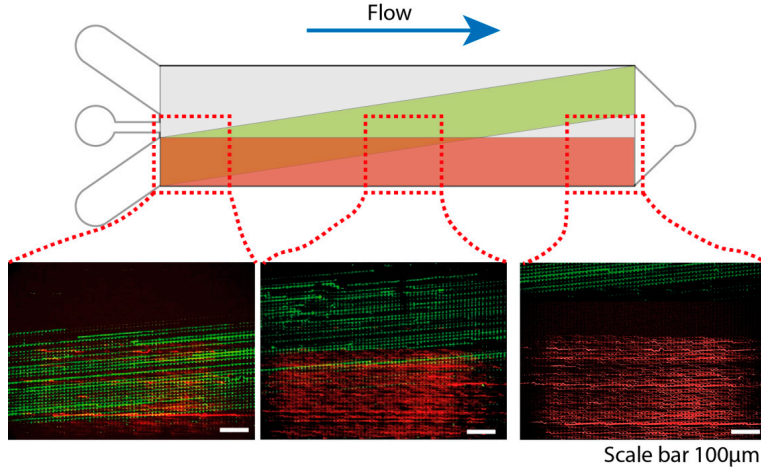


Figure 4. Schematic of a typical sorting device along with experimental results. Fluorescence microscopy images show green (diameter: $16\mu\text{m}$) and red (diameter: $5\mu\text{m}$) particles separated in a DLD array.

The separation performance of each DLD device is based on the critical size (D_c). Davis *et al.* proposed an empirical formula describing the critical size based on experiments with the circular posts in arrays and rigid spherical particles (19).

$$D_c = 1.4GN^{-0.48}$$

Here, D_c is the critical diameter, G is the gap between two posts, and N is the period of the array. This equation can be expressed in some practical parameters as shown in figure 5.

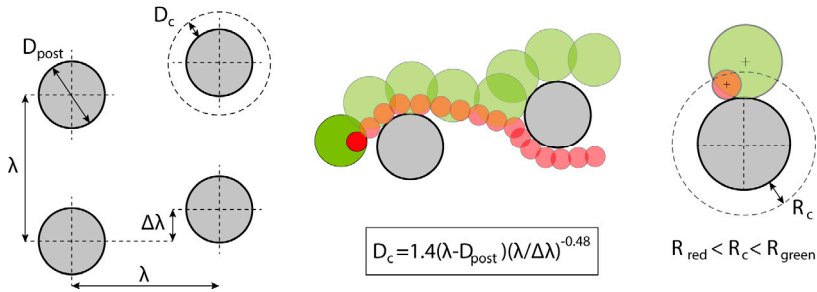


Figure 5. Typical definition of DLD parameters and particle behaviors in relation to the critical size. With λ is a space between the post centers, the second row of posts shifted by a distance $= \lambda/N$, where the array repeats itself after N rows.

The critical size is the most important parameter for the sorting characteristics of a DLD device. Particles smaller than a critical size are defined as small particles, while the others are considered large particles. Besides, gap size and the depth of a device, other device parameters need to be considered carefully for particle selection to avoid trapping and device clogging. Particles larger than the device depth or gap size may be trapped in the reservoirs or in the entrance of the array.

As a passive sorting technique, DLD changes the trajectories of targeted particles, but it does this through the interactions between the particles and the pillar array, instead of due to externally applied fields. This advantage of passive methods makes them less dependent on any additional equipment or skilled personnel and gives a high potential for a portable and easy-to-use tool, for instance, a portable trypanosome sorting tool (20) and open DLD device (21) as shown in Figure 6.

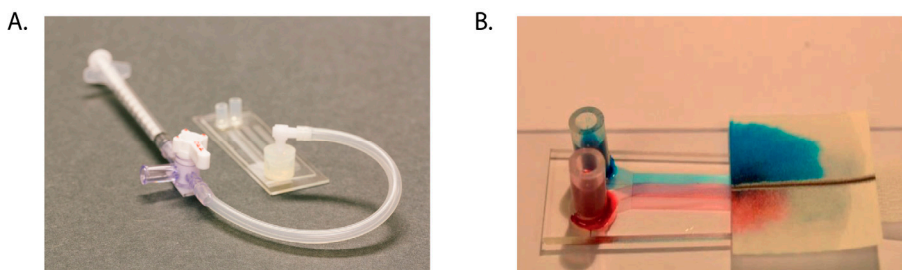


Figure 6. Portable DLD devices. A) Trypanosome sorting tool with a handheld syringe. B) Our Open DLD device with capillary flow. Images taken from (20, 21) . Published by The Royal Society of Chemistry.

High resolution separation

Since the first application in DNA separation and for separation of small polystyrene microspheres (11), DLD has been demonstrated as a high resolution separation technique, with a resolution down to 10 nm. In the last decade, DLD has evolved dramatically and has been adapted to a variety of biological samples with different sample properties. Significant effort has been made to deeply understand the theory as well as design considerations for new target samples. For example, to prevent clogging and to increase the volumetric throughput, much effort has been spent on pillar shape optimization, via both experimental and theoretical approaches. A variety of pillar designs has been reported, including triangles (22-29), squares (26,

30), I- or L-shapes (30-33), diamonds (26), eggs (34), and specific topologically optimized shapes (35) besides circular pillars (Fig.7C). Another consideration is the array design accounting for the wall effect (36), anisotropic permeability effect (37-40) (Fig.7A,B), throughput (24) and combining multiple sections (with different critical sizes) (22).

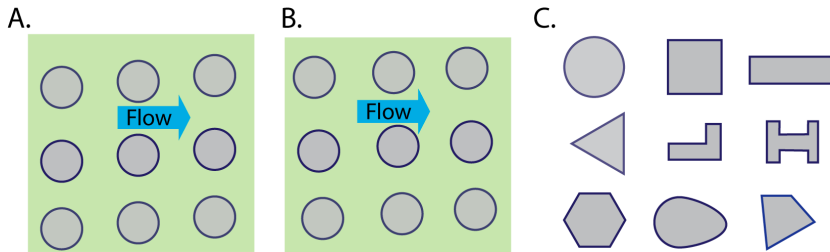


Figure 7. Design consideration for DLD geometry. A) Rhombic array B) Rotated squared array with circular pillar. C) A variety of pillar shapes have been optimized for various applications in DLD devices.

In bio-applications, DLD has been employed to sort a wide range of particles, for instance, fractionation of blood components (12-15), isolation of cancer cells from blood cells (16-18), and parasite separation (20, 41). Other sample types with their sizes are listed in table 1. Among those, the fractionation of blood components is highly interesting. Compared to density gradient centrifugation and direct magnetic approaches, DLD-sorted cells have a more complete and consistent degree of phenotype expression (42). In the near future, automated DLD chips could be a commercial product with precise separation and high throughput (42, 43).

Table 1. Examples of DLD applications in term of particle size and resolution.

	Particle size	Resolution
Below 1µm		
DNA length (11, 44)	Bacterial artificial chromosomes 61kb - 158kb (11)	~ 90kb
	Double-stranded DNA 100-10.000bp (44)	~ 200bp
Exosomes Concentration (45)	Exosomes 20-140nm	~ 90nm
Micro-vesicle from blood (46, 47)	Micro-vesicle 100nm-1µm RBCs & WBCs (6-8µm)	>1µm
Bacteria length (48)	Streptococcus pneumoniae Single Cocci 1-1.5µm Diplococci 3µm, Chain >6µm	>1µm
In a range of 1-10µm		
WBCs from blood (43, 49-60)	Erythrocyte 5-8µm Leukocyte 7-20µm	>1µm
Blood plasma from blood (19, 61-63)	WBCs 5-20µm, RBCs 2-8µm Platelets 1-3µm	>1µm
Nucleated RBC (NRBCs) from blood (64)	Maternal RBCs & Platelets 2µm NRBCs & WBCs 5-10µm	>1µm
Trypanosome from blood (20, 41)	RBCs 2.5-7.5µm Trypanosome cyclops 2.5-30µm	>1µm
Epithelial cells from fibroblasts cells (65)	Epithelial cells 15-20 µm Fibroblast cells 10.7-16.7µm	>1µm
Cardio-myocytes from heart tissue (66)	Cardio-myocytes 7-20µm Non-myocytes 4-71µm	>1µm
Cancer cell lines (28)	SK-BR-3 12.07 µm MDA-MB-231 15.81µm	>1µm

	SUM-159 13.14 μm SUM-149 14.13 μm MCF10A 14.15 μm	
Viable and nonviable Jurkat cells (67)	Viable Jurkat cells 12.3 μm Nonviable Jurkat cells 6.9 μm	>1 μm
In a range of large particles (>10μm)		
Droplet size (68, 69)	Main droplet 61.1 μm Satellite droplets 1-30 μm Size groups 21.4 μm , 10.1 μm and 4.9 μm	>5 μm
Fungal spores from debris (70)	Aspergillus fungal 4 μm Spore debris 10-100 μm	>5 μm
Circulating tumor cell cluster (33, 71-74)	CTC cluster 4-30 μm	>10 μm

Highly tunable and integrated tool

Although DLD is a size-based sorting technique, its capabilities have been extended to a tunable and integrated device. DLD is also a promising method for sorting based on morphology, density, deformability and surface charge based separation.

In 2011, Holm *et al.* reported DLD as a morphology-based sorting tool in parasite extraction (19). A few years later, Beech *et al.* successfully employed this capability to separate bacteria based on chain length (48). Further, DLD has been employed as a deformability-based sorting tool for red blood cells (23) and platelets (24). Finally, DLD has been used to sort based on density (75).

As a passive method, a fixed geometry design with a specific critical size has limited its flexibility. An attempt of tuning the critical size during the sorting process was proposed by stretching an elastic DLD device (76). However, a complex setting rendered its use impractical. Instead, an integration of electrokinetic forces (77) has proven a clear impact on particle separation, especially for same-sized particles. The implementation complicated the operation of DLD, but it also extended the dynamic range of the device. Another attempt of integration is the open DLD and paper

fluidics (21) that we developed. Ease-of-use in resource limited settings and an open platform for integration are the primary advantages of this method.

Whilst most microfluidic sorting techniques employ a pressure difference to drive the flow and particles, DLD has also been demonstrated with alternative driving mechanisms. For example, capillary force (21, 78), centrifugal force (79), gravity (80) or electroosmotic-driven flow (11, 81) can substitute for syringe pumps or pressure pumps.

In summary, thanks to a vast range of attempts and efforts during the last decade, DLD has been significantly improved with multiple sorting capabilities. With a wide range of applications, it has highly contributed to the particle separation field. This thesis will mainly focus on deformability-based sorting, simplifying DLD fabrication, tunable separation and an open DLD platform.

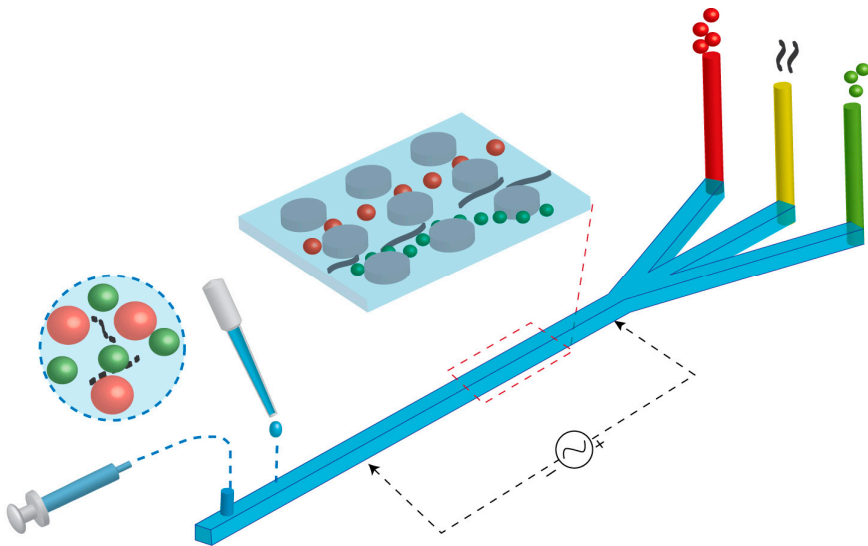


Figure 8. Overview of sorting based on size, morphology and deformability. The force driving the flow can be capillary force or applied pressure. Electrokinetic integration is also possible for tuning separation.

Sample-oriented sorting applications

Size and morphology based sorting

Essentially, DLD is a size-based sorting technique. The difference in size of the particles is the first main consideration for cell sorting. By using an open platform of DLD, we demonstrated size-based sorting for blood fractionation (RBCs 4-8 μm and WBCs 10-15 μm) and cancer cell isolation from blood (MCF7 cells 15-20 μm) (Fig 9A). As the size difference between targeted cells is large (>2 μm), the sorting results are clearly observed even without labelling. However, the size parameter may not be sufficient in practice if the particles are non-spherical, such as RBCs (disk-shape) and parasites (long, slender, tapering and arched). Based on the orientation of the particle, the effective size may change significantly. Therefore, an approach of controlling the cell orientation or morphology-based sorting is employed.

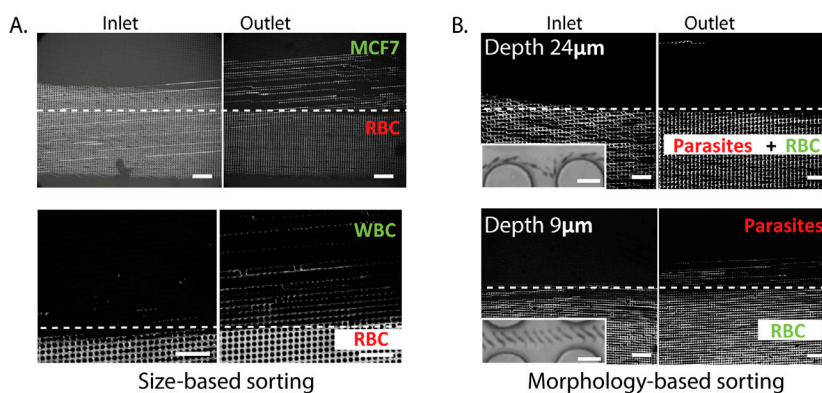


Figure 9. Size and morphology based sorting for A) cancer cell isolation, blood fractionation and B) parasite extraction. Scale bars 100 μm and 10 μm for the insets. Image from (21), Published by The Royal Society of Chemistry.

In order to sort out parasites from blood, Holm *et al* (20) optimized the channel height to maximize the displacement of parasites, while RBCs zig-zag. Figure 9B

presents the effect of channel height in relation to parasite flow-behavior. As illustrated in the figure, no parasites are isolated in a device of depth $24\ \mu\text{m}$, while in a $9\ \mu\text{m}$ deep device, all parasites displace to an upper stream. However, the shallow channel reduces the volumetric flow rate, and thus the throughput or parasite capture rate. In an attempt to orient RBCs without modifying the channel geometry, electrokinetic forces may be superimposed to induce rotation of RBCs in the flow.

Dielectrophoresis – an external field

In 2009, Beech *et al.* (77), introduced dielectrophoretic forces in the pillar array. The use of dielectrophoresis (DEP) has paved way for particle separation based on polarizability, in addition to hydrodynamic size, in the DLD devices. By changing the frequency and magnitude of the applied electric field, the effective size of the particles is tunable, and hence separation is possible. As an alternative to fabricating DLD devices with the specific depth to obtain the parasite extraction, we explore how the effect of the DEP force or other electrokinetic effects may help separation in this study.

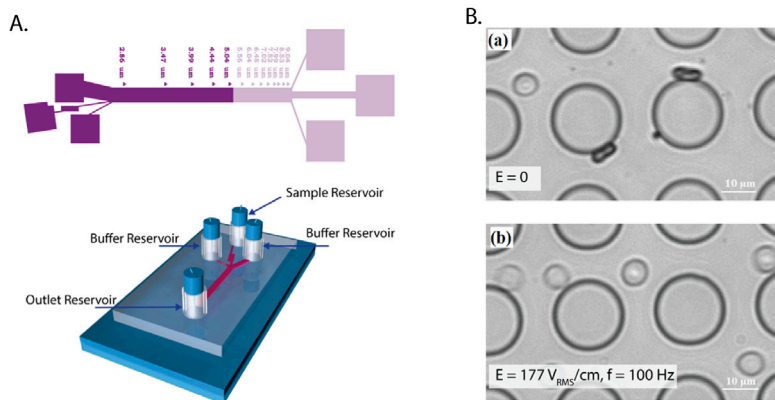


Figure 10. Experimental setting and results A) Electrodes attached at inlet and outlet reservoirs in a DLD device B) The orientation of RBCs as a function of an applied electric field (at 100Hz). Scale bar 10 μm .

Although the rotation of RBCs was observed clearly and the displacement was achieved, high voltages were required and, there was an issue of cell viability due

to Joule heating. Since PBS buffer has a high electrical conductivity (1660mS/m), the temperature may increase significantly when high voltages are applied. An attempt of reducing medium conductivity by sucrose showed a better result of cell morphology (compared to the spherical shape of few cells in the high medium conductivity) while cell displacement was decreased. Further optimization of the running medium to maximize RBCs rotation is required for successful use of the approach for parasite extraction from blood.

In the closed DLD devices as mentioned above, electrodes may only be placed externally in the inlet and outlet reservoirs, which leads to relatively low field strengths in the array. In order to maximize the external force, introduce flexibility of the localization of the stimulated area as well as reduce the Joule heating effect, the open DLD platform has been investigated.

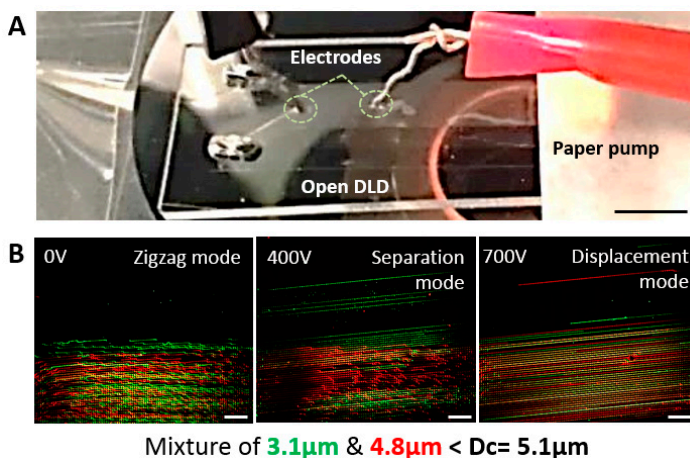


Figure 11. Combination of open DLD and Electrokinetic DLD. A) A typical set up where electrodes are placed in the selected area. B) By tuning the applied voltage (0V, 400V and 700V), the trajectories of particles are changed. Scale bar 100 μm . Images taken from (21). Published by The Royal Society of Chemistry.

In the experiment (Fig.11), a mixture of 3.1 μm and 4.8 μm microspheres were separated in a DLD device ($D_c=5.1\mu\text{m}$). The separation was obtained at 400V. The result was similar to the closed device but the applied voltage was smaller and occurred in a smaller zone. Other advantages of open microfluidics will be discussed in the open DLD section. As a short conclusion, the external force, in this case dielectrophoresis, has expanded the sorting capability of DLD and thus demonstrates a useful integration of two mechanisms in the device.

Device deformation for tunable separation

Many sorting problems require optimization for a successful result. We have approached this problems in two ways: a combination of electrokinetics with DLD for tuning RBCs rotation or tuning particle separation in the open platform or through the deformation of the DLD devices by control of the driving pressure. The second approach of device deformation is expressed in this part.

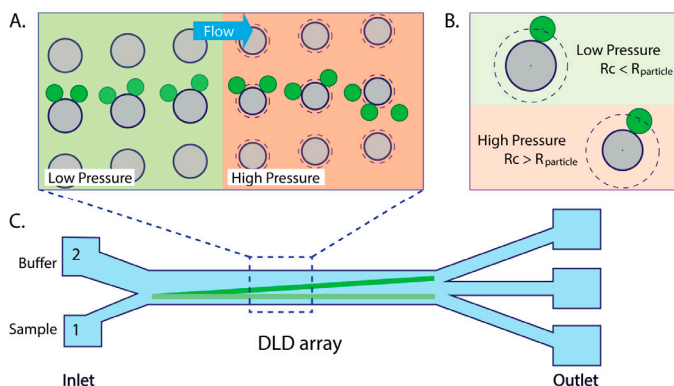


Figure 12. Effect of soft pillar change on particle distribution. A) DLD array and particle trajectories in low and high pressure. B) Critical radius and particle size in both cases. C) A schematic of a DLD device.

Figure 12 shows the effect of post deformation on the particle trajectory. High applied pressure causes the post compression and decreases its size as well as increases the critical size of the array (following the Davis's equation (19)). As a result, the particles which are expected to displace (due to the effective size being larger than the critical size) now move in the zig-zag mode (effective size smaller than the critical size).

In our experiments, 15 μ m Polystyrene beads were used to calibrate the device as shown in figure 13. When the driving pressure is increased, the particles shift to the left and assume to a smaller value of the effective size. Due to the high stiffness of the beads (Young's modulus of 3-3.6x10⁹Pa), the deformation of PDMS is considered and taken in account for a correction. In paper 5, a correction of the critical size is performed by the measurement of post deformation.

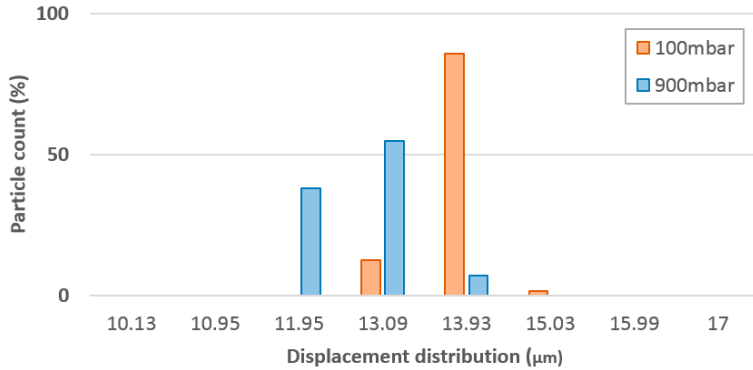


Figure 13. A comparison of 15μm Polystyrene beads at low (100mbar) to high pressure (900mbar). The displacement distribution was effected by pressure control.

The deformation of the posts is related to the stiffness of PDMS which in turn depends on the mixture ratio (the base and the curing agent) and curing time and temperature. The deformability of the device also depends on how much material is deformed and so the Device thickness is also important. A survey of these parameters is shown in figure 14 (curing time has not been tested yet). In this survey, we test different combinations of parameters for PDMS device fabrication in order to avoid or exploit the deformation.

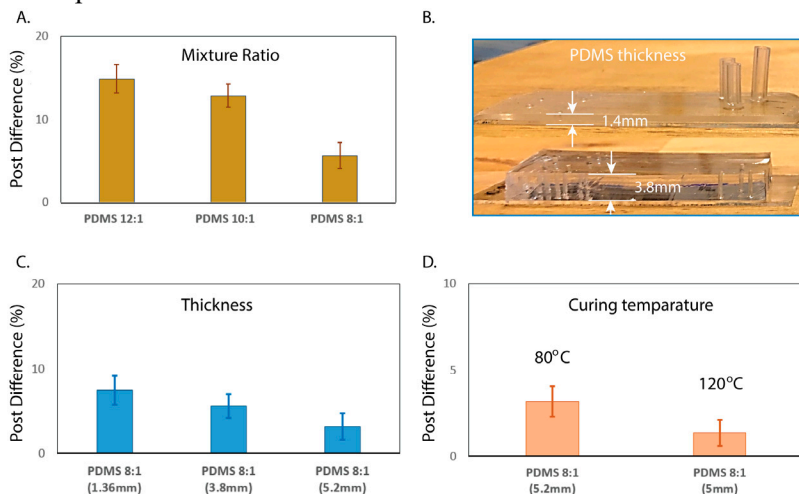


Figure 14. Different parameters related to PDMS stiffness. A) Mixture ratio (12:1; 10:1 and 8:1). B) & C) Device thickness (1.36mm, 3.8mm and 5.2mm) and D) Curing temperature (80°C and 120°C). Post difference refers to the relative change of the post diameters upon application of a 900mbar pressure across the device.

Deformability as a marker for cell sorting

Deformability

Size and morphology are basic label-free markers which are commonly used to discriminate cell types and effectuate separation in DLD. However, in this section, we discuss the mechanical property of deformability as an additional separation parameter. We aim to exploit deformability as a biomarker, to identify cell types as well as to separate them. The aim is cancer cell detection and isolation for cancer cell analysis and diagnostics.

In general, cancer cells are derived from normal healthy cells and undergo uncontrolled growth and division. Although cancer cells have a wider size distribution than their healthy counterparts, and may also have higher prevalence of irregular shapes, the significant overlap in these characteristics renders them unusable as distinguishing or separation parameters.

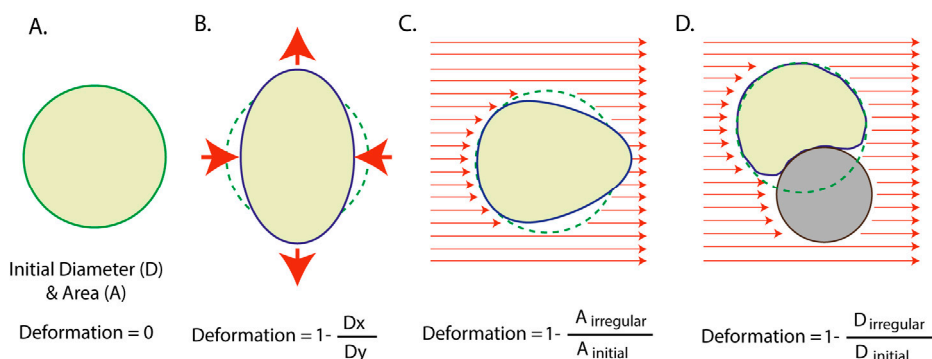


Figure 15. Different approaches for deforming a spherical particle along with different definitions of deformation.

We examined a breast cancer cell line (MCF7) and normal cells (MCF10A) in suspension using optical microscopy. Without labelling, the two cell lines are indistinguishable. Size and shape measurements give a better understanding of the similarities. While the breast cancer cells have a wide size distribution, which overlaps with the distribution of normal cells ($15.5 \pm 4 \mu\text{m}$ and $15.1 \pm 2 \mu\text{m}$, respectively), the circularity shows a uniform spherical shape of both cells. A significant difference between the two cell types is their propensity to form

aggregates; 12 % of the cells form aggregates for MCF7 and 3% for MCF10A. It is believed that cancer cells prefer to form aggregations or clusters (82).

In cancer cell research, higher deformability has been shown to be an inherent characteristic of metastatic cells (83). Without the need for chemical modification or molecular labelling, deformability is a label-free biomarker, has potential as an important parameter for cell characterization and cell phenotype discrimination. To measure the deformability of cells, a variety of techniques have been reported, such as micropipette aspiration (84), atomic force microscopy (AFM) (85-88), optical tweezers (89), and real time deformability cytometry (RT-DC) (6). By stretching or compressing a single cell in the optical tweezer (83) and AFM (85), a spherical cell is deformed into an ellipsoidal shape as in figure 15B. Each single cell will be independently measured and evaluated with respect to its degree of deformation. RT-DC, was introduced in 2015 by Guck *et al.* RT-DC has a much higher throughput (100 cells/s) (6). In a micro-channel, images of single cells are captured using a high-speed camera. Shear forces cause cells to deform into a bullet shape (Fig.15C). The shape of the deformed cell is used to calculate its deformability. An alternative method is a ratchet method (90), which traps cells in microfluidic constrictions, an effect that depends on deformability.

DLD and cell deformation

We aim to employ deformability as a label free marker for cell sorting in the DLD array, where the effective sizes of particles determine their trajectories and outlet distributions. Figure 16A shows how the effective size of a particle can change with deformation and how this can have a large effect when the effective size becomes equal to the critical size. Particles larger than the critical size, R_C , will displace while the others follow the flow. In the case of soft particles, although particle size is larger than the critical size, the effective size could be smaller (due to the deformation) and they behave like small particles (Fig.16B).

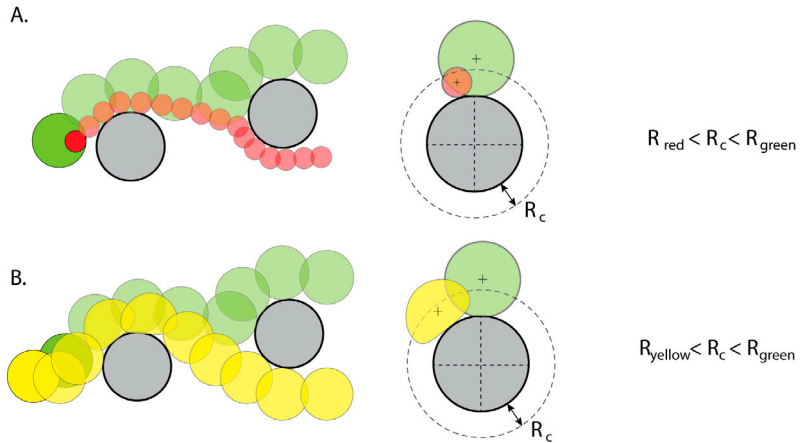


Figure 16. Particle trajectories in relation to size, and deformability. A) Both hard particles with size difference. B) Same-sized particles with difference of deformability.

Different cell types have been shown to undergo different ranges of deformation (83, 86). As an example of cell deformation, an individual MCF7 cell was captured at high driving pressure (900mbar) in figure 17A. At low shear rates, the small (red) cells are in zig-zag mode and the large (green) cells are displaced following the DLD sorting mechanism. At high shear rates, the large cells deform (yellow) move in the zig-zag mode, together with smaller cells.

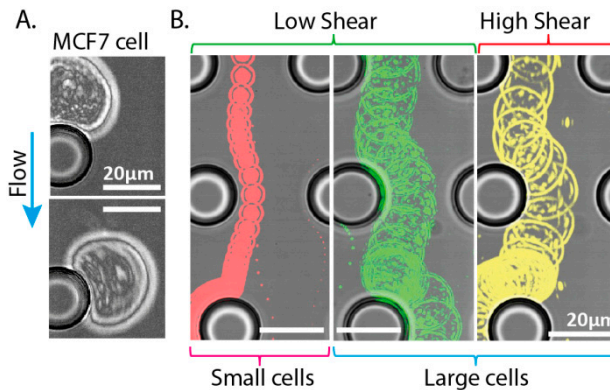


Figure 17. Cell deformation in a DLD array. A) MCF7 cell deformed at high pressure (900mbar). B) Based on size and deformability, different trajectories of cells are observed.

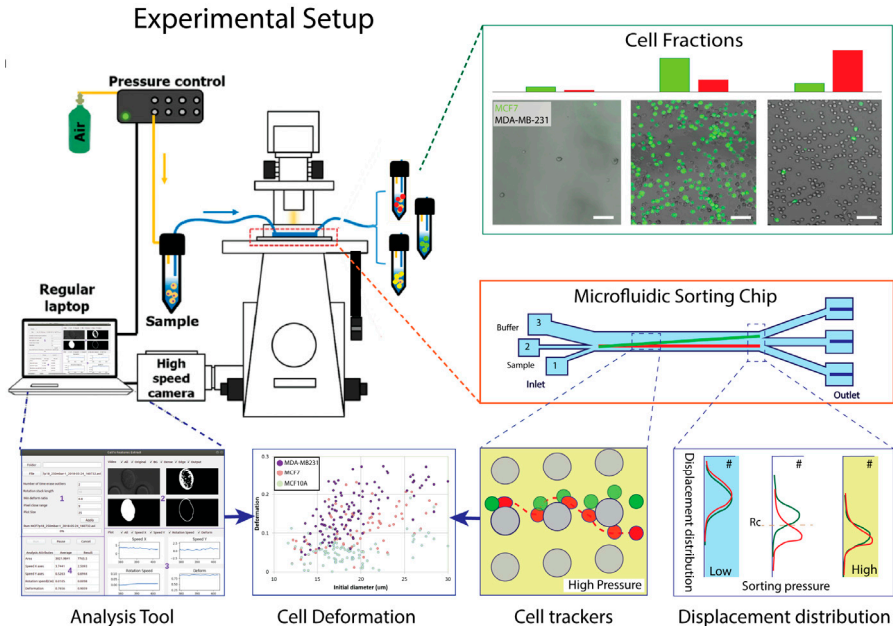


Figure 18. Overview of deformability-based sorting experiment. A sample of cells was loaded into a microfluidic sorting chip (DLD) by air pressure (controlled by the users). During the sorting operation, the sample could be captured in different selected areas for the measurement of cell deformation, cell tracking or cell counting. An analysis tool was used to detect and extract all needed information to obtain the results (the single cell measurement, the displacement distribution or the sorting purity). After sorting, different fractions of cells were collected and used for downstream analysis. Scale bar 100 μ m.

Figure 18 gives an overview of our work on the deformability-based sorting for cancer cell characterization and isolation. The cell identity and deformation have been characterized at three distinct levels.

- Firstly, single cells are directly visualized when in contact with the post array. The deformation is extracted using an image analysis tool developed for the purpose.
- Secondly, cell distributions at the end of the array are counted and measured. The deformation is inferred from the position of the cell at the end of the device. A different image analysis method is utilized for this approach.
- Finally, different sorted fractions are analyzed at the outlet reservoirs to confirm the sorting capability.

In summary, we have successfully demonstrated and measured the deformation of non-malignant cells (MCF10A), breast cancer cells (MCF7) and invasive cells (MDA-MB-231) using DLD devices (Paper 2). We find that the invasive cells (MDA-MB-231) are highly deformed at the high flow rates (900mbar) while MCF10A cells are slightly deformed compared to MCF7 cells. While the direct visualization of the cell deformation process gives better values on deformability (since both the size and deformation are simultaneously measured for individual cells at high magnification and resolution) (Fig.19A & B), the second approach allows the measurement to be performed on many more cells but gives less accurate results (measurements are done at much lower magnification and resolution) (Fig.19C & D). The first approach is limited by the amount of data that can be collected for each cell which in turn is limited by data transfer rates and the internal memory of the camera. As a result, the data only represents a small number of cells (less than a hundred cells for each cell line).

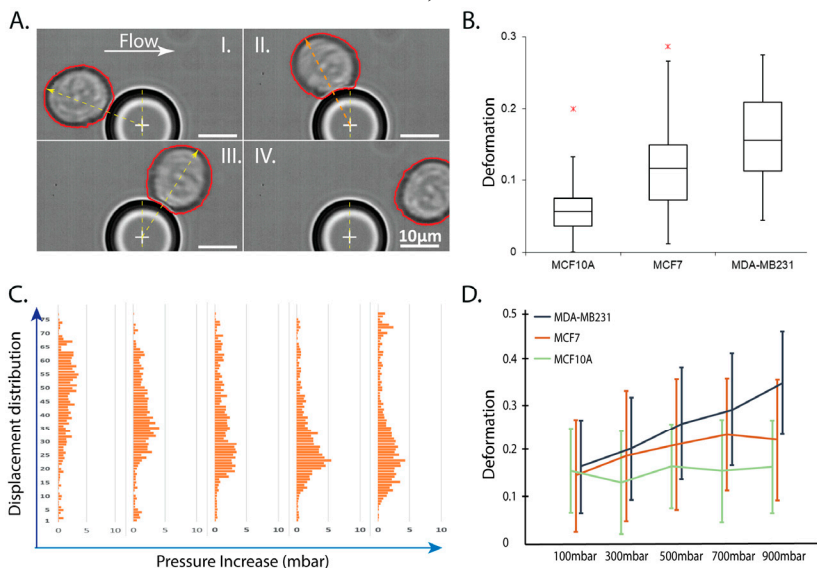


Figure 19. Cell deformation among three cell lines (MCF7, MCF10A and MDA-MB-231). A) & B) Direct measurement from image features (at 900mbar). C) & D) Indirect measurement from cell size and displacement position.

In this section, we propose the use of a DLD device as a deformation measurement tool, besides its separation capabilities. By optimizing the data processing and hardware setting, it is possible to develop a real-time analysis and sorting system, for cancer cell analysis and diagnosis.

To test cell separation, a sample of cells is loaded to the DLD array. Based on the correlation between displacement distribution and applied pressure for each cell line, matching data helps us to identify the sufficient pressure which maximizes the sorting efficiency. For an example of matching data, a comparison of stained MCF7 and MCF10A is shown in figure 20.

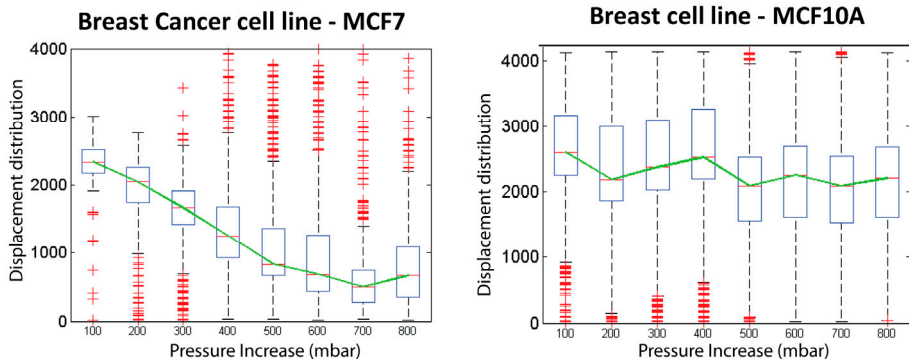


Figure 20. A comparison of displacement distribution of stained MCF7 and MCF10A cells. The mean value of the box-plot presented two different tendencies of cell distribution in relation to pressure increase (from 100-800mbar). The outliers showed the distribution of very large or very small cells. As a results, the separation between two kinds of cells could be obtained from 400mbar.

Another mixture of MCF7 and MDA-MB-231 cells was passed through the DLD array. Because the high speed camera used in these experiments was not sensitive enough to visualize fluorescence from cells moving at high flow rates through devices, it was not possible to visualize displacement distributions. Instead, we collected cells in containers at the outlets of the device and then counted the cells post separation (Fig 21).

The ratios of the different cells types in the collection tubes shows a significant difference compared to the initial mixture (50:50). In tube 2, the ratio reached 71:29, (MDA-MB-231:MCF7) and close to 75% of MDA-MB231 cells were collected. In tube 3, the ratio of was 32:68, and close to 35% of MCF7 cell were recovered.

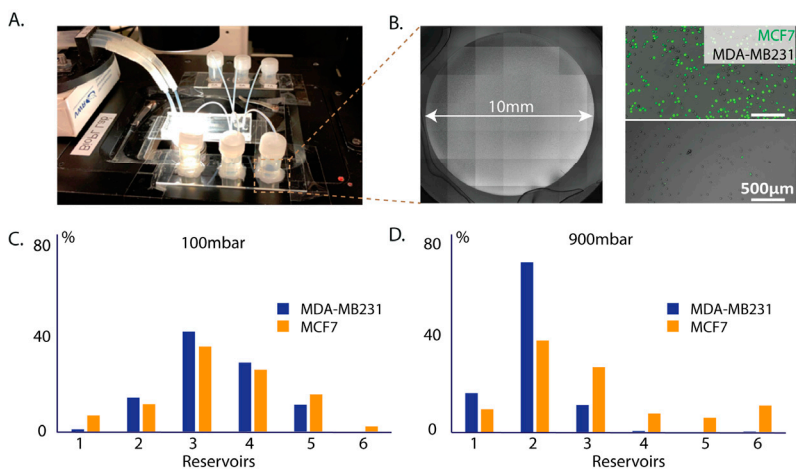


Figure 21. Deformability-based sorting for MCF7 and MDA-MB-231 cells. A) A typical setup for cell sorting. B) Tube reservoir in a large scale and fluorescent images to distinguish MCF7 (GFP) and MDA-Mb-231 cells. C) Percentage of cells in each tube at 100mbar. D) The separation occurs when MDA-MB-231 cells deforms more than MCF7 does.

Although the performed separation does not demonstrate high purity, the results clearly demonstrated the effect of cell deformation on the sorting process. Future work in this direction would aim at a new design of DLD with smaller critical size, and higher operational pressures.

Challenges

While the above sections have described the potential of DLD and other microfluidic sorting techniques, in practice, there exist several challenges to be considered as clogging, high throughput application, easy-to-do operation or mass production of devices.

Clogging is a common issue when loading particles in a micro-channel (91) and pillar array can be especially susceptible to this. In a common DLD device, there is a large surface area where particles will interact with posts and walls. The interaction commonly causes clogging during device operation. We studied the ability of different surface treatments (PLL-PEG, Pluronic, and BSA) (92) to prevent clogging. In some cases, we can use adhesion in the sorting process, see the section of open DLD below with the application of blood purification.

Simplifying microfluidic separation devices

Open channel approach

To simplify the microfluidics, we have explored a DLD device without a lid on the microfluidic channels. We have demonstrated the advantages of accessibility (addition of reagents, retrieval of biologic liquids or objects, human intervention on the system), the minimization of air-bubbles and clogging and how the open architecture facilitates cleaning. We expect that open microfluidics (93) to be a potentially highly interesting choice for point-of-care and home-care-systems.

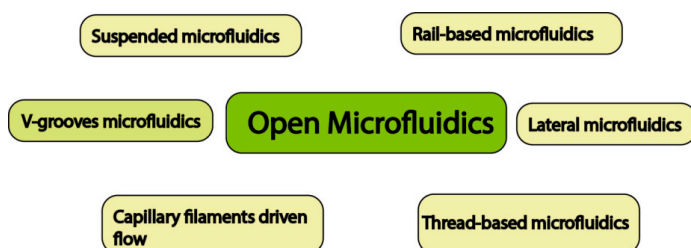


Figure 22. Overview different open microfluidics that has been reported in the literature.

The first open DLD, introduced at MicroTas 2009 (78, 94), showed a successful result of separating the small particle from the mixture by capillary flow. The improvement of separation (for both small and large particles), sample volume and continuous flow was done by our work a few years later when an integration with paper fluidics was utilized successfully. A complete device with varying bio-particle sorting applications was presented recently in Paper 1 (21). The open DLD chip is a portable tool with good prospects to use outside the lab and in resource deprived areas.

To realize the open DLD we simply remove the lid of a typical DLD chip, treat the surface, add reservoirs in the inlets and paper channels at the end of the array (Fig.23). A complete open DLD device contains a PDMS stamp, two inlet reservoirs, and an additional paper capillary pump with wax lines. For practical use, the sample and buffer are loaded separately in two inlet reservoirs of a pre-wetted PDMS device. The reservoirs allow us to load the device with more sample than if we had we just added the sample as droplets on the surface. By the capillary flow and the sorting mechanism in the DLD array, the sample is sorted into different fractions and collected by the paper. Figure 23A presents the entire process of sorting in an open DLD device. When the sorted fractions stay in the paper, a downstream analysis could be directly conducted or a process of particle extraction could easily be done by vortexing the paper to release the sample. The function of the paper will be explained below.

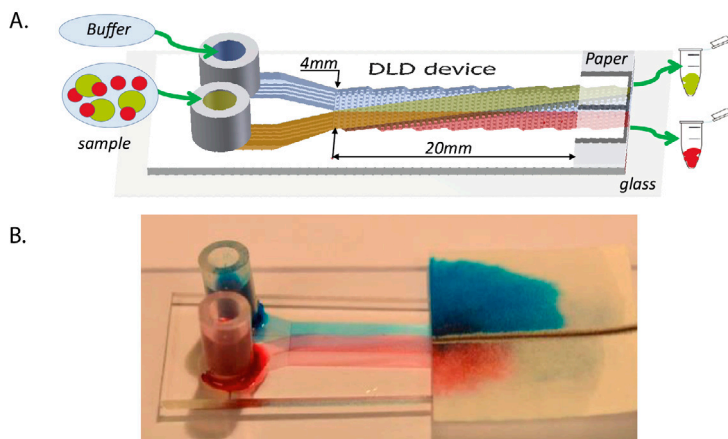


Figure 23. A) An illustration of particle sorting in an open DLD chip. B) A typical device with food colors to present the laminar streams. Images taken from (21). Published by The Royal Society of Chemistry.

A characterization of the liquid profile along the device could be found in three experimental approaches: a macro photography image of the liquid inside the DLD array, a confocal image of 3D liquid volume and a study of the flow in the channel. The results give a better understanding of the flow inside the open DLD channel and confirm that the fluid is confined in an open channel (21). Overall, open channel DLD with new components (reservoirs and paper) are easy to assemble and easy-to-use with particular relevance to applications in resource-poor settings.

To test biological applications, we demonstrated the open DLD technique for a range of mixtures of samples in several different sorting schemes. As a powerful mechanism for size-based sorting, traditional DLD and open DLD perform similarly for blood fractionation (RBCs and WBCs) and cancer cell isolation (MCF7 and RBCs). Figure 24 presents a typical setup of sorting MCF7 from blood and trajectories of two kinds of cells were observed without fluorescence. The RBCs are prevalent at a higher concentration than the MCF7 cells so they can easily be visualized in the paper. To evaluate the purity of sorting, fluorescent dyes were added to both cells in a different experiment (Figure 7 in Paper 1). Morphology-based sorting is another promising aspect of DLD applications. In this study, Trypanosomes were isolated and enriched from RBCs in an open DLD device with depth $9\mu\text{m}$. In another example of open DLD we sorted single cells from clusters of MCF7 cells. A summary of the cell sorting in open DLD is found in figure 24C.

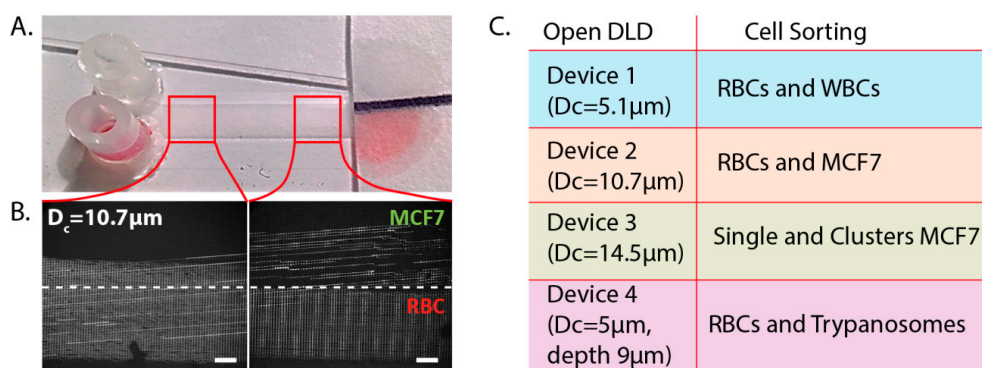


Figure 24. Cell sorting in open DLD chip. A)&B) Sorting MCF7 from blood. C) List of devices and bio-applications. Images taken from (21). Published by The Royal Society of Chemistry.

An additional advantage of open devices is the ease with which they can be cleaned and reused. A closed DLD device, which is sealed to prevent leaking, is hard to clean and reuse when clogging takes place (Fig. 25A and B) while an open device can potentially be reused after a simple cleaning step (Fig. 25C).

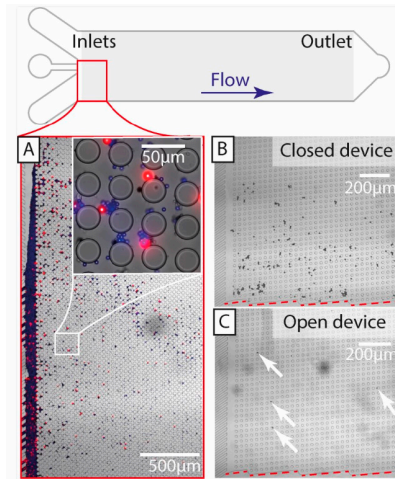


Figure 25. Cleaning and reusing an open DLD chip. A) Clogging in a device. After washing in B) Closed device and C) Open device. Images taken from (21). Published by The Royal Society of Chemistry.

In some cases, the adhesion issue could give a benefit for particle sorting. For an example of forensic cases, RBCs and WBCs need to be separated from contaminated blood samples including soils and dust (Fig.26). Due to the small contaminant sizes, they cannot be filtered out by a filter membrane. Instead, a DLD array having two roles has been tested. The first array traps the contaminants, while the second one is used to sort the remaining RBCs and WBCs. With a negative charge of the PDMS surface, the small sized soil and dust particles were trapped in several first rows, while RBCs and WBCs pass through this section to be continuously sorted according to the main function of DLD.

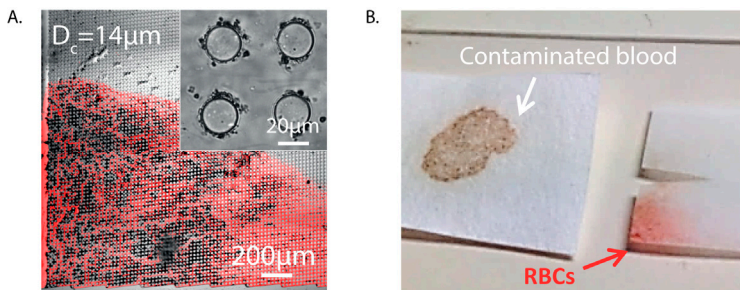


Figure 26. Contaminated blood is purified by passing through the array. Images taken from (21). Published by The Royal Society of Chemistry.

We have successfully demonstrated that open channel DLD devices assembled with capillary paper pumps are promising portable tools for particle and cell sorting. In terms of size-based sorting and morphology-based sorting as well as potential to integrate with other techniques, such as electrokinetics and paper fluidics, we have shown that open channel DLD has the potential to open up for new applications.

Paper fluidics

As a passive technique, DLD is an open platform to integrate or combine with other techniques in a whole system. Here, we exploited the capability of both closed and open DLD chip as an integrated and tunable platform.

As mentioned above, the paper plays an important role in an open DLD system. The paper provides a good solution to maintain a continuous flow, which is important to achieve a continuous sorting. As a capillary pump, the paper contributes a negative pressure to increase and stabilize the flow rate (95-98). A study of the flow rate in the open channel DLD as well as in the paper with evaporation taken into account was conducted in different experiments. Compared to the flow driven by the capillary wetting of the paper, the flow due to the hydrostatic pressure of fluid in reservoirs and the absorption rate of paper are significantly less in magnitude. With a paper fluidics geometry that allows the sample to wet the paper in a semicircle or half a semicircle the resulting flow is essentially constant.

Another aspect of paper fluidics is that it is an attractive substrate for various biomedical applications. Paper based lateral flow tests without the need for specialized and costly equipment are commonly used for medical diagnostics, POC tools and home-care testing. Furthermore, paper-based cell culturing has been developed as a promising approach that allows cells to grow in both 2D and 3D cultures. In this study, paper was used as a convenient substrate that is easy to collect, transport or release the sorted sample from in order to pass it to subsequent analysis. In practice, after sorting particles in an open DLD, the paper is cut out into different fractions. The isolated particles are released into suspension by vortexing and collected by spinning (Fig.27).

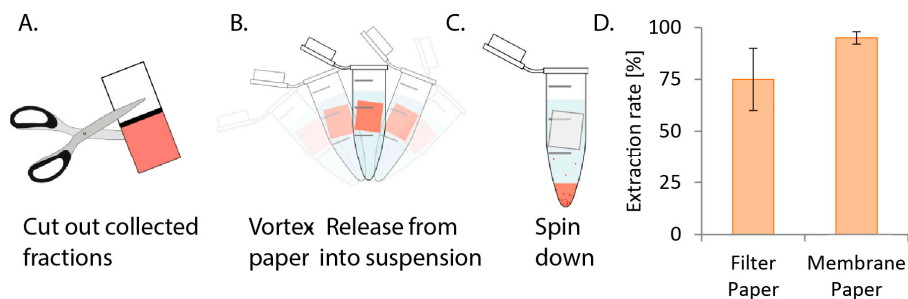


Figure 27. Sample collection from paper fractions. Images taken from (21). Published by The Royal Society of Chemistry.

Various types of paper with different pore sizes, retentions and materials were tested in terms of absorption rate and sample extraction rate. Among these, a filter paper with a good absorption rate was selected for use as a capillary pump and a sandwich paper (filter paper and membrane paper) was applied to increase the sample extraction rate. A comparison of extraction rates is shown in figure 27D. In future work, a bio-compatible paper for cell culture or lateral flow paper could be utilized in the open channel DLD substrate for integrating a series of POC tools.

Device fabrication and sample preparation

Glue-based mold and multi-layer device

From the initial design to a complete device, the fabrication of a microfluidic device is a long procedure with several steps, including design consideration, simulations, fabrication and verification. The process can be resource-intensive, relying on *e.g.* design software, UV-lithography, plasma chamber. In an attempt to reduce the processing effort in soft-lithography and to increase device throughput, we propose a rapid duplication method for PDMS devices in single layers as well as stacks of multilayers.

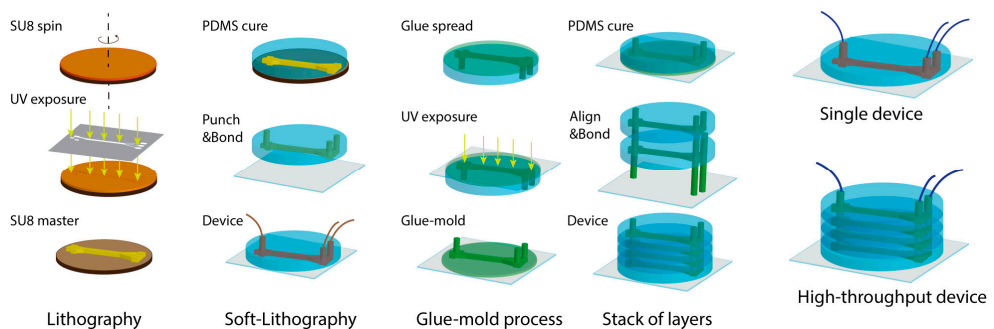


Figure 28. Traditional process of single device fabrication (Lithography and Soft-lithography) and additional method for a stack of layers (glue-based mold and alignment).

Figure 28 shows a brief summary of the device fabrication process which is mainly based on the lithography and soft-lithography processes. In order to protect and extend the lifetime of SU master, a novel method to create a secondary mold has been developed. In our work, a secondary mold made of UV-curable glue is introduced instead of PDMS (99) or Epoxy materials (100), with the advantage of high-resolution replication and no need of anti-sticking treatment.

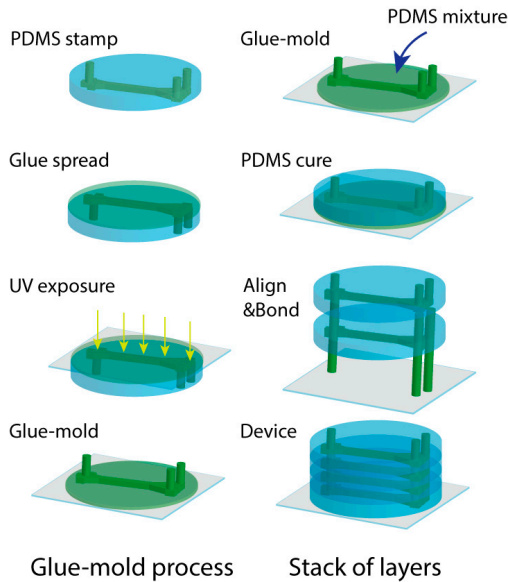


Figure 29. Process of glue-based mold fabrication and alignment step of a stack of layers.

A PDMS stamp duplicated directly from SU-8 master was used to fabricate a secondary mold in the process (Fig.29). After curing, a glue-based mold is used for PDMS replicas. Furthermore, a new approach based on alignment pins for quickly aligning PDMS multilayers is simplifying the process of making a high-throughput devices (Fig.30).

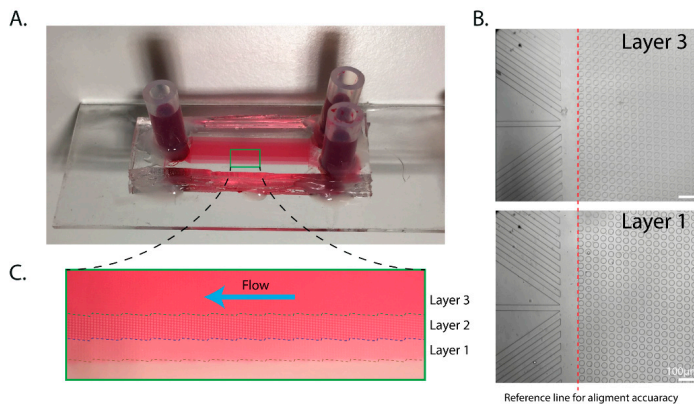


Figure 30. A) A three-layer DLD device with food color. B) Optical images of first and third layer in different focus plans. C) Three layers of devices were observed through the red color. Scale bar 100 μ m.

PDMS device fabrication

The masters for the DLD arrays were fabricated via UV lithography. In a contact mask aligner (Karl Suss MJB3 and MJB4, Munich, Germany), negative photoresist SU8 (MicroChem, Newton, MA, USA) spun on a 3" silicon wafer was exposed to UV light through a chrome-mask designed in L-Edit 11.02 (Tanner Research, Monrovia, CA USA) and printed by Delta Mask (Delta Mask, Enschede, The Netherlands). Before casting of PDMS, a monolayer of 1H,1H,2H,2H-perfluorooctyl trichlorosilane (ABCR GmbH & Co. KG, Karlsruhe, Germany) was applied in the gas phase to the master as an anti-adhesion agent to facilitate demolding. A 10:1 mixture (monomer : curing agent) of PDMS (Sylgard 184, Dow Corning, Midland, MI, USA) was degassed, poured onto the master and then baked for 2 hours at 80°C.

For the closed devices, PDMS stamps are punched and an oxygen plasma treatment step (Plasmatic Systems, Inc., North Brunswick, NJ, USA) is performed to enable bonding to glass slides. Silicone tubes for fluidic connections are glued to the device with silicone glue (Elastosil AO7, RTV-1 silicone rubber, Wacker Silicones, Munich, Germany). For the open device, the PDMS stamps are directly assembled with a paper pump, with or without reservoirs. A comparison of the protocols of the two fabrications is presented in Supplementary of paper 1 (Open channel DLD for particle and cell sorting).

Paper fabrication

Single and two-layer paper systems were used as capillary pumps and for sample capture and collection. For liquid absorption (Herzberg flow rate 110sec/100ml), a filter paper of 0.15mm thickness, a 25-60µm pore size and 8µm particle retention (Grade 600, VWR, Sweden) was used. For sample capture, a layer of polycarbonate paper (Grade 28158, VWR, Sweden), (0.1µm pore size) was sandwiched between the separation device and the lower grade filter paper. Wax barriers were printed onto the filter paper using a wax printer (ColorQube 8570, Xerox, USA) followed by baking for 3 minutes at 100° C.

Sample preparation

Fluorescently labelled polystyrene microspheres with varying diameters (from 1µm to 20µm) (Polyscience Inc.) were suspended in milliQ water and 1% SDS, and used in both closed and open DLD devices for calibration.

Soft polyacrylamide particles (diameter $15 \pm 0.84\mu\text{m}$, Young's modulus 670 ± 280 Pa) obtained from Prof. Guck's lab (TU Dresden, Germany) were used as particle reference in softness sorting in DLD (101).

Small volumes of blood (10 µl) were obtained from healthy, consenting donors via finger pricking. Blood samples were diluted 20 times in autoMACS™ running buffer (Miltenyi Biotech, Auburn, CA).

Trypanosoma cyclops parasites were thawed (after storage in 10% dimethyl sulfoxide (DMSO, Fluka, St Louis, MO: 41639) at -80°C) and cultured in Cunningham's medium 15 with 20% Fetal Calf Serum (FCS, Sigma-Aldrich) at 28°C. Parasites were harvested after proliferating to cover 80% of the culture dish and spiked into blood samples.

MCF-7 (breast carcinoma cell lines obtained from the American Type Culture Collection (ATCC)) was cultured at 37°C and 5% CO₂. Cell culture medium was DMEM, 10%FBS and 1% Penicillin-Streptomycin (Sigma-Aldrich). MCF-7/GFP (breast carcinoma cell lines with Green Fluorescent Protein) (NordicBioSite) was cultured using the same protocol as the non-fluorescent MCF7. MDA-MB-231 (metastasis breast cell lines obtained from the American Type Culture Collection (ATCC)) was cultured at 37°C and 5% CO₂ in a culture medium comprising of DMEM, 10%FBS and 1% Penicillin-Streptomycin.

MCF-10A (human breast cell lines obtained from the American Type Culture Collection (ATCC)) was cultured at 37°C and 5% CO₂ in a culture medium comprising of DMEM, 5% Horse Serum, 20ng/ml Epidermal Growth Factor (EGF), 10ug/mL Insulin, 0.5ug/mL Hydrocortisone, 100ng/mL Cholera Toxin and 1% Penicillin-Streptomycin (Sigma-Aldrich). After one week of culturing, cells reached confluency of approximately 85-90% and were considered ready for separation experiments.

Image Acquisition and analysis

Particle and cell distributions were calculated from images acquired using an inverted epifluorescence microscope (Nikon Eclipse Ti, Nikon Corporation, Tokyo, Japan) and scientific CMOS camera (Flash4.0 V2, Hamamatsu, Japan).

A high-speed camera (MotionBLITZ Eosens mini, Mikrotron GmbH, Unterschleissheim, Germany), capable of capturing 10.000 frames per second, was used to obtain images of the particles and cells at high flow rates (>100ul/min).

ImageJ 1.48v software downloaded from the National Institutes of Health, and NIS-elements 4.51 were used for basic image analysis and the preparation of several of the figures herein. Images of particle trajectories were generated by time-averaging and two-color images generated by adding color to separate images, taken in succession with different filter sets, and superimposing.

Matlab R2014a software was used to write the image analysis code for the specific needs of cell detection, counting and morphology detection.

All error bars of data shown in graphs and figures were calculated by average values and standard deviations of repeated experiments.

Summary of results and outlook

In this thesis, we successfully introduced the open DLD, a portable tool for particle and cell sorting with the capability to sort out various biological samples in terms of size and morphology without external equipment. It was proposed as a potentially useful device for conditions at resource-poor settings. The open DLD method can be further developed and put to use by integrating a reliable downstream method for identification of the sorted cells, for instance paper fluidics with specific antibodies to realize a lateral flow diagnostic device.

In another example of cell sorting, we demonstrate that deformability can be an interesting bio-marker, especially when size and morphology based sorting are not sufficient to extract the specific cancer cells of interest. We have also introduced cell deformation measurements in DLD devices. The results show a significant difference of deformability among cell lines of MCF7, MCF10A and MDA-MB-231 cells. A proof-of-principle of cancer cell sorting using MCF7 and MDA-MB-231 cells is illustrative for deformability-based sorting using DLD. However, the work on isolation of cancer cells from the normal cells is still not yet finished. Furthermore, a comparison of DLD and FACS will give a better understanding of cell characteristics. In future work, more relevant cancer cells, *e.g.* clinical samples, are planned to be sorted using our techniques. To characterize the metastatic potential of the different sub-populations of the cells, transplantation of the sorted fractions in terms of size, morphology, deformability will be explored. To better understand and predict deformability sorting, better theories need to be developed. Two approaches of tuning cell separation have been introduced in different applications: a combination of electrokinetics and DLD for tuning RBCs rotation and device deformation by controlling driving pressure for particle separation. Finally, the application of UV-curable glue moulds for rapid duplication and alignment of multilayer microfluidic sorting devices was presented as an interesting method for device fabrication. While we have shown proof of principle for a range of new methods, further optimization is required to fully benefit from these approaches.

Paper 1. Open DLD channel for particles and cell sorting

We show separation of biologically relevant particles, on patterned surfaces that are reusable, based on a variety of relevant parameters such as size and shape, without the need for external pumps. DLD has proven to be a powerful tool for bio-separations, and here we show proof of principle of an open DLD device that is easier to fabricate, reusable, simpler and therefore potentially cheaper, without using any external pumps. Our approach is relevant for applications in medicine, biological research, and forensics for sample preparation and purification. The potential low cost, ease of use and non-reliance on external equipment makes it particularly suitable for fieldwork, not least in challenging environments such as the developing world.

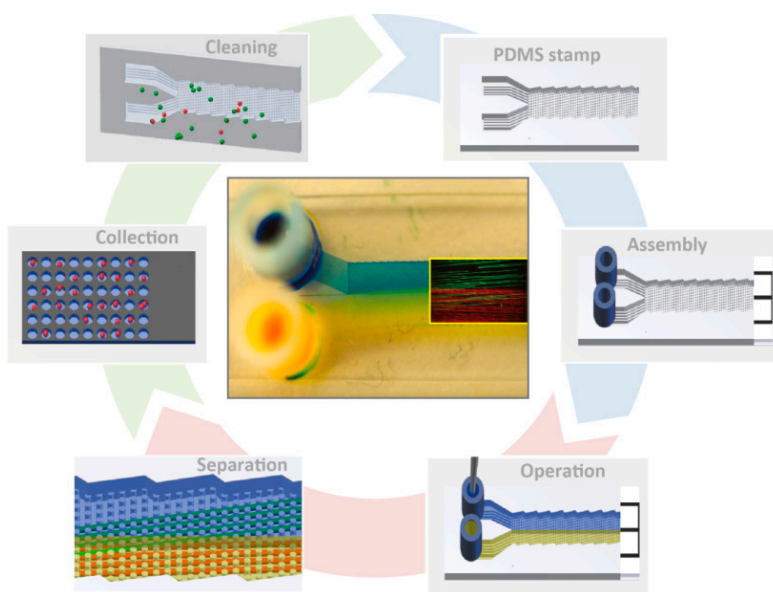


Figure 31. Graphical abstract for the Open DLD approach: fabrication, operation, particle separation and collection to cleaning and reuse.

Paper 2. Softness sorting for cancer cells in deterministic lateral displacement

Due to their direct association with the physiology of cells, physical properties are especially attractive as markers for sorting and characterization of cancer cells. Where molecular surface markers are lacking, the physical properties can instead serve as inherent markers for separation. This is especially interesting for cancer cells as softer cells are known to be more metastatic than hard cells. We have successfully demonstrated and measured the deformability of normal breast cells (MCF10A) and breast cancer cells (MCF7 and MDA-MB-231) using DLD devices. We find that the MDA-MB-231 cells are deformed more than 10% at the highest flow rates and that they are completely separated from the relatively much harder non-malignant cell type MCF10A. Proof of principle of sorting based on deformability has been shown between MDA-MB-231 and MCF7 cells and we will continue utilizing it for other cell types and further applications.

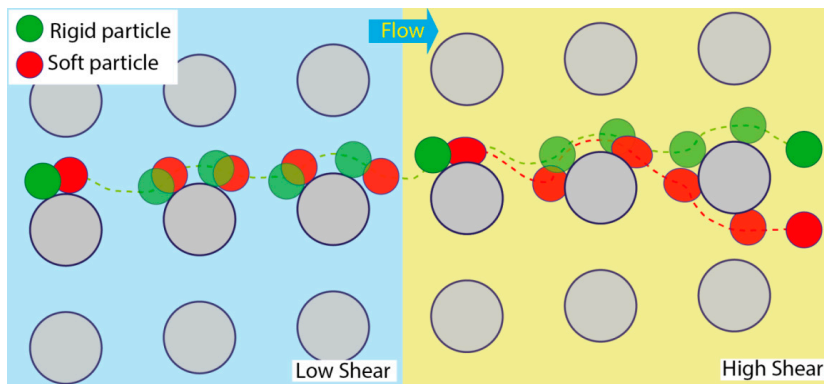


Figure 32. Schematic of deformability-based sorting. While both rigid and soft particles displace at low pressure, the soft ones shift to zig-zag mode at higher pressure.

Paper 3. Electrokinetic rotation of Red blood cells in DLD devices

Morphological separation in DLD relies on the controlled orientation of the particles of interest. Previous work has demonstrated orientation by confining the flow in the vertical direction. However, that may limit the achievable throughput. In this paper, instead of depth control, an alternative of applying a low frequency AC voltage (100 Hz) of a nominal value of $177 V_{RMS}/cm$ in a DLD device is demonstrated to control the orientation of the RBCs. By this method, the device will not be limited in depth, and we open up for higher throughput. An application of isolation of trypanosome parasite is the planned future work of this study.

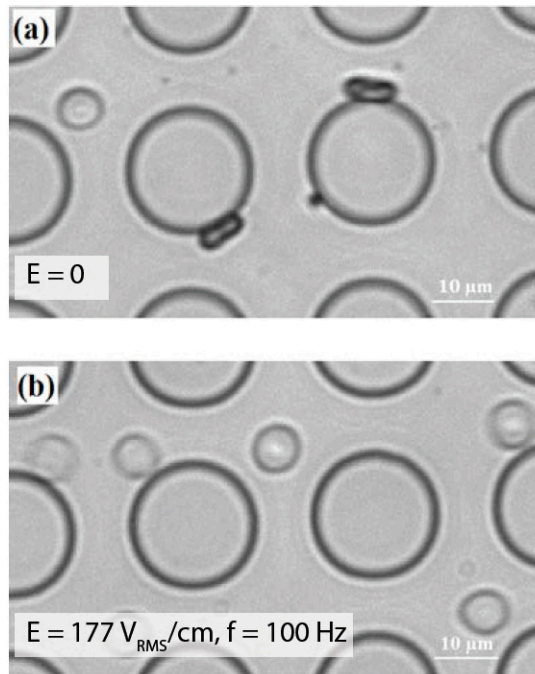


Figure 33. Effect of electric field on orientation of RBCs in a DLD device. a) In the absence of an electric field, when the cells travel close to the pillars, they will lean against the pillars with their width, exhibiting a small effective size. b) RBC rotation due to the effect of an applied voltage.

Paper 4. Rapid duplication and alignment for multilayers of microfluidic PDMS devices

In the soft-lithography process, PDMS stamps are duplicated many times from an SU8 master. This is associated with risks of damage to the master which in turn may cause waste of time and effort to redo the lithography process for the master. We have demonstrated a new method of duplicating a secondary master or mold using optical glue. The method has been developed to eliminate a punching step for fluidic access that is a standard step in conventional protocols of soft lithography. Furthermore, the capability of easily stacking multilayers of devices by alignment pins opens up for high throughput applications for PDMS devices.

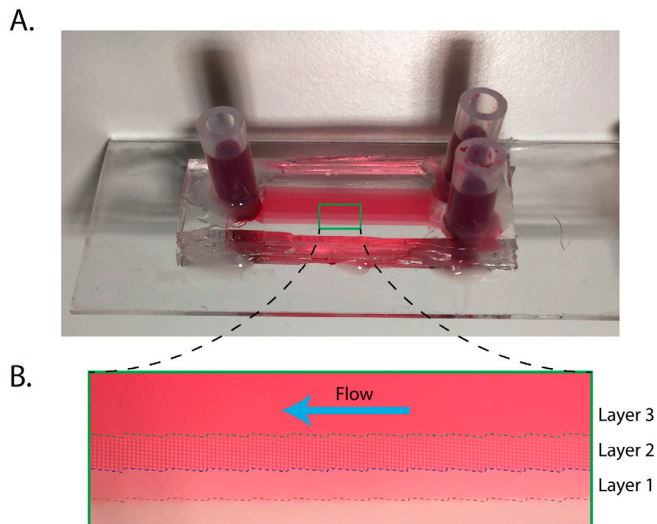


Figure 34. Multilayers of a DLD device which are duplicated and aligned by a glue-based mold. A) An overview of the whole device. B) Food color helps to identify different layers of the device.

Paper 5. Tunable separation in deterministic lateral displacement by pressure control on varying PDMS stiffness

In practice, many sorting experiments require careful optimization for obtaining high purity separations. As an attempt towards tunable particle separation in ongoing experiments, we carefully characterized the effects of deformation and the deformation of DLD devices by controlling the driving pressure. To avoid the effects of the elasticity of the PDMS, preparation was optimized with respect to mixing ratio, curing temperature and device thickness.

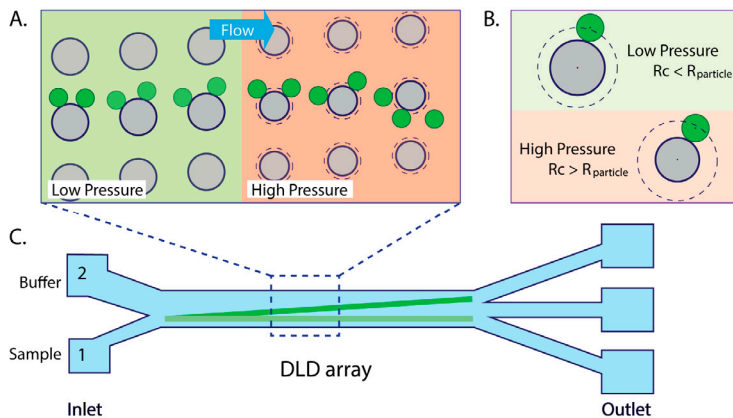
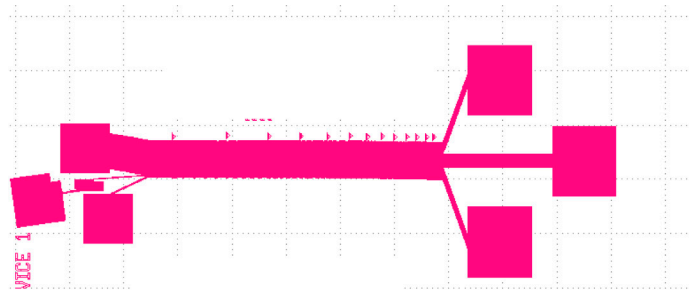


Figure 35. Tunable separation in a DLD device. A) PDMS post deformation at high pressure. B) Particle trajectory tuned from displacement to zigzag mode. C) A sketch of the DLD device.

Appendix

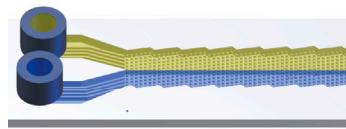
- DLD devices which were used mainly in Paper 2 & Paper 5 (multiple critical sizes). The device was designed by Stefan Holm.



Gap	[Grid]															
Dc	In 1	In 2	IN 3													
	<7.82	7.82	8.91	10.13	10.95	11.95	13.09	13.93	15.03	15.99	17	17.95	19	19.98	>20	
	Outlet RE1		Outlet RE2		Outlet RE3			Outlet RE4		Outlet RE5		Outlet RE6				

Figure 36. DLD design and critical sizes.

- DLD device which is used in Paper 1 (Single critical size).



Open DLD device

Device	Dpost	Gap	Dc	Depth
1	30	11	5.1	24
2	30	23	10.7	24
3	30	31	14.4	24
4	20	12	5	24
5	20	12	5	9

Unit: μm

Figure 37. Open DLD and all used devices.

- Different built-in interfaces in Matlab programming were used to analyze the data.
 - –The scripts for size and shape measurement of cells (Fig. 38) as well as particle counting were developed by Thuy-Dung Nguyen.
 - –Extraction of specific features of cells of interest, which was used for single cell measurement has been created by Vuong D. Nguyen and associate prof. Ha T. Le (HMI Laboratory, Vietnam National University, Hanoi, Vietnam) (Fig.39).

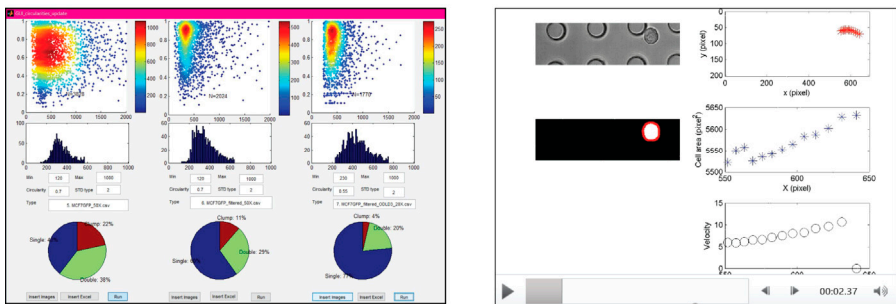


Figure 38. GUI for size and shape measurement.

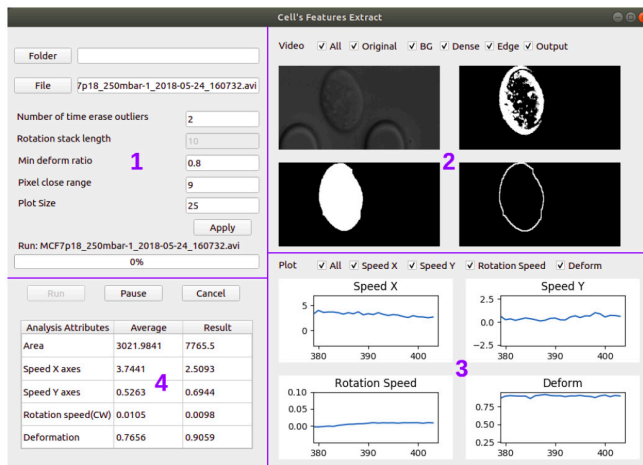


Figure 39. GUI for extraction of specific features of cells of interest.

References

1. Pappas D (2016) Microfluidics and cancer analysis: cell separation, cell/tissue culture, cell mechanics, and integrated analysis systems. *Analyst* 141(2):525-535.
2. Halldorsson S, Lucumi E, Gomez-Sjoberg R, & Fleming RMT (2015) Advantages and challenges of microfluidic cell culture in polydimethylsiloxane devices. *Biosensors & bioelectronics* 63:218-231.
3. Tsai HF, Trubelja A, Shen AQ, & Bao G (2017) Tumour-on-a-chip: microfluidic models of tumour morphology, growth and microenvironment. *J R Soc Interface* 14(131).
4. Khan ZS & Vanapalli SA (2013) Probing the mechanical properties of brain cancer cells using a microfluidic cell squeezer device. *Biomicrofluidics* 7.
5. Kim YC, Park SJ, & Park JK (2008) Biomechanical analysis of cancerous and normal cells based on bulge generation in a microfluidic device. *Analyst* 133(10):1432-1439.
6. Otto O, *et al.* (2015) Real-time deformability cytometry: on-the-fly cell mechanical phenotyping. *Nature methods* 12(3):199-202, 194 p following 202.
7. Huh D, Gu W, Kamotani Y, Grotberg JB, & Takayama S (2005) Microfluidics for flow cytometric analysis of cells and particles. *Physiol Meas* 26(3):R73-98.
8. Haik Y, Pai V, & Chen CJ (1999) Development of magnetic device for cell separation. *Journal of magnetism and magnetic materials* 194:254-261.
9. Pappas D & Wang K (2007) Cellular separations: a review of new challenges in analytical chemistry. *Analytica chimica acta* 601(1):26-35.
10. Di Carlo D, Irimia D, Tompkins RG, & Toner M (2007) Continuous inertial focusing, ordering, and separation of particles in microchannels. *Proceedings of the National Academy of Sciences of the United States of America* 104(48):18892-18897.
11. Huang LR, Cox EC, Austin RH, & Sturm JC (2004) Continuous particle separation through deterministic lateral displacement. *Science* 304(5673):987-990.
12. Gossett DR, *et al.* (2010) Label-free cell separation and sorting in microfluidic systems. *Analytical and bioanalytical chemistry* 397(8):3249-3267.
13. Pamme N (2007) Continuous flow separations in microfluidic devices. *Lab on a chip* 7(12):1644-1659.

14. Yamada M, Nakashima M, & Seki M (2004) Pinched flow fractionation: Continuous size separation of particles utilizing a laminar flow profile in a pinched microchannel. *Analytical chemistry* (76):5465-5471.
15. Giddings JC (1966) A New Separation Concept Based on a Coupling of Concentration and Flow Nonuniformities. *Separation Science* 1(1):123-125.
16. Laurell T, Petersson F, & Nilsson A (2007) Chip integrated strategies for acoustic separation and manipulation of cells and particles. *Chemical Society reviews* 36(3):492-506.
17. Harrison DJ, *et al.* (1993) Micromachining a Miniaturized Capillary Electrophoresis-Based Chemical Analysis System on a Chip. *Science* 261(5123):895-897.
18. Pethig R, Menachery A, Pells S, & De Sousa P (2010) Dielectrophoresis: a review of applications for stem cell research. *J Biomed Biotechnol* 2010:182581.
19. Davis JA, *et al.* (2006) Deterministic hydrodynamics: taking blood apart. *Proceedings of the National Academy of Sciences of the United States of America* 103(40):14779-14784.
20. Holm SH, Beech JP, Barrett MP, & Tegenfeldt JO (2011) Separation of parasites from human blood using deterministic lateral displacement. *Lab on a chip* 11(7):1326-1332.
21. Tran TSH, Ho BD, Beech JP, & Tegenfeldt JO (2017) Open channel deterministic lateral displacement for particle and cell sorting. *Lab on a chip* 17(21):3592-3600.
22. Loutherbach K, Puchalla J, Austin RH, & Sturm JC (2009) Deterministic microfluidic ratchet. *Phys Rev Lett* 102(4):045301.
23. Loutherbach K, *et al.* (2010) Improved performance of deterministic lateral displacement arrays with triangular posts. *Microfluidics and Nanofluidics* 9(6):1143-1149.
24. Loutherbach K, *et al.* (2012) Deterministic separation of cancer cells from blood at 10 mL/min. *AIP Adv* 2(4):42107.
25. Liu Z, *et al.* (2013) Rapid isolation of cancer cells using microfluidic deterministic lateral displacement structure. *Biomicrofluidics* 7(1):11801.
26. Zhang Z, Henry E, Gompper G, & Fedosov DA (2015) Behavior of rigid and deformable particles in deterministic lateral displacement devices with different post shapes. *The Journal of chemical physics* 143(24):243145.
27. D'Silva J, Austin RH, & Sturm JC (2015) Inhibition of clot formation in deterministic lateral displacement arrays for processing large volumes of blood for rare cell capture. *Lab on a chip* 15(10):2240-2247.
28. Liu Z, *et al.* (2015) Microfluidic cytometric analysis of cancer cell transportability and invasiveness. *Scientific reports* 5:14272.
29. Liu Z, *et al.* (2018) Integrated Microfluidic Chip for Efficient Isolation and Deformability Analysis of Circulating Tumor Cells. *Advanced Biosystems* 2(10):1800200.

30. Wei J, *et al.* (2015) Numerical Study of Pillar Shapes in Deterministic Lateral Displacement Microfluidic Arrays for Spherical Particle Separation. *IEEE Trans Nanobioscience* 14(6):660-667.
31. Zeming KK, Ranjan S, & Zhang Y (2013) Rotational separation of non-spherical bioparticles using I-shaped pillar arrays in a microfluidic device. *Nature communications* 4:1625.
32. Ranjan S, Zeming KK, Jureen R, Fisher D, & Zhang Y (2014) DLD pillar shape design for efficient separation of spherical and non-spherical bioparticles. *Lab on a chip* 14(21):4250-4262.
33. Au SH, *et al.* (2017) Microfluidic Isolation of Circulating Tumor Cell Clusters by Size and Asymmetry. *Scientific reports* 7(1):2433.
34. Karabacak NM, *et al.* (2014) Microfluidic, marker-free isolation of circulating tumor cells from blood samples. *Nat Protoc* 9(3):694-710.
35. Hyun J-c, Hyun J, Wang S, & Yang S (2017) Improved pillar shape for deterministic lateral displacement separation method to maintain separation efficiency over a long period of time. *Separation and Purification Technology* 172:258-267.
36. Inglis DW (2009) Efficient microfluidic particle separation arrays. *Applied Physics Letters* 94(0313510).
37. Vernekar R, Kruger T, Loutherbach K, Morton K, & D WI (2017) Anisotropic permeability in deterministic lateral displacement arrays. *Lab on a chip* 17(19):3318-3330.
38. Kulrattanak T, *et al.* (2011) Mixed motion in deterministic ratchets due to anisotropic permeability. *Journal of colloid and interface science* 354(1):7-14.
39. Kulrattanak T, van der Sman RGM, Schroën CGPH, & Boom RM (2010) Analysis of mixed motion in deterministic ratchets via experiment and particle simulation. *Microfluidics and Nanofluidics* 10(4):843-853.
40. Kim SC, *et al.* (2017) Broken flow symmetry explains the dynamics of small particles in deterministic lateral displacement. *Proceedings of the National Academy of Sciences of the United States of America* 10(1074):5034-5041.
41. Holm SH, Beech JP, Barrett MP, & Tegenfeldt JO (2016) Simplifying microfluidic separation devices towards field-detection of blood parasites. *Anal. Methods* 8(16):3291-3300.
42. Campos-Gonzalez R, *et al.* (2018) Deterministic Lateral Displacement: The Next-Generation CAR T-Cell Processing? *SLAS Technol* 23(4):338-351.
43. Civin CI, *et al.* (2016) Automated leukocyte processing by microfluidic deterministic lateral displacement. *Cytometry. Part A : the journal of the International Society for Analytical Cytology* 89(12):1073-1083.
44. Wunsch BH, *et al.* (2019) Gel-on-a-chip: continuous, velocity-dependent DNA separation using nanoscale lateral displacement. *Lab on a chip* 19(9):1567-1578.

45. Wunsch BH, *et al.* (2016) Nanoscale lateral displacement arrays for the separation of exosomes and colloids down to 20 nm. *Nature nanotechnology* 11(11):936-940.
46. Laki AJ, *et al.* (2014) Microvesicle fractionation using deterministic lateral displacement effect. *Proceedings of the 9th IEEE International Conference on Nano/Micro Engineered and Molecular Systems*:490-493.
47. Laki AJ, Botzheim L, Iván K, Tamási V, & Civera P (2014) Separation of Microvesicles from Serological Samples Using Deterministic Lateral Displacement Effect. *BioNanoScience* 5(1):48-54.
48. Beech JP, *et al.* (2018) Separation of pathogenic bacteria by chain length. *Analytica chimica acta* 1000:223-231.
49. Zheng S, Yung R, Tai YC, & Kasdan H (2005) Deterministic lateral displacement MEMS device for continuous blood separation. *18th IEEE International Conference on Micro Electro Mechanical Systems* (2005):851-854.
50. Zheng S, Tai YC, & Kasdan H (2005) A micro device for separation of Erythrocytes and Leukocytes in human blood. *Proceedings of the 2005 IEEE Engineering in medicine and biology 27th annual conference* 1024-1027.
51. Inglis DW, *et al.* (2008) Determining blood cell size using microfluidic hydrodynamics. *Journal of immunological methods* 329(1-2):151-156.
52. Inglis DW, Lord M, & Nordon RE (2011) Scaling deterministic lateral displacement arrays for high throughput and dilution-free enrichment of leukocytes. *Journal of Micromechanics and Microengineering* 21(5):054024.
53. Holmes D, *et al.* (2014) Separation of blood cells with differing deformability using deterministic lateral displacement(dagger). *Interface focus* 4(6):20140011.
54. Kruger T, Holmes D, & Coveney P (2014) Deformability-based red blood cell separation in deterministic lateral displacement devices - A simulation study. *Biomicrofluidics* 8(054114-2).
55. Chen Y, Silva J, Austin RH, & Sturm JC (2015) Microfluidic chemical processing with on-chip washing by deterministic lateral displacement arrays with separator walls. *Biomicrofluidics* 9(054105).
56. Henry E, *et al.* (2016) Sorting cells by their dynamical properties. *Scientific reports* 6:34375.
57. Zeming KK, Salafi T, Chen CH, & Zhang Y (2016) Asymmetrical Deterministic Lateral Displacement Gaps for Dual Functions of Enhanced Separation and Throughput of Red Blood Cells. *Scientific reports* 6:22934.
58. Chou CY, Lu YT, Cahng CM, & Liu CH (2018) Selectively capturing monocytes from whole blood on microfluidic biochip for sepsis dianosis. *Proceedings of the 13th IEEE international conference on Nano/Micro Engineered and molecular systems*:56-59.
59. Zeng Y, *et al.* (2018) Microfluidic enrichment of plasma cells improves treatment of multiple myeloma. *Mol Oncol* 12(7):1004-1011.

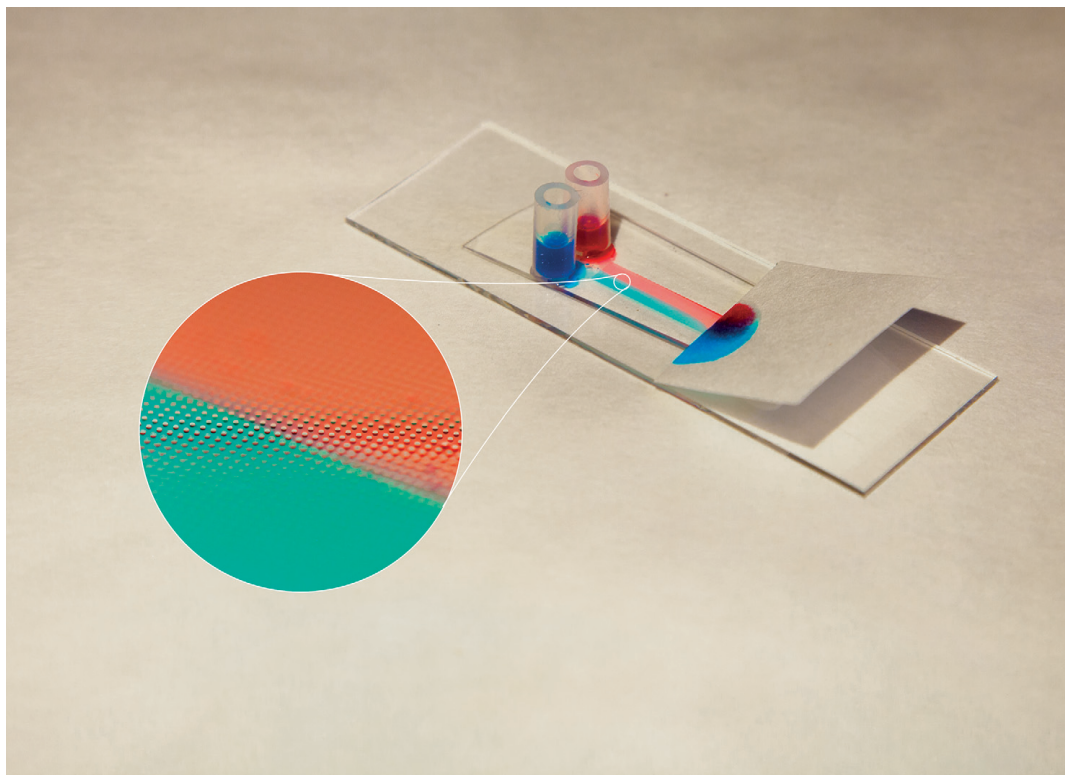
60. Kabacaoğlu G & Biros G (2018) Sorting same-size red blood cells in deep deterministic lateral displacement devices. *Journal of Fluid Mechanics* 859:433-475.
61. Li N, Kamei DT, & Ho CM (2007) On-Chip continuous blood cell subtype separation by deterministic lateral displacement. *Proceedings of the 2nd IEEE International conference on Nano/Micro engineered and molecular system*:932-936.
62. Inglis DW, *et al.* (2008) Microfluidic device for label-free measurement of platelet activation. *Lab on a chip* 8(6):925-931.
63. Morton KJ, *et al.* (2008) Crossing microfluidic streamlines to lyse, label and wash cells. *Lab on a chip* 8(9):1448-1453.
64. Huang R, *et al.* (2008) A microfluidics approach for the isolation of nucleated red blood cells (NRBCs) from the peripheral blood of pregnant women. *Prenat Diagn* 28(10):892-899.
65. Green JV, Radisic M, & Murthy SK (2009) Deterministic Lateral Displacement as a Means to Enrich Large Cells for Tissue Engineering. *Anal. Chem* 81(21):9178-9182.
66. Zhang B, Green JV, Murthy SK, & Radisic M (2012) Label-free enrichment of functional cardiomyocytes using microfluidic deterministic lateral flow displacement. *PLoS One* 7(5):e37619.
67. Tottori N, Nisisako T, Park J, Yanagida Y, & Hatsuzawa T (2016) Separation of viable and nonviable mammalian cells using a deterministic lateral displacement microfluidic device. *Biomicrofluidics* 10(014125).
68. Joensson HN, Uhlen M, & Svahn HA (2011) Droplet size based separation by deterministic lateral displacement-separating droplets by cell-induced shrinking. *Lab on a chip* 11(7):1305-1310.
69. Tottori N, Hatsuzawa T, & Nisisako T (2017) Separation of main and satellite droplets in a deterministic lateral displacement microfluidic device. *RSC Advances* 7(56):35516-35524.
70. Inglis DW, Herman N, & Vesey G (2010) Highly accurate deterministic lateral displacement device and its application to purification of fungal spores. *Biomicrofluidics* 4(2).
71. Khodae F, Movahed S, Fatourae N, & Daneshmand F (2015) Numerical Simulation of Separation of Circulating Tumor Cells from Blood Stream in Deterministic Lateral Displacement (DLD) Microfluidic Channel. *Journal of Mechanics* 32(04):463-471.
72. Okano H, *et al.* (2015) Enrichment of circulating tumor cells in tumor-bearing mouse blood by a deterministic lateral displacement microfluidic device. *Biomedical microdevices* 17(3):9964.
73. Zhou J, *et al.* (2019) Isolation of circulating tumor cells in non-small-cell-lung-cancer patients using a multi-flow microfluidic channel. *Microsystems & Nanoengineering* 5(1).
74. Sarioglu AF, *et al.* (2015) A microfluidic device for label-free, physical capture of circulating tumor cell clusters. *Nature methods* 12(7):685-691.

75. Holm SH, J.P B, & Tegenfeldt JO (2013) Combined density and size-based sorting in deterministic lateral displacement devices *17th International conference on miniaturized systems for chemistry and life sciences*:1224-1226.
76. Beech JP & Tegenfeldt JO (2008) Tuneable separation in elastomeric microfluidics devices. *Lab on a chip* 8(5):657-659.
77. Beech JP, Jonsson P, & Tegenfeldt JO (2009) Tipping the balance of deterministic lateral displacement devices using dielectrophoresis. *Lab on a chip* 9(18):2698-2706.
78. Beech JP & Tegenfeldt JO (2009) Capillary driven separation on patterned surfaces. *Thirteenth International Conference on Miniaturized Systems for Chemistry and Life Sciences*:785-787.
79. Jiang M, Mazzeo AD, & Drazer G (2016) Centrifuge-based deterministic lateral displacement separation. *Microfluidics and Nanofluidics* 20(1).
80. Du S & Drazer G (2016) Gravity driven deterministic lateral displacement for suspended particles in a 3D obstacle array. *Scientific reports* 6:31428.
81. Hanasoge S, Devendra R, Diez FJ, & Drazer G (2014) Electrokinetically driven deterministic lateral displacement for particle separation in microfluidic devices. *Microfluidics and Nanofluidics* 18(5-6):1195-1200.
82. Hanahan D & Weinberg RA (2000) The hallmarks of cancer. *Cell* 100:57-70.
83. Guck J, *et al.* (2005) Optical deformability as an inherent cell marker for testing malignant transformation and metastatic competence. *Biophysical journal* 88(5):3689-3698.
84. Ribeiro AJ, Khanna P, Sukumar A, Dong C, & Dahl KN (2014) Nuclear stiffening inhibits migration of invasive melanoma cells. *Cell Mol Bioeng* 7(4):544-551.
85. Kuznetsova TG, Starodubtseva MN, Yegorenkov NI, Chizhik SA, & Zhdanov RI (2007) Atomic force microscopy probing of cell elasticity. *Micron* 38(8):824-833.
86. Li QS, Lee GY, Ong CN, & Lim CT (2008) AFM indentation study of breast cancer cells. *Biochem Biophys Res Commun* 374(4):609-613.
87. Dokukin ME, Guz NV, & Sokolov I (2013) Quantitative study of the elastic modulus of loosely attached cells in AFM indentation experiments. *Biophysical journal* 104(10):2123-2131.
88. Guz N, Dokukin M, Kalaparthy V, & Sokolov I (2014) If cell mechanics can be described by elastic modulus: study of different models and probes used in indentation experiments. *Biophysical journal* 107(3):564-575.
89. Musielak M (2009) Red blood cell-deformability measurement: review of techniques. *Clin Hemorheol Microcirc* 42(1):47-64.
90. McFaul SM, Lin BK, & Ma H (2012) Cell separation based on size and deformability using microfluidic funnel ratchets. *Lab on a chip* 12(13):2369-2376.
91. Dressaire E & Sauret A (2017) Clogging of microfluidic systems. *Soft matter* 13(1):37-48.

92. Wong I & Ho CM (2009) Surface molecular property modifications for poly(dimethylsiloxane) (PDMS) based microfluidic devices. *Microfluid Nanofluidics* 7(3):291-306.
93. Berthier J, Brakke KA, & Berthier E (2016) *Open Microfluidics* (Wiley).
94. Morton K, *et al.* (2010) The anti-lotus leaf effect in nanohydrodynamic bump arrays. *New Journal of Physics* 12(8):085008.
95. Fu E, Ramsey SA, Kauffman P, Lutz B, & Yager P (2011) Transport in two-dimensional paper networks. *Microfluid Nanofluidics* 10(1):29-35.
96. Osborn JL, *et al.* (2010) Microfluidics without pumps: reinventing the T-sensor and H-filter in paper networks. *Lab on a chip* 10(20):2659-2665.
97. Li X, Ballerini DR, & Shen W (2012) A perspective on paper-based microfluidics: Current status and future trends. *Biomicrofluidics* 6(1):11301-1130113.
98. Glavan AC, *et al.* (2013) Rapid fabrication of pressure-driven open-channel microfluidic devices in omniphobic R(F) paper. *Lab on a chip* 13(15):2922-2930.
99. Yang L, Hao X, Wang C, Zhang B, & Wang W (2013) Rapid and low cost replication of complex microfluidic structures with PDMS double casting technology. *Microsystem Technologies* 20(10-11):1933-1940.
100. Olmos CM, *et al.* (2019) Epoxy resin mold and PDMS microfluidic devices through photopolymer flexographic printing plate. *Sensors and Actuators B: Chemical* 288:742-748.
101. Girardo S, *et al.* (2018) Standardized microgel beads as elastic cell mechanical probes. *Journal of Materials Chemistry B* 6(39):6245-6261.

Paper I





Featuring work from NanoLund, Prof. Jonas O. Tegenfeldt, Lund University, Sweden

A simple, low-cost and robust approach was developed for sorting complex samples using open-architecture fluidics. The liquid flow was driven by a paper capillary pump that doubles as a reservoir for collection of the sorted fractions.

Open channel deterministic lateral displacement for particle and cell sorting

Image reproduced by permission of Jason Beech/Tegenfeldt group

As featured in:



See Jonas O. Tegenfeldt et al.,
Lab Chip, 2017, 17, 3592.



rsc.li/loc

Registered charity number: 207890



Cite this: *Lab Chip*, 2017, 17, 3592

Open channel deterministic lateral displacement for particle and cell sorting†

Trung S. H. Tran,  Bao D. Ho,  Jason P. Beech  and Jonas O. Tegenfeldt *

We present the use of capillary driven flow over patterned surfaces to achieve cheap and simple, but powerful separation of biologically relevant particle systems. The wide use of microfluidics is often hampered by the propensity for devices to clog due to the small channel sizes and the inability to access the interior of devices for cleaning. Often the devices can only be used for a limited duration and most frequently only once. In addition the cost and power requirements of flow control equipment limits the wider spread of the devices. We address these issues by presenting a simple particle- and cell-sorting scheme based on controlled fluid flow on a patterned surface. The open architecture makes it highly robust and easy to use. If clogging occurs it is straightforward to rinse the device and reuse it. Instead of external mechanical pumps, paper is used as a capillary pump. The different fractions are deposited in the paper and can subsequently be handled independently by simply cutting the paper for downstream processing and analyses. The sorting, based on deterministic lateral displacement, performs equivalently well in comparison with standard covered devices. We demonstrate successful separation of cancer cells and parasites from blood with good viability and with relevance for diagnostics and sample preparation. Sorting a mixture of soil and blood, we show the potential for forensic applications.

Received 6th July 2017,
Accepted 18th September 2017

DOI: 10.1039/c7lc00707h

rscl.li/loc

Introduction

Cell separation is a critical process in cell biology, disease diagnostics and prognosis. While standard techniques such as FACS and MACS are widely used, there is a need to miniaturize systems in order to minimize sample and reagent use, simplify systems for the user, and integrate components into comprehensive analysis tools. Depending on the exact applications, different types of microfluidic sorting schemes may be utilized. Inertial¹ and acoustophoretic methods² give high volumetric throughput but with a relatively low size resolution and must be operated at low particle concentrations. Deterministic lateral displacement (DLD) is a method of particle separation, based on the continuous flow of particles through an array of obstacles that exhibits exceptional resolution in size-based separations.³ DLD has been used for cell and bio-particle separations such as blood fractionation,^{4–8} trypanosome enrichment from blood,^{9,10} cancer cell isolation^{11–13} and CTC cell cluster isolation from whole blood,¹⁴ DNA and exosome separation,¹⁵ and the separation of cells based on parameters other than size, namely shape and

deformability,^{16,17} and dielectric properties.¹⁸ Early theoretical work by Inglis *et al.*¹⁹ and Davis *et al.*²⁰ describing the critical size in DLD arrays has been improved upon by studying the effects of post shape.^{21,22} Further improvements to theoretical descriptions have been made by considering other parameters such as diffusion,²³ dynamical properties,¹⁷ and alternative trajectories through DLD arrays.^{23–25} Being a passive method its basic operation does not require any application of external fields, like those used in acoustophoresis, and because it functions at high particle concentrations and low flow rates, relevant throughput can be achieved without the pressures required to generate the high particle velocities needed for inertial-effect based approaches. Even at high volume flow rates (10 mL min⁻¹) DLD has been shown to separate a variety of cells with minimal effect on viability.¹² Taken together, these qualities make DLD our method of choice for the development of a simple, cheap but effective approach to particle separation.

Here we show that by removing the lid of the DLD devices and using capillary flow we are able to perform separations, equally powerful as those in closed devices, but with many added advantages. While the benefits of open fluidics in general^{26,27} and of capillary driven DLD has been demonstrated previously,^{28,29} we here show proof of principle of their usefulness for sorting of biologically relevant particles not only based on size but also based on morphology and dielectric properties with relevance for *e.g.* medical diagnostics and

NanoLund and Division of Solid State Physics, Physics Department, Lund University, PO Box 118, 221 00, Lund, Sweden. E-mail: jonas.tegenfeldt@ftf.lth.se; Tel: +46 46 222 8063

† Electronic supplementary information (ESI) available. See DOI: 10.1039/c7lc00707h

forensics. What is more, this can be done in devices that are cheaper and easier to fabricate, since oxygen plasma and bonding is not required, and also cheaper and easier to run since pressure controllers are not required. A common limitation of standard fluidics devices, based on sealed small channels, is a propensity to clog, especially when handling complex samples. The difficulties to clean these closed devices make them unsuitable for prolonged and repeated use. We show that our open devices are easy to clean and reuse, which together with the use of the paper capillary pumps further contributes to the lowering of the costs. While standard pumps and pressure control units are ultimately more versatile, they are bulky, power consuming and expensive. We show that paper capillary pumps are compatible with open DLD devices allowing us to handle larger volumes than can fit into a device alone, and that they have the added advantage of doubling as sample collection substrates, further simplifying downstream process steps and analyses.

Results and discussion

Device fabrication and assembly

Both open and closed devices are fabricated in PDMS using replica molding on SU8 masters (see Materials and methods section). The final step in fabricating closed devices is to bond a glass slide to the PDMS cast and to then attach fluidics connectors. Open devices are much simpler in that they require neither of these two last steps. In order for the open device to function, PDMS must be rendered hydrophilic using *e.g.* oxygen plasma or, alternatively, prewetted by submersion in water. Fig. S3† in the supplementary material shows an overview of hydrophobic, hydrophilic and pre-wetted devices. Pre-wetting is much simpler to perform and negates the requirement of an oxygen plasma system, helping to keep the method cheap and simple. When a device is submerged in water the device features (channels and arrays) will fill with water after 5 minutes. When the PDMS slab is removed from submersion, water runs off of all flat areas and the only liquid remaining is that which is trapped within the patterned areas constituting the device. Sample can now be applied to the inlets and paper to the outlets and the sample will flow through the patterned areas of the device, confined to within the defined height of the features.

DLD devices in open configuration

Fig. 1A and B show a typical configuration of a closed DLD device. PDMS is bonded to glass to form closed channels and a pump or pressure control unit is used to drive flow through the device. As shown in Fig. 1C and D, our approach is to remove the glass lid and replace the pressure-driven flow with capillary flow. Provided the channels are hydrophilic, any aqueous solution placed at the inlet of the device will flow into the channels until they are filled. For our typical DLD devices (*e.g.* device 1, 20 mm length, 4 mm width and 24 μm depth, see ESI† Fig. S1) the array volume is approximately 1.1 μL .

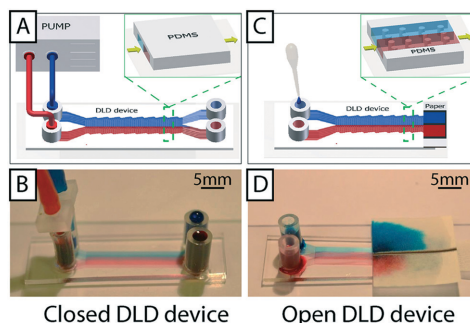


Fig. 1 Comparison of closed and open devices. (A and B) Conventional closed device where fluid is confined inside channels in a complicated setup of tubes and a pump or a pressure control unit. (C and D) Open DLD without lid. In these devices the interplay between surface tension and geometry keeps the fluid confined to the separation array and a paper reservoir at the outlet maintains flow, via capillary action, and collects the sample. We see, by observing the red and blue food coloring, that the flow is laminar in both devices.

To run the device, reservoirs are mounted at the device inlets and tested for volumes up to 60 μL using the paper capillary pump. At the beginning of the device there is a transition in liquid height from the reservoir to the bulk of the separation array. In this transition zone the sample flows across the top of the array, but the liquid height falls to that of the posts within 1–5 mm. Fig. 1D shows how we are able to maintain a stable, laminar flow (of red and blue food dye in this case) in the device using the paper capillary pump. The figure also shows how the fluids are collected in the paper. The resulting flow rates are measured to be $71 \pm 19 \text{ nL s}^{-1}$, which is comparable to what we achieve with an applied pressure of 21 mBar in a corresponding closed device. This also compares well with a closed device driven by a paper capillary pump.

The liquid in the reservoirs gives a hydrostatic pressure that is less than 1 mBar and is therefore negligible in comparison with the equivalent driving pressure in a closed device. The result is that the liquid is pulled through the device by the negative pressure imposed by the capillary pump, minimizing any liquid build-up on top of the posts.

To estimate the liquid profile along the device we resorted to three approaches. Direct imaging (Fig. 2A and B) indicates that the liquid is indeed thicker at the beginning of the device close to the reservoirs and that it levels out rather quickly away from the reservoirs. Confocal imaging supports the conclusion giving a direct view of the profile (Fig. 2C–F). Finally we studied the flow in the channels. We measure the velocities of the flow (Fig. S4B†) and combine that with the cross sectional area of the device based on the design parameters to obtain a value of the volumetric flow. The resulting flow rate is consistent with what we obtain in direct measurements of the volumetric flow rate (Fig. S5†) and measurements of the average flow by measuring the elapsed time

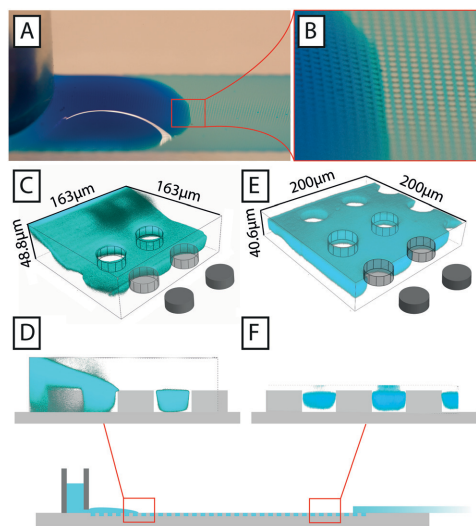


Fig. 2 Images of aqueous fluids in an open DLD device. A) Photograph of an aqueous solution of food color in an open device. B) Close-up of the transition between the area where the fluid forms a droplet and where it is confined to the post array. C) and D) 3d rendering and cross section, respectively, of confocal images of an aqueous solution of FITC in the same device, taken near to the reservoir. The drop formed by the reservoir can be seen to fall below the height of the posts. E) and F) 3d rendering and cross section, respectively, at the end of the device closest to the paper. The device is filled with liquid but no liquid can be seen above the posts.

between loading of a defined volume and the emptying of the reservoirs (Fig. S4D†) suggesting that the liquid is indeed filling the device to the top of the pillars. Note that there is a trend of lower flow velocities close to the reservoirs, in line with the local buildup of liquid on top of the post array that we observe by direct inspection.

The throughput of the paper capillary pump driven device is ultimately limited by the absorption rate of the paper. In a very simplified but illustrative picture the paper capillary pump can be viewed as a battery with an internal resistance and a hydromotive force in analogy to standard electrical batteries. If the external load is much less than the internal flow resistance, the flow rate is limited by the internal resistance. By measuring the flow rates in a free paper as well as a paper connected to a device (Fig. S5†), we could estimate the internal resistance, $16 \times 10^{12} \text{ kg s}^{-1} \text{ m}^{-4}$, which is within an order of magnitude of the resistance of our closed devices, $30 \times 10^{12} \text{ kg s}^{-1} \text{ m}^{-4}$ (from Fig. S4†), and open devices $23 \times 10^{12} \text{ kg s}^{-1} \text{ m}^{-4}$ (from Fig. S5†). From these data we could also estimate the hydromotive force to 32 mBar. Higher throughputs can now be realized by decreasing the device flow resistance through an increase in the depth of the devices or by using paper pumps with higher absorption rates. While the flow in narrow strips of paper follows the Washburn law³⁰ such that

the flow rate is inversely proportional to the square root of time, we use wider strips of paper where the liquid fans out leading to a constant flow rate as shown by Mendez *et al.*³¹ To obtain specific volumes and flow rates as a function of time, the paper capillary pumps can be programmed by selecting appropriate geometries of the paper.^{32–34} Further details on the flow generated in our open devices by the paper capillary pump can be found in the ESI.†

In addition to the simplifications compared to standard DLD devices we can demonstrate good separation performance. Fig. 3B shows the separation of 3 μm and 7 μm polystyrene microspheres. The sample (a mixture of the two beads) was placed in one inlet and buffer placed in the other. As the sample stream flows through the device, in parallel with the buffer stream, the mechanism of DLD causes the 7 μm particles, which are larger than the critical size, D_c , to be displaced into the buffer stream while the 3 μm particles, which are smaller than D_c remain in the sample stream. This lateral displacement is caused by steric interactions between particles and posts, which cause particles to move with a component perpendicular to the flow direction. The net result is the continuous, spatial separation of particles, Fig. 3B, in this case based on size. We also show here how the particles are collected in the paper, in regions divided by wax lines, which we will return to below. Despite the lack of a lid in our open DLD devices, flow is well defined and confined to the pillar array, and high-resolution separations can be performed fully comparable to those demonstrated for closed DLD devices. Fig. 3C shows experimental comparison of 3 devices and 10 particle sizes run in open configurations. Filled circles show particles following the flow (as expected if they are below the critical size) and open circles show those that are displaced (above the critical size). These points fall on either side of the expected critical size (indicated by red double arrows) as calculated using the empiric expressions given by Inglis *et al.*³⁵ and Davis *et al.*²⁰ for closed devices demonstrating good correspondence between particle behavior in open and closed configurations.

Application areas – proof of principle

To show the applicability of open DLD devices to relevant bio-separations, we tested separation of a range of relevant bioparticles in different modalities, as described below.

Size-based separation. Deterministic lateral displacement provides a powerful mechanism for highly precise continuous sorting based on size. In addition to the size-based separation of polystyrene beads shown above (Fig. 3) we show the separation of cells of higher biological relevance. Fig. 4A shows the size-based separation of cells from a breast cancer cell line (MCF7 cells with diameter $17.3 \pm 2.1 \mu\text{m}$) from erythrocytes (red blood cells, RBC) (diameter $7.8 \pm 0.6 \mu\text{m}$) in an open device with $D_c = 10.7 \mu\text{m}$ (device 2, see ESI,† Fig. S1) and Fig. 4B shows the size-based separation of white blood cells (WBC) (diameter $12.2 \pm 0.9 \mu\text{m}$) and RBCs in a device with $D_c = 5.1 \mu\text{m}$ (device 1, see ESI,† Fig. S1). In both cases

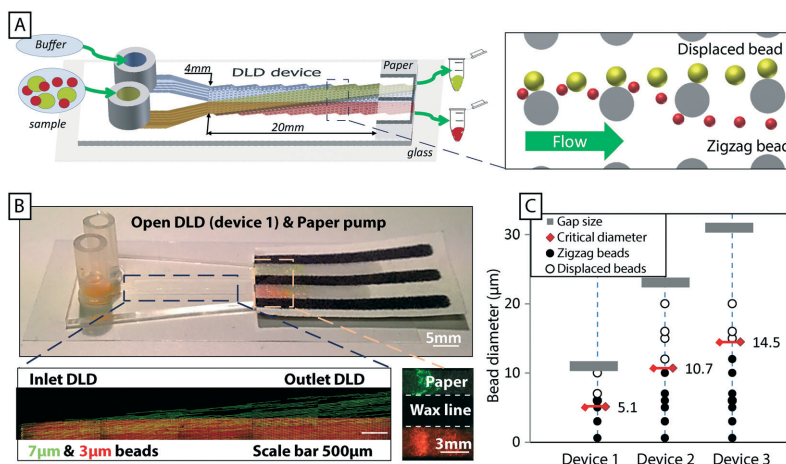


Fig. 3 An overview of open DLD, device layout and typical results. (A) Particles are introduced via one inlet and buffer via the other. The mechanism of deterministic lateral displacement pushes particles (yellow) larger than a critical size, D_c , from the sample stream to the co-flowing buffer stream as they move along the device. Smaller particles (red) remain in the sample stream. (B) Paper is used both as a capillary pump and as a method of sample collection. Here colored beads are visualized after separation and collection in zones in the paper pump defined with wax (yellow/green 7 μm and red 3 μm , black lines are wax). Time averaged images of fluorescent beads (green 7 μm and red 3 μm) in the beginning and end of the device show the trajectories of the beads in the device, which lead to separation. Note the collection of particles in separate, wax-delimited zones in the paper. (C) The behavior of open DLD devices is consistent with that of standard closed DLD devices. The red double arrows indicate theoretical critical sizes for a conventional closed device based on Davis' estimate.²⁰ The results for the open DLD are shown with filled black circles for particles in zigzag mode (following the flow), and open circles for particles in displacement mode (displaced into the buffer stream). The grey bars indicate the upper limit of the particle sizes as imposed by the gap sizes between the posts.

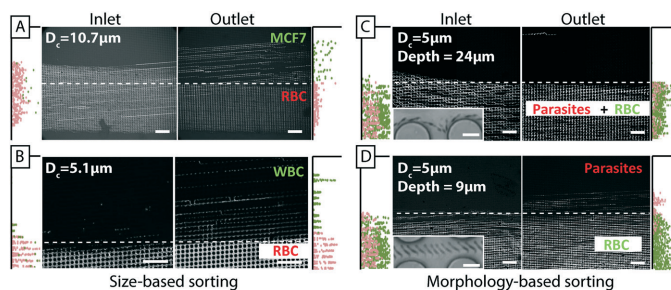


Fig. 4 Cell and parasite sorting in open DLD devices. All images show plots of inlet distributions (to the left) and outlet distributions (to the right) together with time-averaged micrographs of different cells moving through open DLD devices. The micrographs show the trajectories of the different cells in each case and the outlet distributions show the resulting separations. (A) Size-based separation of RBCs (red dots) and MCF7 cells (green dots) (B) Sizebased sorting of RBCs (red dots) and WBCs (green dots) (C) in a 24 μm deep device RBCs (green dots) and parasites (*T. cyclops*) (red dots) have the same trajectories, but in a shallower device (9 μm deep) (D) they are separated. Scale bars 100 μm and 10 μm for the insets.

the performance of the devices in the simpler open configuration is equivalent to that of the same device with a lid and pressure-driven flow.

Morphology-based separation. To leverage the differences in morphology of bioparticles as a separation parameter, DLD devices can be made in which the orientation of non-spherical particles is controlled. In this way a specific aspect of the shape can be selected to influence the effective size of the particles.^{9,36} As in previous work, but now in the open de-

vice, we control the orientation of parasites to optimize their separation from erythrocytes. In a 24 μm deep device 4 (Fig. 4C), both RBCs and parasites follow the flow, whereas in a 9 μm deep device 5 (Fig. 4D) RBCs follow the flow but parasites are displaced and separation is achieved based on the same principle as was shown in ref. 9 and 36. Device parameters are shown in ESI,† Fig. S1.

Complex samples. We demonstrate the robustness of the open DLD by introducing a mixture of soil and blood into a

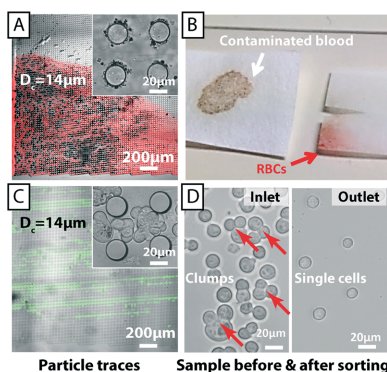


Fig. 5 Sorting of complex samples in open DLD devices. Even if large particles become trapped at the beginning of a device they do not block the flow of liquid and smaller particles as they would in a closed device. This allows extremely “dirty” samples to be analysed. A mixture of soil and RBCs is introduced into an open device. Despite the large amount of soil particles trapped at the beginning of the device (A), a clean fraction of RBCs is collected at the end of the device (B). (C) & (D) A combination of filtering and continuous separation of suspensions of cells containing large clusters that would otherwise block the inlets of a closed device.

device (Fig. 5). Soil sediments quickly and sticks in the separation array, as can be seen in Fig. 5A, but this does not cause the flow to stop. RBCs are still able to traverse the post array and a soil free fraction of RBCs is readily collected in paper at the end of the device (Fig. 5B).

A common challenge in microfluidics is the aggregation of cells that often lead to clogging even with careful surface passivation. Using the open DLD we clearly demonstrate the retention of cell aggregates of MCF7 cells while the individual cells are collected at the end of the device (Fig. 5C and D). While cell aggregates may be of interest in their own right,³⁷ in many cases, such as in cell culturing, drug screening and fluorescence activated cell sorting, it is often necessary to remove cell aggregates. Those experiments are conducted in device 3 with $D_c = 14 \mu\text{m}$ (see ESI† Fig. S1).

Application of electric fields

Electrokinetic effects can be utilized in DLD devices to widen the scope and add specificities associated with the distribution of charge on the particles of interest as shown previously by Beech *et al.*¹⁸ in closed DLD devices. We added electrodes to the inlet and outlet reservoirs of a DLD device generating an electric field in the device. The electric field lines were “squeezed” between the insulating PDMS posts and field gradients were generated near the post surfaces. Polarizable particles interacted with the field gradient and the resulting dielectrophoretic (DEP) forces were used to modify the DLD-based behavior and tune size-based separations. Because there is no lid on an open device it is easy to access the fluid at any point in the device, during a separation. In the exam-

ple shown in Fig. 6 electrodes are dipped into the fluid (KCl with a conductivity of 24 mS m^{-1}) and an AC electric field is applied. In a closed device the electrodes are usually mounted in the inlet and outlet reservoirs, which are 30 mm apart in this device. Here we could easily place them 3 mm apart allowing for the generation of much higher fields at a given voltage. In Fig. 6B we see the effects of adding an electric field. In the absence of an applied voltage, $3.1 \mu\text{m}$ sulphate-terminated polystyrene and $4.8 \mu\text{m}$ carboxy-terminated polystyrene microspheres are following the flow (zigzagging), which is to be expected in a device with a critical diameter of $5.1 \mu\text{m}$ (device 1, see ESI† Fig. S1), showing that the electrodes do not greatly perturb the flow. At 400 V applied AC voltage (100 Hz) the $4.8 \mu\text{m}$ microspheres are displaced and separation is achieved. At 700 V, all microspheres are displaced.

Applying electrodes in this manner, rather than in the inlets and outlets, decouples the electrode geometry from the flow geometry in a very simple way, giving us freedom to apply any number of electrodes in any pattern and at any angle to the flow direction.

Sample collection and recovery

The paper at the end of the device functions not only as a capillary pump but also as a sample recovery matrix from which fractions can be cut in a manner similar to that shown by Osborn *et al.*³⁸ Filter paper with a thickness of $150 \mu\text{m}$ and a pore size of $25\text{--}60 \mu\text{m}$ has excellent absorption. Liquid reservoirs of the required volume can be defined using a wax printer. The wax lines serve to maintain the separation of collected fractions (Fig. 1, 3 and 7). Fluorescent samples with good signal can be imaged directly in the paper with low magnification (Fig. 3 and 7). For samples with lower, or no fluorescent signal, higher magnification together with transmitted light can be used to image cells. In Fig. 7 separated MCF7 cells and RBCs are imaged inside the paper reservoirs.

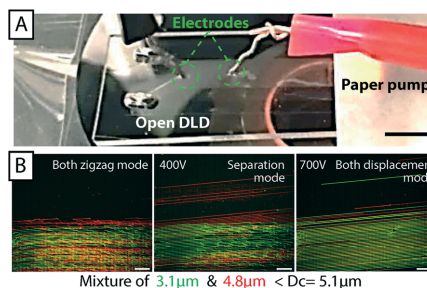


Fig. 6 Combination of electrokinetics and open DLD. (A) With direct access to the fluid it is straight-forward to position external electrodes at any point in the device. Scale bar 3 mm. An AC field at 100 Hz and various applied voltages (B) 0 V/400 V/700 V, change the trajectories of particles consistent with what was previously shown by Beech *et al.*¹⁸ in closed DLD devices. Scale bars 100 μm .

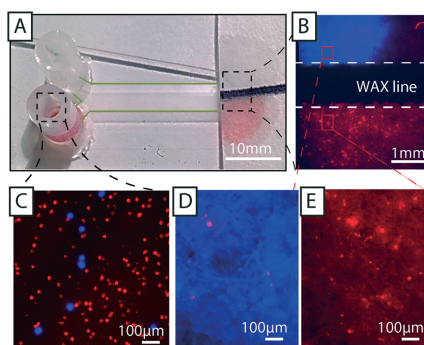


Fig. 7 Paper functions both as a capillary pump and as a collection reservoir for separated cells. (A and C) A sample containing RBCs (red fluorescence) and MCF7 cells (blue fluorescence) is introduced into an open DLD. RBCs (smaller than D_c) and MCF7 cells (larger than D_c) follow different trajectories through the device (from left to right) and can be collected to the right in two areas on the paper, separated by a printed wax line. The RBCs are more numerous than the MCF7 cells and can easily be seen in the paper through their red color (no fluorescence). Note the green dotted line that delineates the borders of the device. (B) Trapped MCF7 cells and RBCs imaged in the paper. The high concentration makes it difficult to pick out individual cells in the image, but as (D) shows, very few RBCs were observed in the top zone where the MCF7 fraction dominates. (E) No MCF7 cells are seen in the RBC fraction.

To recover cells from the paper, we have developed a simple protocol that does not negatively affect viability or proliferation (Fig. 8). The desired fractions are cut out of the paper and placed inside a liquid medium of choice

(e.g. in a 1.5 mL Eppendorf tube). Gentle vortexing releases most of the collected sample from the paper and subsequent centrifugation may then be performed to concentrate and/or collect the freed cells or particles. Fig. 8D shows a micrograph of MCF7 cells after separation in an open device, release from paper, and collection *via* centrifugation. Fig. 8E shows the recovery of 75% of cells from filter paper using this method.

While having good absorptive qualities, which is good for maintaining flow, fibrous filter paper with large pore size, is not ideal for sample collection due to trapping of particles and cells within the structure of the paper. Instead a two-layer paper system was used to increase the collection rate. By sandwiching a layer of filter membrane (1 μm pore size, polycarbonate membrane) between the filter paper and the device, the good absorptive qualities of the filter paper could be used while the polycarbonate membrane stopped the particles/cells from entering the paper and becoming trapped. Particles and cells captured on the surface of the polycarbonate membrane were easily resuspended with higher yields observed. Fig. 8E shows how 95% of cells could be recovered using the extra membrane layer.

To measure the effect of sorting in both open and closed devices on the health of cells, we performed viability and proliferation assays of MCF7 cells. Cell counting using viability dyes (trypan blue) was conducted to measure the percentage of viable cells and the rate of proliferation. Fig. 8F demonstrates viabilities of >90% for sorted cells. A small difference in the viability of cells (control, open, and closed devices) could be seen in our measurements but the difference has no practical significance and shows nothing more than the

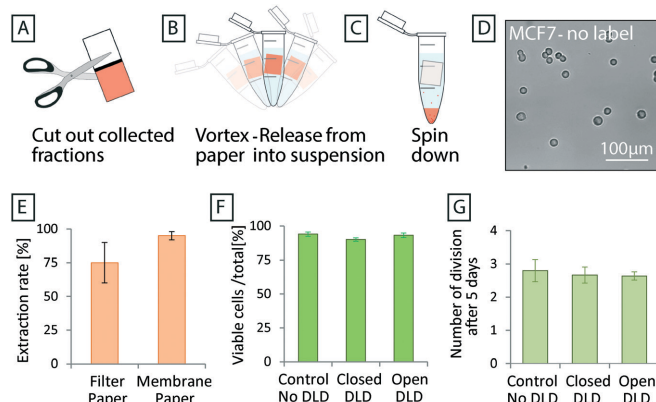


Fig. 8 Post-separation sample recovery. (A) Separated fractions are accumulated in the paper and kept separated by hydrophobic wax lines. The desired fractions are collected separately by dividing the paper along the wax line. (B) To re-suspend the collected fractions vortexing is used, which shakes the cells free of the paper matrix, followed by (C) centrifugation. (D) MCF7 cells after separation and collected using the process described in (A)–(C). (E) Recovery statistics for the filter paper and the two-layer system. Error bars show max/min values from 5 experiments. (F) Cell viability and (G) proliferation assay for MCF7 after separation in closed and open DLD. Error bars show the standard deviation in (F) and (G). No significant difference could be seen in the proliferation rates of sorted and non-sorted cells.

common variation between cultures using these cells. Furthermore, Fig. 8G shows that after 5 days of culturing, no difference in the proliferation rates of cells, (~ 2.5 divisions in 5 days), can be seen as a consequence of sorting.

The performance of the devices is qualitatively comparable to the conventional closed devices with clear separation of the different fractions. Purity and capture rate are performance parameters that do not depend on the DLD as much as on the overall design and will have to be optimized carefully for each specific application. For example the paper capillary pump in Fig. 3B can be extended to three lanes instead of two. In that way the purity of the sample collected in the two extreme lanes can be enhanced by discarding the central lane. The data in Fig. 4 shows clearly that by appropriate choice of cut-offs we would be able to achieve close to 100% purity of the separated fractions. With longer devices, this is expected to be done with minimum loss of capture efficiency.

Cleaning and reusing devices

The fouling of devices with particles and cells is the most common reason for device failure and limits device lifetime. Fouling can be due to several mechanisms. Particles can adhere to surfaces and they can become trapped because they are too large to move through constrictions. These mechanisms are also linked. For example, particles can stick to one another, forming agglomerations that are much more likely to get stuck. Fig. 9A shows an image of 4.5 and 10 μm particles that have become stuck in a closed device with a $D_c = 5.1 \mu\text{m}$ and gap size of 11 μm after operating for 30 min (device 1, see ESI†, Fig. S1). At this point the device has ceased to

work and particles are no longer able to enter the array. This kind of clogging is detrimental for all kinds of microfluidics devices, in particular for DLD devices since a well-defined flow direction is crucial for the successful operation. Even a small deviation of flow direction may change the critical size significantly.

Closed devices are most often irreversibly sealed (to avoid leaking) and are difficult to clean and reuse. Fig. 9B shows the same device after sonication, reversal of the flow direction and an increase in pressure in an effort to remove clogging. Despite these efforts many particles remain stuck in the device and the device is unusable. Open devices are considerably easier to clean and can be cleaned to a much higher degree. Fig. 9C shows the same kind of device as above after first being run in an open configuration and then cleaned by sonication and rinsing. This device is free of particles after rinsing and can be reused.

Conclusion

We have shown that by combining patterned surfaces in PDMS with paper based capillary pumps we can fabricate potentially cheap, simple to use, and reusable continuous flow separation devices. We have demonstrated proof-of-principle separations of samples based on size and morphology and what is more, in samples containing very large contaminant particles. Being open, access to flowing fluid is possible in these devices allowing for easy electric contact through electrodes. Flow rates can be held constant by choice of size and properties of the paper used in the capillary pump. Paper is not only useful as a pump but also as a matrix for the collection of separated fractions. The separational functionality of DLD is retained in open devices paving the way for simple, robust and clogging insensitive sorting using pillar arrays with potential applications in medicine and forensic science. Our device opens up for sample preparation applications in paper fluidics based diagnostics.^{39,40}

The limitations and challenges introduced by working with open devices on the other hand include the risk for evaporation, contamination and biohazard.⁴¹ These issues can be mitigated through a cover that is positioned in close proximity, yet not in contact with the actual device.

Materials and methods

PDMS device fabrication

In a contact mask aligner (Karl Suss MJB3 and MJB4, Munich, Germany), negative photoresist SU8 (MicroChem, Newton, MA, USA) spun on a 3" silicon wafer was exposed with UV light through a chrome-mask designed in L-Edit 11.02 (Tanner Research, Monrovia, CA USA) and printed by Delta Mask (Delta Mask, Enschede, The Netherlands). Before casting of PDMS, a monolayer of 1H,1H,2H,2H-perfluorooctyltrichlorosilane (ABCR GmbH & Co. KG, Karlsruhe, Germany) was applied in the gas phase to the master

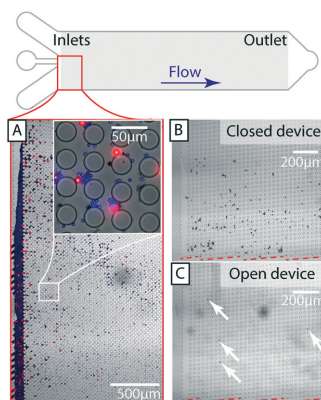


Fig. 9 Cleaning and reusing open DLD devices. (A) Depending on the array parameters, particle sizes and surface chemistries, devices eventually clog. (B) A closed device after attempted cleaning using sonication, high pressures and reversing the flow direction. (C) An open device after sonication and rinsing is almost completely free of particles (30 times fewer). Those remaining are highlighted with arrows. Channel walls are shown in red dashed lines.

as an anti-adhesion agent to facilitate demoulding. A 10:1 mixture (monomer:curing agent) of PDMS (Sylgard 184, Dow Corning, Midland, MI, USA) was degassed, poured onto the master then baked for 2 hours at 80 °C. For the closed devices vias are punched and an oxygen plasma treatment step (Plasma Preen II-862, Plasmatic Systems, Inc., North Brunswick, NJ, USA) is performed to enable bonding to glass slides and the attaching of silicone tubes for fluidic connections, none of which are necessary for the open devices. In Fig. S2† (supplementary of device fabrication), a comparison among a protocol of closed DLD fabrication and optional protocol for open DLD fabrication (with and without oxygen plasma plus reservoir) is presented.

Paper capillary pump

A two-layer paper system was used as a capillary pump and for sample capture and collection for the experiments described in Fig. 8. For liquid absorption (Herzberg flow rate⁴² 110 s/100 mL), filter paper of 0.15 mm thickness, a 25–60 µm pore size and 8 µm particle retention (Grade 600, VWR, Sweden) was used. For sample capture a layer of polycarbonate paper (Grade 28158, VWR, Sweden), (1 µm pore size) was sandwiched between the separation device and the lower grade filter paper. For the other experiments only the filter paper was used. Wax barriers were printed onto the filter paper using a wax printer (ColorQube 8570, Xerox, USA) followed by baking for 3 minutes at 100 °C.

For the experiments characterizing the evaporation, a grid was printed onto the paper to facilitate measurement of the wetted area. The grid was printed using a standard laser writer (Canon iR-ADV C5250i).

Sample preparation (beads, RBCs, WBCs, parasites and MCF7 cells)

Fluorescently labeled polystyrene microspheres with varying diameters (from 1 µm to 20 µm) (Polyscience Inc., Warrington, PA, USA) were suspended in MilliQ water and 1% SDS and used in both closed and open DLD devices for calibration.

Small volumes of blood (10 µL) were obtained from healthy, consenting donors *via* finger pricking. Blood samples were diluted 20 times in autoMACS™ running buffer (Miltenyi Biotec, Auburn, CA, USA).

Trypanosoma cyclops parasites were thawed (after storage in 10% dimethyl sulfoxide (DMSO, Fluka, St. Louis, MO, USA: 41639) at –80 °C) and cultured in Cunningham's medium with 20% fetal calf serum (FCS, Sigma-Aldrich) at 28 °C. Parasites were harvested after proliferating to cover 80% of the culture dish and spiked into blood samples.

MCF-7 (breast carcinoma cell lines obtained from the American Type Culture Collection (ATCC)) was cultured at 37 °C and 5% CO₂. Cell culture medium was Dulbecco's modified Eagle's medium (DMEM), 10% FBS and 1% penicillin streptomycin (Sigma-Aldrich). After one week of subculture,

the cells proliferated to fill more than 80% of the culture flasks and were considered ready for separation experiments.

Image acquisition and analysis

Particle and cell distributions were calculated from images acquired using an inverted epifluorescence microscope (Nikon Eclipse Ti, Nikon Corporation, Tokyo, Japan) and scientific CMOS camera (Flash4.0 V2, Hamamatsu, Japan). ImageJ 1.48v software downloaded from the National Institutes of Health, and NIS-elements 4.51 were used for image analysis and the preparation of figures. Images of particle trajectories are generated by time-averaging. Two color-images generated by adding color to separate images, taken in succession with different filter sets, and superimposing.

Conflicts of interest

There are no conflicts to declare.

Acknowledgements

We thank Stefan Holm and Bo Baldetorp for their kind donation of trypanosomes and MCF-7 cells respectively. This work was carried out within MCF7 at Lund University with funding from the Child Cancer Foundation (MT2013-0031), LAPASO (EU FP7 project 607350) and the Swedish Research Council (VR) grant no. 2015-05426. All device processing was conducted within Lund Nano Lab. We thank Christelle Prinz for valuable comments after carefully reading the manuscript.

References

- 1 D. Di Carlo, D. Irimia, R. G. Tompkins and M. Toner, *Proc. Natl. Acad. Sci. U. S. A.*, 2007, **104**, 18892–18897.
- 2 T. Laurell, F. Petersson and A. Nilsson, *Chem. Soc. Rev.*, 2007, **36**, 492–506.
- 3 L. R. Huang, E. C. Cox, R. H. Austin and J. C. Sturm, *Science*, 2004, **304**, 987–990.
- 4 J. A. Davis, D. W. Inglis, K. J. Morton, D. A. Lawrence, L. R. Huang, S. Y. Chou, J. C. Sturm and R. H. Austin, *Proc. Natl. Acad. Sci. U. S. A.*, 2006, **103**, 14779–14784.
- 5 D. W. Inglis, M. Lord and R. E. Nordon, *J. Microchem. Microeng.*, 2011, **21**, 054024.
- 6 C. I. Civin, T. Ward, A. M. Skelley, K. Gandhi, Z. P. Lee, C. R. Dosier, J. L. D'Silva, Y. Chen, M. Kim, J. Moynihan, X. C. Chen, L. Aurich, S. Gulnik, G. C. Brittain, D. J. Recktenwald, R. H. Austin and J. C. Sturm, *Cytometry, Part A*, 2016, **89A**, 1073–1083.
- 7 K. K. Zeming, T. Salafi, C. H. Chen and Y. Zhang, *Sci. Rep.*, 2016, **6**, 22934.
- 8 M. Yamada, W. Seko, T. Yanai, K. Ninomiya and M. Seki, *Lab Chip*, 2017, **17**, 304–314.
- 9 S. H. Holm, J. P. Beech, M. P. Barrett and J. O. Tegenfeldt, *Lab Chip*, 2011, **11**, 1326–1332.
- 10 S. H. Holm, J. P. Beech, M. P. Barrett and J. O. Tegenfeldt, *Anal. Methods*, 2016, **8**, 3291–3300.

- 11 Z. B. Liu, F. Huang, J. H. Du, W. L. Shu, H. T. Feng, X. P. Xu and Y. Chen, *Biomicrofluidics*, 2013, 7, 011801.
- 12 K. Loutherbach, J. D'Silva, L. Y. Liu, A. Wu, R. H. Austin and J. C. Sturm, *AIP Adv.*, 2012, 2, 042107.
- 13 H. Okano, T. Konishi, T. Suzuki, T. Suzuki, S. Ariyasu, S. Aoki, R. Abe and M. Hayase, *Biomed. Microdevices*, 2015, 17, 59.
- 14 S. H. Au, J. Edd, A. E. Stoddard, K. H. K. Wong, F. Fachin, S. Maheswaran, D. A. Haber, S. L. Stott, R. Kapur and M. Toner, *Sci. Rep.*, 2017, 7, 2433.
- 15 B. H. Wunsch, J. T. Smith, S. M. Gifford, C. Wang, M. Brink, R. L. Bruce, R. H. Austin, G. Stolovitzky and Y. Astier, *Nat. Nanotechnol.*, 2016, 11, 936–940.
- 16 J. P. Beech, S. H. Holm, K. Adolfsson and J. O. Tegenfeldt, *Lab Chip*, 2012, 12, 1048–1051.
- 17 E. Henry, S. H. Holm, Z. M. Zhang, J. P. Beech, J. O. Tegenfeldt, D. A. Fedosov and G. Gompper, *Sci. Rep.*, 2016, 6, 34375.
- 18 J. P. Beech, P. Jonsson and J. O. Tegenfeldt, *Lab Chip*, 2009, 9, 2698–2706.
- 19 D. W. Inglis, J. A. Davis, R. H. Austin and J. C. Sturm, *Lab Chip*, 2006, 6, 655–658.
- 20 J. A. Davis, *Doctoral thesis*, Princeton, 2008.
- 21 Z. Zhang, E. Henry, G. Gompper and D. A. Fedosov, *J. Chem. Phys.*, 2015, 143, 243145.
- 22 K. Loutherbach, K. S. Chou, J. Newman, J. Puchalla, R. H. Austin and J. C. Sturm, *Microfluid. Nanofluid.*, 2010, 9, 1143–1149.
- 23 B. R. Long, M. Heller, J. P. Beech, H. Linke, H. Bruus and J. O. Tegenfeldt, *Phys. Rev. E*, 2008, 78, 046304.
- 24 J. Frechette and G. Drazer, *J. Fluid Mech.*, 2009, 627, 379–401.
- 25 S. C. Kim, B. H. Wunsch, H. Hu, J. T. Smith, R. H. Austin and G. Stolovitzky, *Proc. Natl. Acad. Sci. U. S. A.*, 2017, 114, E5034–E5041.
- 26 J. Melin, W. van der Wijngaart and G. Stemme, *Lab Chip*, 2005, 5, 682–686.
- 27 B. P. Casavant, E. Berthier, A. B. Theberge, J. Berthier, S. I. Montanez-Sauri, L. L. Bischel, K. Brakke, C. J. Hedman, W. Bushman, N. P. Keller and D. J. Beebe, *Proc. Natl. Acad. Sci. U. S. A.*, 2013, 110, 10111–10116.
- 28 J. P. Beech and J. O. Tegenfeldt, Capillary driven separation on patterned surfaces, *microTAS 2009, The 13th International Conference on Miniaturized Systems for Chemistry and Life Sciences*, Jeju, Korea, November 1–5, 2009, pp. 785–787.
- 29 K. Morton, O. K. C. Tsui, C. K. Tung, J. C. Sturm, S. Y. Chou and R. Austin, *New J. Phys.*, 2010, 12, 085008.
- 30 E. W. Washburn, *Phys. Rev.*, 1921, 17, 273–283.
- 31 S. Mendez, E. M. Fenton, G. R. Gallegos, D. N. Petsev, S. S. Sibbett, H. A. Stone, Y. Zhang and G. P. Lopez, *Langmuir*, 2010, 26, 1380–1385.
- 32 E. Elizalde, R. Urteaga and C. L. Berli, *Lab Chip*, 2015, 15, 2173–2180.
- 33 P. Yager, T. Edwards, E. Fu, K. Helton, K. Nelson, M. R. Tam and B. H. Weigl, *Nature*, 2006, 442, 412–418.
- 34 B. M. Cummins, R. Chinthapatla, B. Lenin, F. S. Ligler and G. M. Walker, *Technology*, 2017, 5, 21–30.
- 35 D. W. Inglis, J. A. Davis, R. H. Austin and J. C. Sturm, *Lab Chip*, 2006, 6, 655–658.
- 36 S. H. Holm, J. P. Beech, M. P. Barrett and J. O. Tegenfeldt, *Anal. Methods*, 2016, 8, 5726–5726.
- 37 A. F. Sarioglu, N. Aceto, N. Kojic, M. C. Donaldson, M. Zeinali, B. Hamza, A. Engstrom, H. Zhu, T. K. Sundaresan, D. T. Miyamoto, X. Luo, A. Bardia, B. S. Wittner, S. Ramaswamy, T. Shioda, D. T. Ting, S. L. Stott, R. Kapur, S. Maheswaran, D. A. Haber and M. Toner, *Nat. Methods*, 2015, 12, 685–691.
- 38 J. L. Osborn, B. Lutz, E. Fu, P. Kauffman, D. Y. Stevens and P. Yager, *Lab Chip*, 2010, 10, 2659–2665.
- 39 Y. Yang, E. Noviana, M. P. Nguyen, B. J. Geiss, D. S. Dandy and C. S. Henry, *Anal. Chem.*, 2017, 89, 71–91.
- 40 K. Yamada, H. Shibata, K. Suzuki and D. Citterio, *Lab Chip*, 2017, 17, 1206–1249.
- 41 Y. Temiz, R. D. Lovchik, G. V. Kaigala and E. Delamarque, *Microelectron. Eng.*, 2015, 132, 156–175.
- 42 W. Herzberg, *Papierprüfung*, Springer, Berlin, Heidelberg, 1921, p. 109, DOI: 10.1007/978-3-662-25211-6_18.

Open Channel Deterministic Lateral Displacement for Particle and Cell Sorting

Trung S.H. Tran, Bao D. Ho, Jason P. Beech and Jonas O. Tegenfeldt

Electronic Supporting Information

Design and fabrication

The basic operational principle of DLD along with relevant parameters and critical separation diameters for our DLD devices are shown in Figure S1.

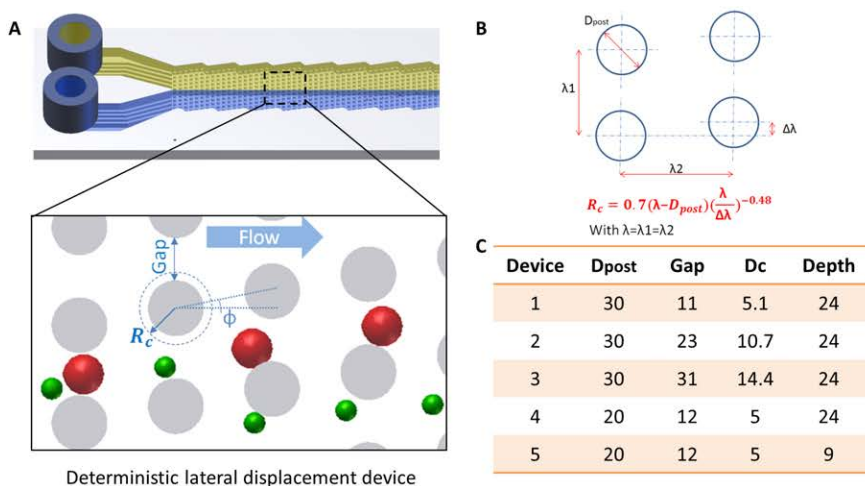


Figure S1. (A) Schematic of a typical DLD device with particle trajectories, (B) Key parameters determining the critical diameter (D_c) of a DLD array, (C) List of DLD devices used in this report (length units are μm). Length of the devices is 20 mm and width is 4 mm.

Several fabrication and surface treatment schemes were tested for our devices (Figure S2). Figure S2A shows the conventional method of fabricating closed PDMS/glass devices with a plasma-bonding step (that also renders the PDMS hydrophilic) and the attachment of reservoirs/pressure control connections.

Preparation of devices

For the open devices, if a drop of aqueous solution is applied at the end of an untreated (hydrophobic) DLD array, the droplet will stay on the surface and will not wet the channels or array area of the device. This can be overcome in two ways. Figure S2B shows an open device in which the channels are selectively rendered hydrophilic by use of a mask during oxygen plasma treatment. The untreated, hydrophobic PDMS surrounding the active area of the device serves to confine the sample, which would otherwise spread outside the features of the device. Another approach, that is simpler because oxygen plasma is not needed, is

shown in Figures S2C and D. By submerging the device in an aqueous solution (1% SDS for polystyrene bead sorting, AutoMacs™ for RBC, and complete Dulbecco's Modified Eagle's Medium (DMEM) for cancer cell experiments) at room temperature for 5 minutes, the entire surface of the device can be forced to wet. When the device is removed from the solution the flat PDMS surface is sufficiently hydrophobic to repel the aqueous solution, but the water inside the structures of the device remains. After the positioning of the paper capillary pump at the outlet and the addition of more sample at the inlet, flow is maintained and separation can be performed. The reservoir, shown in Figure S2D, is not essential but allows for greater control of the sample and the handling of larger sample volumes.

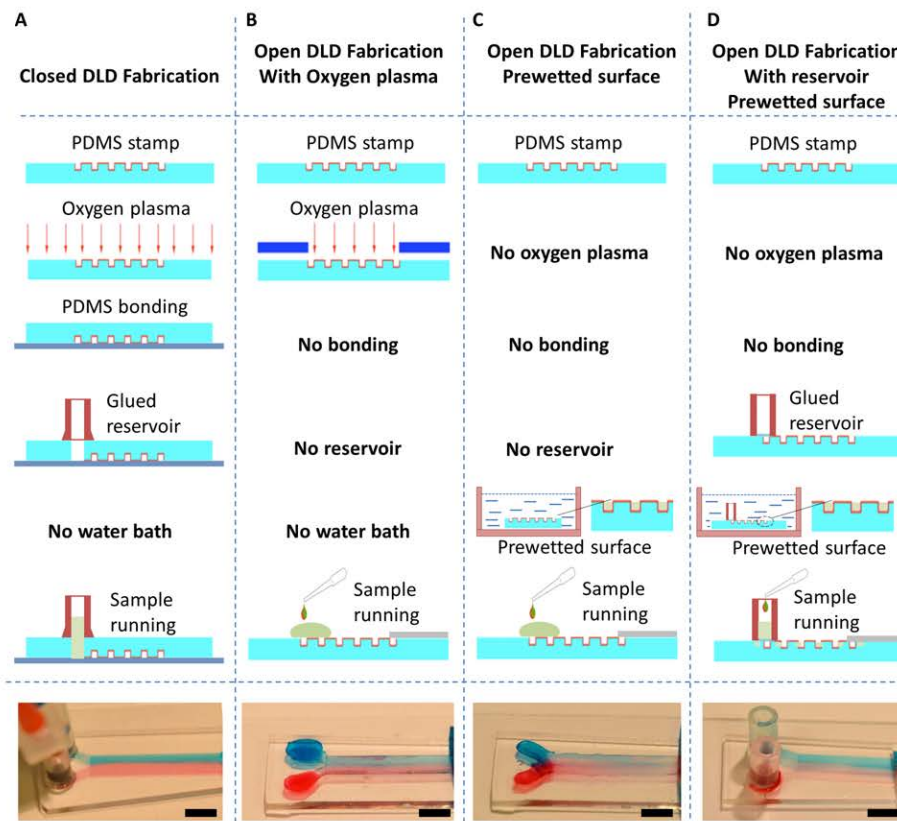


Figure S2. Comparison of different fabrication methods for closed and open DLD devices. (A) Conventional closed device fabrication. (B) Open device where the sorting structures are selectively treated with oxygen plasma to make them hydrophilic. (C) Rendering the PDMS hydrophilic by immersion (prewetting) in a water bath (plain water at room temperature in 5 minutes) instead of in an oxygen plasma. (D) Addition of a reservoir gives better control of the sample and allows for larger volumes. Scale bars 5 mm.

The wetting of the devices using the different surface treatment strategies was characterized in more detail as presented in Figure S3. Selective oxygen plasma treatment gives a strongly hydrophilic surface with contact angle $\sim 0^\circ$. Immersing the device in aqueous buffer gives a less hydrophilic surface (contact angle $\sim 60^\circ$ outside the device and an effective contact angle $\sim 0^\circ$ in the DLD array). The latter approach is fully adequate for the operation of the device and much simpler as it does not require any oxygen plasma equipment.

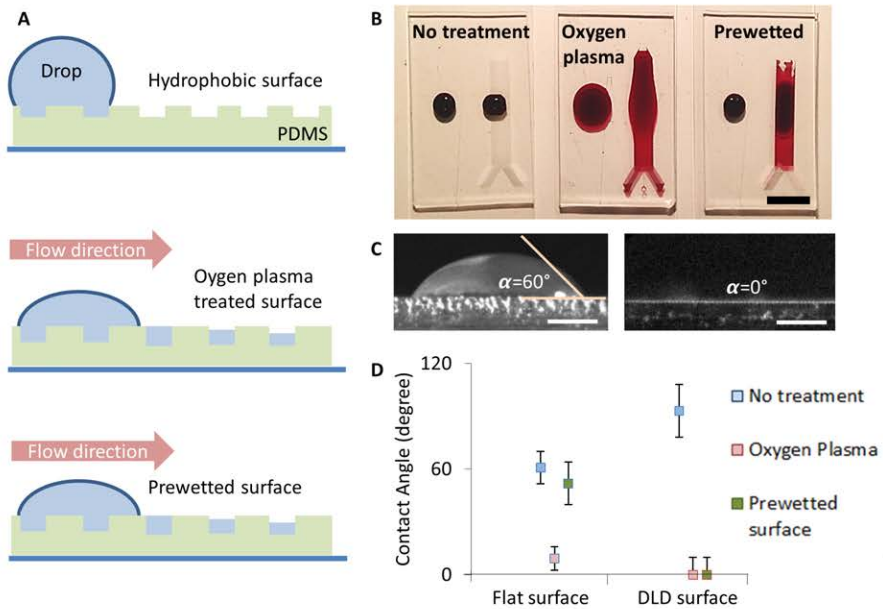


Figure S3. Hydrophobic and hydrophilic devices. (A) Schematic of a water droplet on an untreated (hydrophobic) surface and the two treated hydrophilic surfaces (B) Visualization of the wetting behavior of the three kinds of surface treatments on flat and patterned PDMS using an aqueous solution of red food coloring. (C) Cross-sectional view of water drop outside and on the DLD array for a prewetted surface. (D) Comparison of wetting angles on flat and patterned surfaces after no treatment, oxygen plasma and prewetting. The error bars represent the standard deviation of the measurement.

Volume of a filled device

The volume of the liquid in a filled device is calculated based on the table in figure S1C. The ratio of the area of the fluid and the total area of the unit cell is 0.58, which is multiplied with the overall dimensions of the device (length 20 mm, width 4 mm and depth 24 μm), giving us the total volume of device 1 of 1.1 μL .

Uniformity of wetting

The characteristics and uniformity of the wetted array are characterized by confocal microscopy and direct imaging with a macro objective. In both cases device 3 was used with added reservoirs. For the confocal images fluorescein isothiocyanate (FITC) was first dissolved in methanol to 10% that was in turn diluted in water 100 times and the methanol

allowed to evaporate. The confocal microscope is based on a Yokogawa CSU22 spinning disc, Andor laser combiner and Andor iXon DU-897 CCD camera on an inverted Nikon Ti microscope. A Plan 50x ELWD Dry and a Plan Fluor ELWD 40x Ph2 ADL objective with NA 0.32 and 0.4 respectively were used for figures 2C-F. Since the microscope is inverted, the device was turned upside-down for imaging (surface tension dominates and so this has little to no effect on the shape of the liquid surface). The image contrast was adjusted such that scattered light was rejected from the image.

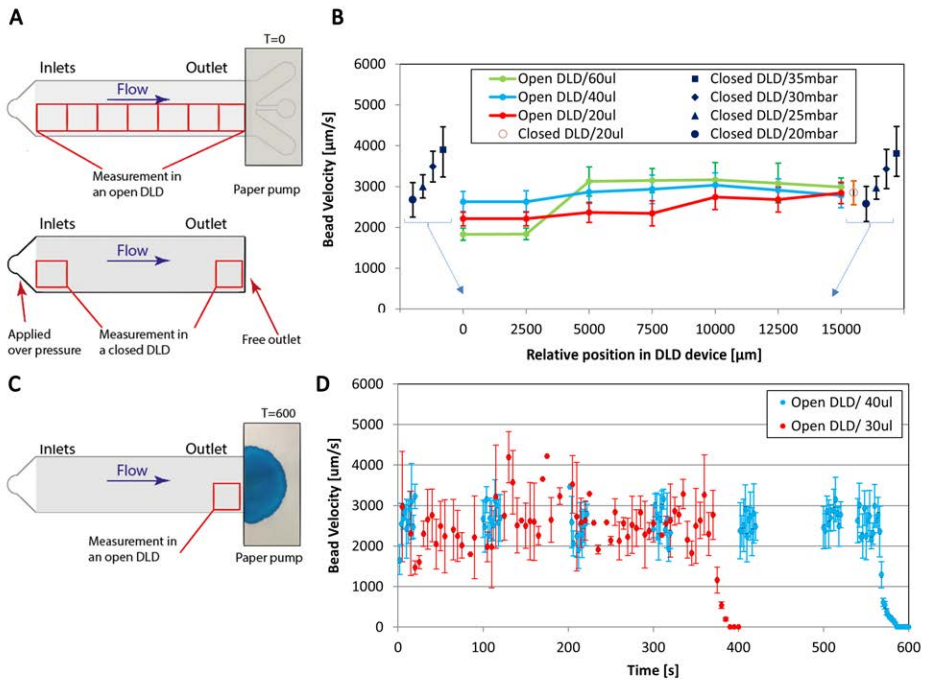


Figure S4. Particle velocity measurements for open and closed DLD devices. The flow in the open devices is driven by a paper capillary pump without any wax-defined channels. The paper is shown at $t=0$ s in (A) and $t=600$ s in (C). The flow in the closed devices is driven by over pressure as well as by a paper capillary pump. The different sets of experiments took place using the same design of DLD (Device 1 (Figure S1)). The following microspheres were used at a dilution of 50x in deionized water: green fluorescent polystyrene beads with diameter $1.57 \mu\text{m}$ (CV 2%) and functionalized with carboxylate groups from Polysciences Inc. (Warrington, PA). (A) Schematic of measurement setup for velocity measurements at different locations for open and closed devices. (B) Velocity of the beads as a function of position for open and closed devices. For the data where a paper capillary pump was used the volume in the reservoir is indicated. For the pressure driven flow the applied pressure difference is given. (C) Schematic of measurement setup for velocity measurements as a function of time. (D) Velocity of beads as a function of time when $30 \mu\text{L}$ (red) and $40 \mu\text{L}$ (blue) of sample is added to the reservoir. The error bars represent the standard deviations of the measurements.

For the images with the macro objective, the device is wetted with an aqueous food dye and imaged, with the liquid facing upwards, using a macro objective (Canon MP-E 65 mm f/2.8 1-5x) with a Canon 5D Mark II camera house. Basic contrast and brightness adjustments were made to ensure that the image reflects what is seen by the naked eye.

We could observe a tendency that the flow velocity (see below) is slightly lower for the first ~5 mm along the device. This indicates that the flow cross section is larger here, which is consistent with the flow extending above the posts since the volume flow rate is a conserved quantity. We observed that this effect vanishes as the fluid level drops, away from the reservoir and also decreases as the sample volume in the reservoir decreases with time.

Flow measurements

We measured the flow rates at different positions along open and closed devices using an applied overpressure or using a paper capillary pump (Figure S4). Velocities of fluorescent microspheres were observed between two neighboring posts in the same row.

The volumetric flow rates were measured directly by running the device with reservoirs filled with well-defined volumes and recording the elapsed time until the reservoirs were empty (Figure S4D). The volumes were corrected by subtracting the evaporated volume from the device based on figure S5 (8.5 nL/s). The time was measured until the velocity was half of the mean velocity. The remaining liquid in the device was crudely estimated to half the volume of the device, i.e. $0.5 \times 1.1 \mu\text{L}$. This volume was subtracted from the total volume considered. From these two measurements we obtain approximate values of 70 nL/s and 61 nL/s for the two different volumes tested. These results are consistent with the results of combining the velocity measurements (Figure S4B) with the total flow cross section based on the designed dimensions (Device 1 in Figure S1C) of the device giving flow rates of 71 ± 19 nL/s. The correspondence of the two types of measurements indicate that the flow is indeed taking place such that it fills up the space between the posts without overflowing.

Equivalent pressures applied to the device

The equivalent pressure exerted by the paper capillary pump is found to be 21 mBar by comparing the applied over-pressure necessary across a closed device to achieve the same flow velocities as for a closed device with a paper capillary pump (Figure S4B). The pressure exerted by the paper capillary pump exceeds the pressure due to the water pillar in the reservoir. The pressure generated in the reservoir depends on the height difference between the inlet and outlet ($\rho g \Delta h \sim 1$ mBar/cm with $\rho = 1000$ kg/m³ density of water, $g = 9.8$ m/s² gravitational acceleration, Δh height of water pillar). The tested volumes, 30 μL , 40 μL and 60 μL , correspond to heights of 4.2 mm, 5.6 mm and 8.4 mm of sample respectively in the reservoir (inner diameter 3mm) giving hydrostatic pressures of 0.4 mBar, 0.6 mBar and 0.8 mBar which is much less than the involved estimated negative pressures exerted by the capillary paper pump pulling the sample. The capillary pumping effect of the paper therefore dominates the flow and the fluid is predominantly pulled through the device.

Flow resistance

Flow resistance for the closed devices is estimated based on the relationship

$$Q_{pump}^{closed} = \frac{\Delta P_{pump}}{R_{load}^{closed}}$$

where R is the fluidic resistance, Q is the volumetric flow rate and ΔP is the applied pressure difference across the device. From figure S4B we obtain $R^{closed} = 30 \cdot 10^{12} \text{ kgs}^{-1}\text{m}^{-4}$.

The flow resistance of the open device is expected to be slightly lower than that for the closed device. It is calculated below based on figure S5.

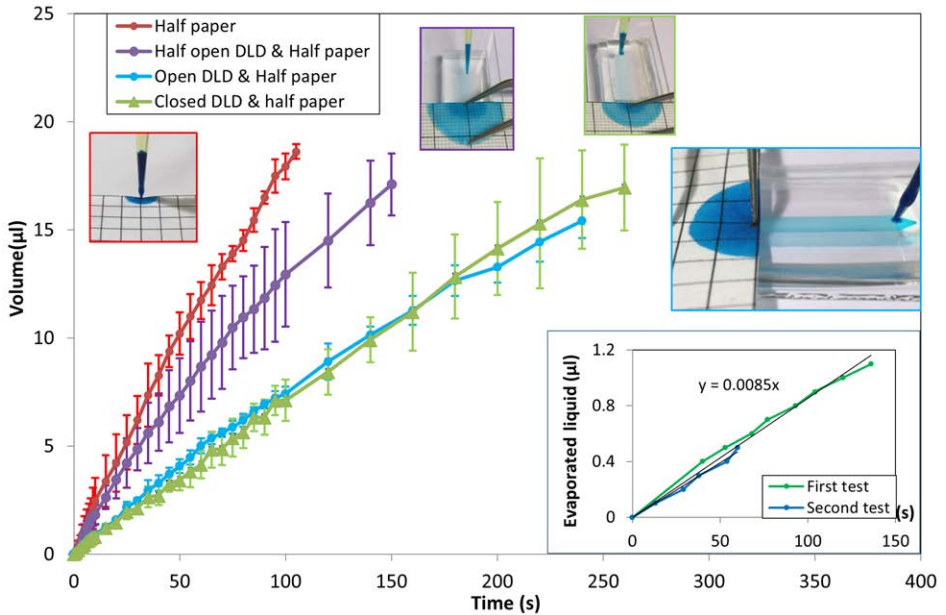


Figure S5. Liquid flows versus time corrected for evaporation. The liquid is 0.5% food coloring diluted in deionized water. The graph shows four cases. From the left to the right we have: liquid added at the edge of a paper (half paper), open DLD device of length 10 mm (half device) connected to paper, open DLD of length 20 mm (whole device) connected to paper, closed DLD of length 20 mm (whole device) connected to paper. To be able to easily judge the extent of the drops on the paper, a grid pattern is printed on the paper using a standard laser writer. The inset shows the accumulated evaporated liquid from a filled device (device 1). From this graph we can conclude that the evaporation rate from the device is 8.5 nL per second.

Characterization of the paper capillary pump

The paper capillary pump can be treated as a battery with an internal resistance and an internal negative pressure or, in analogy to electronics, a hydromotive force. To estimate the internal resistance and the hydromotive force the following system of equations (number 1 to 4) are considered. Note that we will obtain an estimate of the flow resistance of the open device from these calculations.

$$\left\{ \begin{array}{l} Q_{paper} = \frac{\Delta P_{internal}}{R_{internal}} \\ Q_{paper}^{openHALF} = \frac{\Delta P_{internal}}{\frac{1}{2}R_{load}^{open} + R_{internal}} \\ Q_{paper}^{open} = \frac{\Delta P_{internal}}{R_{load}^{open} + R_{internal}} \\ Q_{paper}^{closed} = \frac{\Delta P_{internal}}{R_{load}^{closed} + R_{internal}} \end{array} \right.$$

We first calculate the internal resistance of the paper by combining equations 1 and 4 above to eliminate the internal pressure (hydromotive force).

$$R_{internal} = \frac{\Delta P_{pump}}{Q_{pump}^{closed}} \frac{Q_{paper}^{closed}}{Q_{paper}^{closed} - Q_{paper}^{closed}}$$

Numerical data is extracted from Figures S4 (for the pump driven flow) and S5 (for the paper capillary pump driven flow) based on the initial flow rates for each case and combined with the flow resistance of the closed device as calculated above.

$$\begin{aligned} \Delta P_{pump} &= 21 \text{ mBar} \\ Q_{pump}^{closed} &= 71 \text{ nLs}^{-1} \\ Q_{paper} &= 198 \text{ nLs}^{-1} \\ Q_{paper}^{closed} &= 71 \text{ nLs}^{-1} \\ \Rightarrow R_{internal} &= 16.5 \cdot 10^{12} \text{ kg s}^{-1} \text{ m}^{-4} \end{aligned}$$

The hydromotive force is now calculated by using the number of the flow rate of the paper without any device ("Half paper") in fig S5 combined with equation 1 above.

$$\begin{aligned} Q_{paper} &= 198 \text{ nLs}^{-1} \\ \Rightarrow \Delta P_{internal} &= 32 \text{ mBar} \end{aligned}$$

Plugging the results above into equation 3 above, the flow resistance of the open device.

$$\begin{aligned} Q_{paper}^{open} &= 80 \text{ nLs}^{-1} \\ \Rightarrow R_{load}^{open} &= 23.1 \cdot 10^{12} \text{ kg s}^{-1} \text{ m}^{-4} \end{aligned}$$

Finally, as a simple control the flow rate of the device cut in half is estimated based on equation 2 above.

$$Q_{paper}^{openHALF*} = 113nLs^{-1}$$

The value is lower but still consistent with the value obtained by measuring the initial slope of the corresponding curve in figure S5.

$$Q_{paper}^{openHALF} = 157nLs^{-1}$$

Evaporation

To obtain rough estimates of the evaporation rates we measured the evaporation rates for different cases by using a precision balance (Ohaus Corp. Pine Brook, NJ USA, model Pioneer PA114C, minimal readout 1 µg).

An evaporation of 8 nL/s from the device can be compared to the typical flow rate through the device of 65 nL/s. Roughly 12% of the sample is thus evaporated from the device.

Due to nonuniform wetting and possible variations in the lab environment during the course of the experiments, the evaporation rates should be considered rough estimates to give a perspective of the relationship between the evaporation rate and the volumetric throughput in the devices.

The lab environment had a 60±5% RH and room temperature of 21°±1° C.

Biological samples

The size distributions of the biological samples used were determined by measurement in optical micrographs using ImageJ (Figure S6). The results are summarized in the following table.

<i>Sample type</i>	<i>Dimensions ± std dev</i>	<i>Shape</i>
MCF7 (cancer cell line)	17.3±2.1 µm	spherical
White blood cell	12.2±0.9 µm	spherical
Red blood cell	2.2±0.5 µm 7.8±0.6 µm	biconcave
<i>Trypanosome cyclops</i>	2.5±0.5 µm 12.8±3.3 µm	ribbon-like

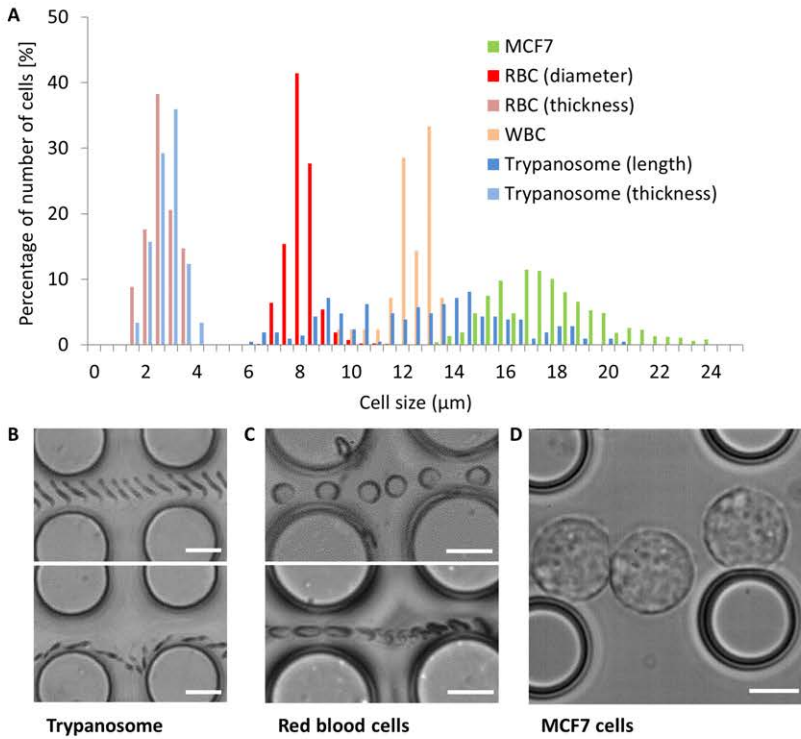


Figure S6. Size distribution of biological samples based on measurements in optical micrographs. (A) Histograms of size distributions. For the spherical cells (MCF7 and WBC) one number gives the relevant size (diameter). Red blood cells and the parasites are described by two numbers (thickness and overall diameter or length). (B) & (C) Optical micrographs of the non-spherical cells exhibiting different orientations depending on device depth ($9\ \mu\text{m}$ and $24\ \mu\text{m}$) (top images shallow device and bottom images deep device) (D) Optical micrograph of spherical MCF7 cells. All scale bars $10\ \mu\text{m}$.

Paper II



Softness sorting for cancer cells in deterministic lateral displacement.

Trung S.H. Tran^a, Jason P. Beech^a, Bo Baldetorp^b and Jonas O. Tegenfeldt^a

(a) Division of Solid State Physics & NanoLund, Lund University

(b) Department of Oncology, Lund University

Abstract

Due to their direct association with the physiology of cancer cells, physical properties are especially attractive as markers for sorting and characterization. Where molecular surface markers are lacking, the physical properties can instead serve as inherent markers for separation. Indications that soft cancer cells are more metastatic than hard cells make mechanical properties of specific interest. Our work provides a deeper understanding of deformability-based sorting using deterministic lateral displacement (DLD) and we show how DLD devices can be used for the characterization and fractionation of cell samples into subpopulations with different mechanical properties. Our aim is to develop a device to help oncologists gain more accurate prognoses and better monitoring of the effects of treatment.

Key words: deterministic lateral displacement, cell deformability, softness sorting.

Introduction

During the last decade, deterministic lateral displacement has been developed and applied to an increasing variety of biological samples. Since the initial work showing high resolution separation of plastic microspheres and potential for applications in DNA separation (1), significant advances in the method have been reported. New DLD devices designed to separate a range of samples, all with specific challenges, together with the theories used to describe how devices function have been developed. DLD applications include *e.g.* the fractionation of blood components (2-5), isolation of cancer cells from blood cells (6-8), parasite separation (9, 10) and the isolation of extracellular vesicles (11-13).

Essentially, DLD is a size-based sorting technique. With carefully designed obstacle arrays, DLD has been shown to be a powerful sorting technique with high resolution (12) and throughput (14). In 2011, Holm *et al* first reported the use of the method as a morphology-based sorting tool when they extracted parasites from blood (9) and in 2012, Beech *et al* further extended the method to deformability-based sorting of red blood cells (15) followed by Henry *et al.* (2016) with careful simulation (16). These capabilities make DLD a very interesting tool for label free cell sorting and analysis.

In a DLD device (Fig. 1C), an array of posts is designed with different parameters: gap size, post size and post shape as well as critical radius, R_c , which is pre-calculated depending on the intended target particles. For hard spheres, those smaller than a critical size move along the flow, while those larger than the critical size switch to neighboring streamlines and become displaced (see SI). In biological applications, samples are often soft and deformable. Fluid shear and interactions with device structures (dependent on flow rate) change the shape and the effective size of particles and therefore their trajectories as shown in Figure 1A. The net effect is that the outlet displacement distribution depends on pressure for soft particles (Fig. 1B).

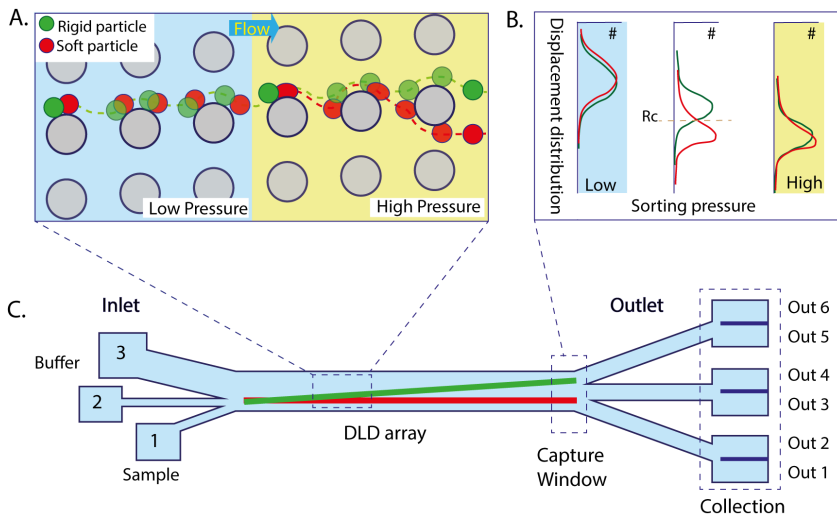


Figure 1. Schematic overview of deformability-based separation in a DLD device. (A) A cartoon depiction of a DLD device in which a mixture of particles (rigid green and soft red particles) and buffer are loaded in the inlet. At the low pressure, particle trajectories of both particles are completely overlapped, a separation of continuously displaced (green) and non-displaced (red) particles illustrate the deformability based operation of DLD. (B) The lateral displacement distribution of particles at low and high pressure shows that they cannot be separated but at an optimized transition pressure (also dependent on R_c), sorting can be achieved. (C) The typical device, which is used in this work, has 3 inlets and total 6 outlet reservoirs to collect the sorted fractions.

By carefully evaluating the correlation between outlet distributions, the deformed radii of cells and flow rate, we can characterize the deformability of cells. Based on the knowledge gained, devices can be optimized and re-designed to achieve the deformability-based separation of specific cell types.

The cells we target in this work are MCF7 (human breast cancer cell line), MCF10A (human breast cell line) and MDA-MB-231 (human metastatic breast cancer cell line). These are quite common models for cancer research with known physical properties and specific receptors (table 1) for identification or separation (17). However, without the use of specific probes, they are a challenge for label-free sorting due to the similarity of many physical properties including density, shape, size and electrical properties. In this study, the deformability-based sorting of MCF-7, MCF-10A and MDA-MB-231 provides a novel approach for cell sorting and separation in the absence of specific molecular probes.

Results and discussion

Cell physical properties and current sorting challenges

Cell density, adhesion (specific through e.g. immunolabeling and non-specific attachment) and size are the physical parameters commonly used in cell sorting techniques, for instance centrifugation, adherence and filtration. Centrifugation has seen large-scale use, but it has low specificity and is limited to separate cells by the density of cytoplasm and nucleus (18). What is more, the majority of soft-tissue derived cells are adherent and present a spherical shape in suspension, and hence cannot be distinguished without labelling. Also, the high aggregation rates of these cells make them clog easily in cell strainers or membrane filters. A small difference of dielectric properties (19, 20), and an overlap of size distribution also renders them inseparable by dielectrophoresis or size-based sorting techniques (table 1).

Table 1. Physical properties of human breast cell lines

Parameter/ Unit	MDA-MB 231	MCF-7	MCF-10A	Reference
Antibody binding				
- Estrogen receptor	No	Yes	No	(17)
- Progesterone receptor	No	Yes	No	(17)
- Androgen receptor	Yes	Yes	No	(17)
Physical properties				
- Attachment ability	Yes	Yes	Yes	ATCC
- Density of cytoplasm & nucleus [g/cm^3]	1.05 1.3	1.05 1.3	1.05 1.3	(18)
- Aggregation rate [%]	>30	~ 27	~ 19	Measurement
- Circularity of cells	0.81 ± 0.15	0.76 ± 0.12	0.78 ± 0.11	Measurement
- Diameter of cells [μm]	15.1 ± 7	17.9 ± 7	15.6 ± 6	Measurement
- Young's modulus [Pa]	183-363	415-855	667-1641	(21, 22)
- Dielectric constant [ϵ']	~16	~17	~3	(20)
- Conductivity of cells [S/m]	~5.7	~7.6	~0.3	(20)

Among the physical properties of the cells, elasticity (cytoplasm and nucleus), i.e. the Young's modulus of cancerous and non-cancerous cells shows significant differences and could provide a basis to identify and sort them by deformability-based sorting. Atomic force microscopy has been used to characterize cell elasticity as shown in Table 1 (21, 22). In microfluidics, the deformability differences of these cells have been observed, measured and confirmed by several methods, including cell squeezing (23), compressive chamber (24) and optical stretcher (25).

Although cell elasticity has been reported and proposed as a promising marker for cancer research for several years, deformability-based applications have not been fully investigated, especially cell sorting techniques. Primary challenges have been the small difference in Young's moduli together with the wide distribution in sizes within most cell populations. A method that is able to detect differences in size and deformability with high sensitivity and that can separate based on these parameters would have considerable impact. The methods also need to be robust, able to deal with common issues such as cell aggregation and need to preserve cell viability. In this study, we demonstrate that DLD is a promising deformability-based sorting technique with high sensitivity and resolution. The deformation of individual cells has been investigated as a function of applied pressure and conditions for separation have been optimized giving separations with satisfactory cell viability.

Synthetic microsphere controls

Polystyrene beads of known sizes are commonly used to calibrate DLD devices by counting the displacement distribution at the outlet. Due to the high Young's modulus (Young's modulus of $3-3.6 \times 10^9$ Pa), polystyrene beads are good models for hard particles. Polyacrylamide particles are softer (Young's modulus of $2.8-6.7 \times 10^2$ Pa) and serve as a good reference for a softer sample (26). These hard and soft reference particles were run in the device at different pressures. While the outlet position of the hard beads remains unchanged with increasing operational pressures, the softer particles displace less and at 700 mbar hard and soft particles are separated (see SI).

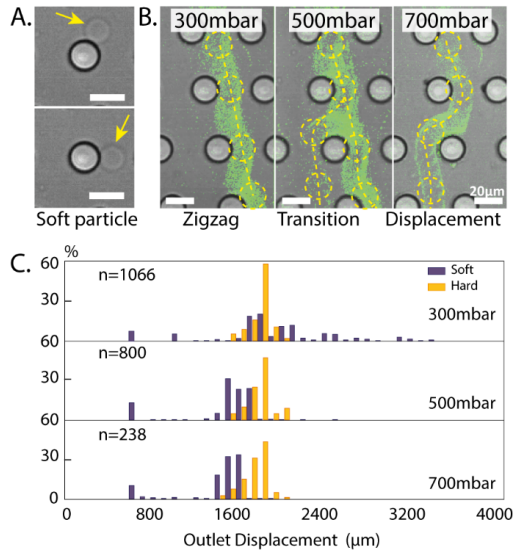


Figure 2. Hard and soft particles (polystyrene and polyacrylamide) both with diameters $15\mu\text{m}$ in a DLD array ($D_c=14\mu\text{m}$). (A.) Consecutive images of a soft and transparent particle interacting with a post. (B.) Time averages of many particle traces of the same kind of particle (polyacrylamide) as that shown in A. A transition from displacement mode to zigzag mode occurs as the pressure is increased. (C.) Hard and soft particles distributions at the end of the separation array. Soft particles become effectively smaller (less displaced) as the pressure is increased.

Direct cell deformation measurement

In the literature, cellular deformation has been related to interaction of the cells with the surrounding environment. Further, cellular deformation also strongly depends on the biomechanical properties of a typical cell or cell type, and its cytoskeleton. A comparison of the relative amount of F-actin and tubulin among MCF7 and MCF10A has been conducted by Kim *et al.* (24). In their conclusion, the cancerous cells (MCF7) showed lower amounts of F-actin and tubulin than a normal cell (MCF10A).

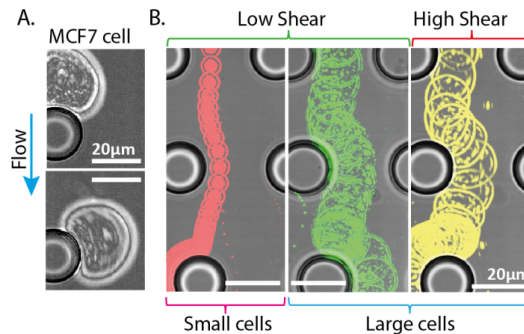


Figure 3. Cell trajectories due to different size and deformation effects. (A.) A single MCF7 cell is deformed when interacting with a post (B.) At low shear, cells follow the expected paths (small ones are in zigzag mode while large ones are displaced). When increasing the shear rate, large cells start deforming and the effective size is decreased such that the trajectory is significantly affected.

Based on our preliminary results of hard and soft particles we expect the softer cancer cells to deform more readily at higher flow rates in our DLD devices. Using a high-speed camera with high frame rates ($\sim 10000\text{fps}$), we are able to capture and analyze the behavior of individual cells as they flow through

the devices. Fig. 3A shows how a single MCF7 cell deforms when interacting with a post. Furthermore, the trajectories of small and large cells illustrate the sorting mechanism of the DLD array at low shear stress. A significant change in trajectories is observed when the large cells are subjected to higher shear rates (Fig. 3B). The figure gives a clear evidence that soft large cells could behave as a small cell in a DLD array at a high shear rate (high flow rate). In a contrast, normal cells behaved similarly to stiffer particles, and were less affected by the shear rate. Depending on the deformability of these cells, we separate them in the DLD device.

By carefully visualizing the trajectories of individual cells, we obtain a better view of their behaviors and relevant parameters. Prior to contacting the post, single cells retain their morphology while following the streamline in the laminar flow. Upon contact with the post, due to the shear gradient, the cell starts rotating on the post's surface (see SI). At this time, the pressure gradient surrounding the post compress the cell membrane and create a deformation between the cell and the post surface. The deformation reaches a maximum value at a certain point of contact with the post (the maximum pressure gradient as show in SI). After this point, the shape recovery occurs before the cell leaves the post. To be able to evaluate the deformation of individual cells, the image's features are extracted and analyzed.

Due to significant differences in image quality at low and high flow rates, we developed two separate strategies to be able extract all needed information. Firstly, at low flow rate, the contrast of the image is high, so cell boundaries can be precisely detected. Cell area, perimeter, contacting angle and the minimum diameter are quickly extracted using a boundary detection function (Fig.4A). At high flow rates imaging must be performed at high frames rates and with short exposure times which leads to reduced contrast in the images and the boundary detection becomes unreliable. Hence, a projected image of an individual cell and a post (from stage I to stage III) is used to analyze instead of analyzing single frame in the previous approach (Fig.4C), and the contacting angle and cell diameter are measured. Figure 4B illustrates the correlation between contacting angle and cell diameter of a single MCF7 cell.

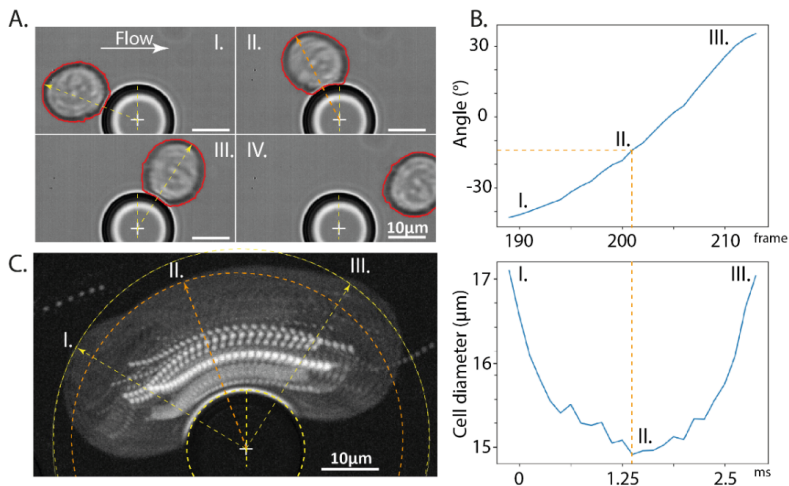


Figure 4. Cell detection and analysis by image processing. A) Cell boundary is auto-detected and provides all features of the cell such as cell area, perimeter, rotation, speed as well as deformation. C) To calculate a measure for the deformation, we refer to the relevant size scale of the cell as its diameter, defined as the distance from the circumference of the circular post (the innermost yellow dashed circle) to the outer periphery of the cell. The minimum diameter corresponds to the large orange circle and the initial to the large yellow dashed circle. B) The contacting angle as a function of the frame number of a video (top). Cell diameter versus time (bottom). The deformation process of the cell is clearly observed over time.

The combination of these two methods allows us to compare single cells results over a wide range of flow rates. The two parameters used to calculate deformation are the initial and minimum diameter (during deformation).

$$Deformation = 1 - \frac{D_{minimum}}{D_{initial}} \quad (1)$$

To investigate the change in diameter which is due to the applied pressure, the initial diameter and minimum diameter of MCF7 are first obtained in figure 4A. The dependence between minimum diameter and pressure is clearly recorded. It is evident that higher pressure (or higher shear rate) is associated with a decreased diameter for all cells. We conducted the same experiment with other cell types (MCF10A and MDA-MB231), and observed as expected that the cells experience the highest deformation at the maximum pressure applied in our study (due to the limits of equipment), 900mbar. To easily compare the difference among these cells, we show the data of the initial diameter and deformation value which are all collected at 900mbar (Fig.5C).

From their deformation values at maximum pressure (900mbar), normal cells (MCF10A) seem stiffer than other cells while the invasive cells (MDA-MB-231) show highest response to the shear rate and appear as the softest cells. The deformation value of each cell type is redrawn in the box-plot of figure 5D. To summarize, cell deformation is successfully extracted and is significantly different among the cell lines that we considered.

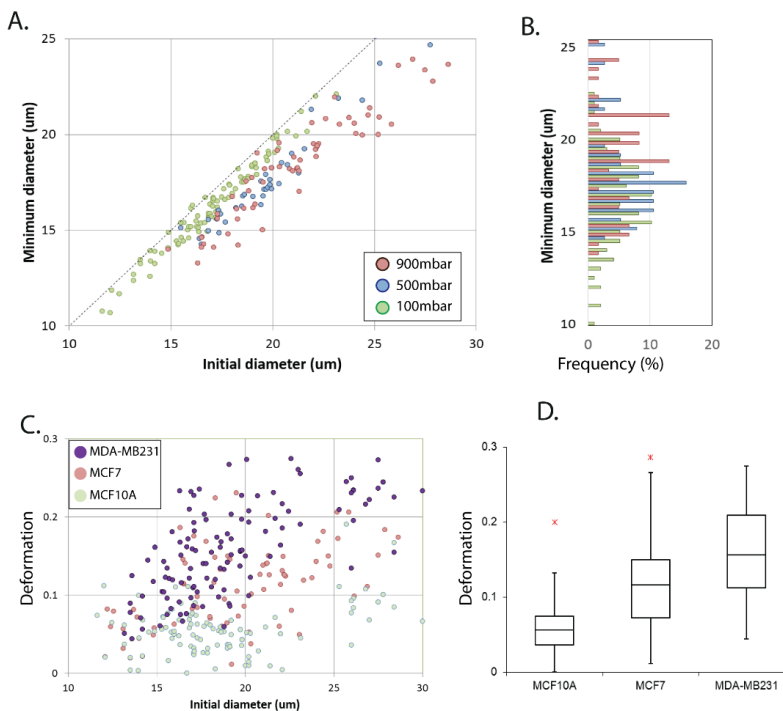


Figure 5. Data of direct deformation measurements. A & B) Data of MCF7 cells in a range of 100-900mbar in scatter and column plot. C) A comparison among three cell types (MCF7 cells (green), MCF10A cell (red) and MDA-MB231 cells (purple)) at 900mbar in scatter plot and D) Box-plot with the outliers.

Indirect cell deformation measurement

Although the direct measurement method provides a reliable value of the cell deformation, the limits of single cell measurements and the time consumption (data transfer from internal memory of camera to computer memory and image processing of the whole process of single cell interaction) make it impractical for routine use. An alternative is needed which performs fast measurement of large amounts of cells (at least thousands of cells). To achieve this goal, a wider view of the full width of the channel is placed at the end of the array. In this area, cells are divided by size into subpopulation due to the DLD sorting mechanism. The lateral position of each cell shows its effective size, as determined by the expected position of non-deformable particles based on the known parameters of the device. At the end of array, no interaction is expected in the straight array, so the apparent size shows non-deformable size, which is useful for size comparison in the deformation equation. Thus the deformation can be represented as below

$$Deformation = 1 - \frac{D_{effective}}{D_{apparent}} \quad (2)$$

In here, the initial diameter and minimum diameter are represented by apparent size and effective size in an indirect approach for cell deformation measurement.

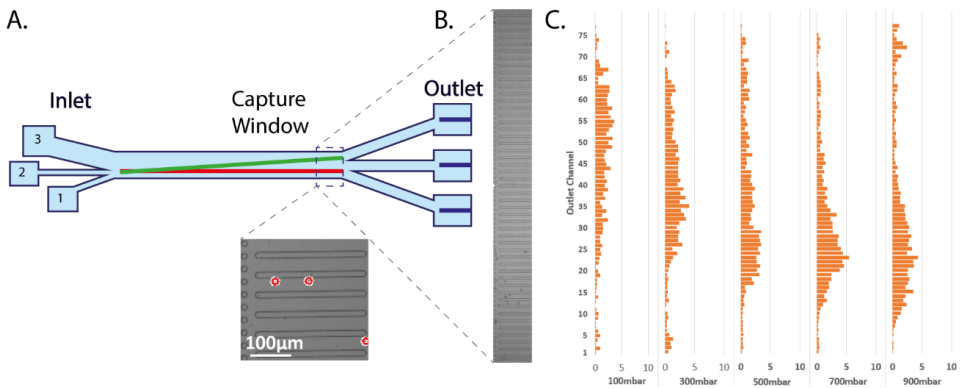


Figure 6. Cell distribution at the end of DLD array. A) The capture window position in the whole device. B) Actual view of the channels. C) The number of MCF7 cell is counted for several applied pressures (100, 300, 500, 700 and 900mbar).

Figure 6 shows the capturing area of cell distributions, and the distribution of MCF7 cells in a range of applied pressures (100, 300, 500, 700 and 900 mbar). The graph illustrates a shift in cell distribution in relation to higher applied pressure. As all cells have the relaxed size larger than critical size of the device, they all displace at the low pressure (100 mbar). At low pressure, the effective size could represent to the apparent size of cells. When the pressure increases, deformation decreases the effective size and the cells appear smaller (Fig.6C). To confirm that cell size distribution is not affected when cells pass through the array, the size distribution of the sample was checked before and after each experiment (see SI).

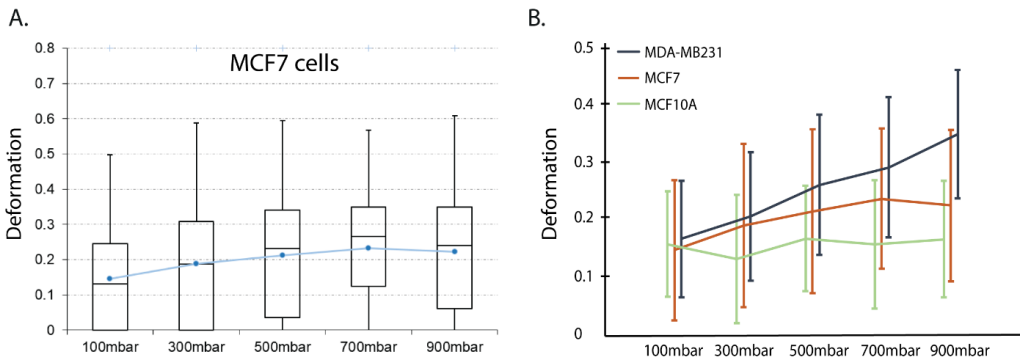


Figure 7. Cell deformation by observing the cell distribution at the end of the DLD array. A) Deformation rate of MCF7 cell at the end of the array. A box-plot shows the deformation distribution as a function of pressure. B) A comparison among three cell types.

To extract the cell deformation value from its distribution (Fig.6C), the apparent size is measured using an image analysis tool developed for the purpose. A box-plot graph of MCF7 deformation is shown in Fig.7A, and a simpler line plot among three types of cells is shown in Fig. 7B. The differences in their deformation are initially quite small but increases with increasing pressures. Due to limits of our experimental setup, we could apply a maximum of 900 mbar pressure while capturing the particle movement at high flow rate. The tendency and the deformation level among cell lines are acceptable compared to the direct measurement method.

Instead of extracting a series of cell sizes (from the initial diameter to minimum diameter) for each single cell, the measurement of one apparent size per cell speeds up the analysis process and thus data can be acquired for thousands of cells (for each pressure) (Fig.7). A fast measurement has successfully been accomplished, but for a real-time analysis, an optimization step of data transfer is suggested for the future work.

Deformability-based separation

Since the second aim of this study is cell isolation based on deformability, different cell types have been run through the DLD system at a variety of applied pressures and the resulting displacement distributions and cell deformations have been presented above. In order to further conduct the sorting experiment, a mixture of cells is required. To distinguish the cells, we fluorescently stain the cells and count them at the end of the device. An illustration of the sorting capability was conducted for a mixture of MCF7 and MDA-MB-231 cells. Figure 8A presents a practical setting to run and collect the fraction in different reservoirs. In this work, MCF7 and MDA-MB231 cells are loaded into the DLD device and a range of applied pressure (from 100mbar to 900mbar) is applied. After each pressure, all cells are collected in the reservoirs and counted by fluorescence microscopy (Fig.8B).

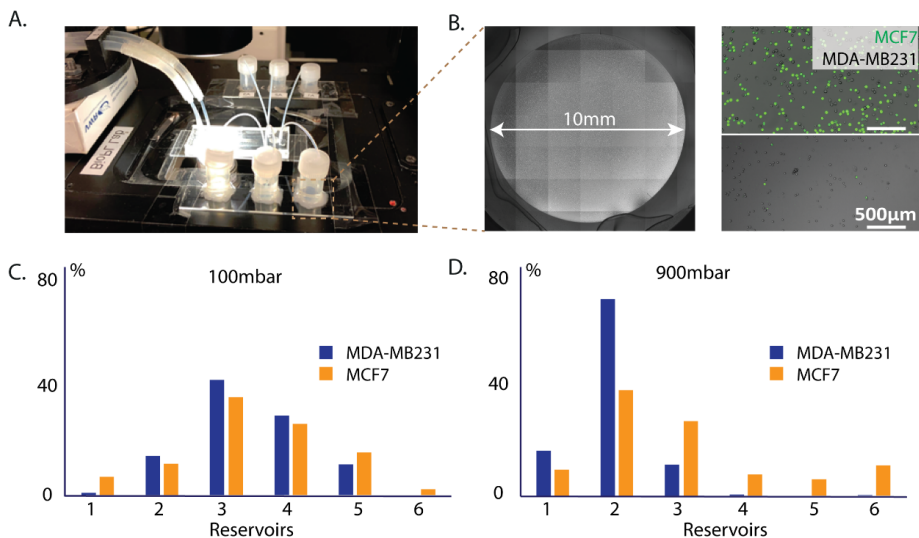


Figure 8 Cell measurement at the outlet reservoirs. *A)* A typical setup for cell fractionation. *B)* In the reservoirs, all cells settle down onto the glass substrate. The MCF7 cells express GFP and are fluorescently detected. The MDA-MB231 cells are visible in standard bright field. *C)* Relative fractions of MCF7 and MDA-MB231 cells in 6 outlet reservoirs at a low pressure (100mbar). *D)* Results for high pressure (900mbar).

It is clearly observed that no significant differences in trajectories of the cells occurred at low applied pressures (100mbar). The similarity of size and shape is clearly a practical challenge for those cells. However, separation was obtained when the pressure increased. At 900mbar, the number of cells in each tube showed a significant difference between the cell ratios compared to the initial mixture (50:50). In terms of purity, we start with 50% purity of the MDA-MB231 cells. In the tube 2, the purity increases to 71% with a capture rate of approximately 75% of total MDA-MB231. In the tube 3, the purity of MCF7 was 68% and 35% of total MCF7 cell is collected.

Although the performed separation does not demonstrate high purity, the results clearly demonstrate the effect of cell deformation on the sorting process. Further optimization of device design and flow rates is necessary for improved performance.

Materials and Methods

Device fabrication

In a contact mask aligner (Karl Suss MJB3 and MJB4, Munich, Germany), negative photoresist SU8 (MicroChem, Newton, MA, USA) spun on a 3" silicon wafer was exposed to UV light through a chrome-mask designed in L-Edit 11.02 (Tanner Research, Monrovia, CA USA) and printed by Delta Mask (Delta Mask, Enschede, The Netherlands). Before casting of PDMS, a monolayer of 1H,1H,2H,2H-perfluorooctyltrichlorosilane (ABCRC GmbH & Co. KG, Karlsruhe, Germany) was applied to the master as an anti-adhesion agent to facilitate demolding. A 10:1 mixture (monomer: curing agent) of PDMS (Sylgard 184, Dow Corning, Midland, MI, USA) was degassed, poured onto the master then baked for 2 hours at 80°C.

To bond the device to glass, the PDMS device and the glass were treated with oxygen plasma (Plasmatic Systems, Inc, North Brunswick, NJ, USA). Subsequently, holes were punched at the inlets and outlets and silicon reservoirs were glued.

Sample preparation

Fluorescently labeled polystyrene microspheres with a diameter of 15 μm from Polyscience Inc. were suspended in milliQ water and used at varying flow rates for calibration. Soft polyacrylamide particles (diameter $15 \pm 0.84\mu\text{m}$, Young's modules $670 \pm 280\text{ Pa}$) obtained from Prof. Guck's lab (TU Dresden, Germany) were used as particle reference in softness sorting in DLD (26).

MCF-7, MDA-MB231 (two breast carcinoma cell lines) and MCF-10A (human breast epithelial cell line) were obtained from the American Type Culture Collection (ATCC) and were cultured at 37°C and 5% CO₂. Cell culture medium for MCF-7 was DMEM, 10%FBS and 1% Penicillin-Streptomycin (Sigma-Aldrich). Cell culture medium for MCF-10A was DMEM, 5% Horse Serum, 20ng/ml Epidermal Growth Factor (EGF), 10ug/mL Insulin, 0.5ug/mL Hydrocortisone, 100ng/mL Cholera Toxin and 1% Penicillin-Streptomycin (Sigma-Aldrich). Cell culture medium for MDA-MB-231 was DMEM (1.25% L-glutamine), 1% Penicillin-Streptomycin (Sigma-Aldrich), 10% FBS. After a one-week subculture, the cells proliferated to fill more than 80% of the surface of the culture flasks and were considered ready for separation experiments.

Image acquisition and analysis

Particle and cell distributions were calculated from images acquired using an inverted epifluorescence microscope (Nikon Eclipse Ti, Nikon Corporation, Tokyo, Japan) and scientific CMOS camera (Flash4.0 V2, Hamamatsu, Japan) and an EoSens mini MC-1370 fast camera (Mikrotron GmbH, Unterschleissheim, Germany) for high frame rate imaging. ImageJ software, downloaded from the National Institutes of Health, was used for image analysis and the preparation of figures. Code written using Matlab R2014a was used for image analysis tailored to the specific needs of cell counting and morphology detection.

All error bars of data shown in graphs and figures were calculated by average values and standard deviation of repeated experiments.

Conclusions

Using DLD devices, we have successfully demonstrated a measurement tool for cell deformation among three cell lines (normal breast epithelial cells, MCF10A, breast cancer cells MCF7 and metastatic breast cancer cells MDA-MB-231). Both using direct and indirect measurement, we are able to measure the softness level of each cell type. To summarize, non-malignant MCF10A cells show low deformation. Invasive MDA-MB-231 cells show high deformation, while MCF7 cells exhibit an intermediate deformation level. Furthermore, the deformability-based sorting in DLD device was illustrated for a mixture of MDA-MB-231 cells and MCF-7 cells. Although the performance does not give high purity (~71%), the sorting capability based on deformability is confirmed. The optimization of design is next step in this work.

Acknowledgements

We thank Stefan Holm for his design of DLD devices in this project. Another thanks to Thuy-Dung Nguyen, Vuong D. Nguyen and Ha T. Le for different image analysis tools which were specifically developed for this purpose. Finally, we thank Kushagr Punyani for his contribution of the soft-particles obtained from Prof. Guck's lab (TU Dresden, Germany). This work was carried out within NanoLund at Lund University with funding from the Child Cancer Foundation (MT2013-0031), LAPASO (EU FP7 project 607350) and the Swedish Research Council (VR) grant no. 2015-05426. All device processing was conducted within Lund Nano Lab.

References

1. Huang LR, Cox EC, Austin RH, & Sturm JC (2004) Continuous particle separation through deterministic lateral displacement. *Science* 304(5673):987-990.
2. Inglis DW, Lord M, & Nordon RE (2011) Scaling deterministic lateral displacement arrays for high throughput and dilution-free enrichment of leukocytes. *Journal of Micromechanics and Microengineering* 21(5):054024.
3. Civin CI, *et al.* (2016) Automated leukocyte processing by microfluidic deterministic lateral displacement. *Cytometry. Part A : the journal of the International Society for Analytical Cytology* 89(12):1073-1083.
4. Zeming KK, Salafi T, Chen CH, & Zhang Y (2016) Asymmetrical Deterministic Lateral Displacement Gaps for Dual Functions of Enhanced Separation and Throughput of Red Blood Cells. *Scientific reports* 6:22934.
5. Yamada M, Seko W, Yanai T, Ninomiya K, & Seki M (2017) Slanted, asymmetric microfluidic lattices as size-selective sieves for continuous particle/cell sorting. *Lab on a chip* 17(2):304-314.
6. Louterback K, *et al.* (2012) Deterministic separation of cancer cells from blood at 10 mL/min. *AIP Adv* 2(4):42107.
7. Liu Z, *et al.* (2013) Rapid isolation of cancer cells using microfluidic deterministic lateral displacement structure. *Biomicrofluidics* 7(1):11801.
8. Okano H, *et al.* (2015) Enrichment of circulating tumor cells in tumor-bearing mouse blood by a deterministic lateral displacement microfluidic device. *Biomedical microdevices* 17(3):9964.
9. Holm SH, Beech JP, Barrett MP, & Tegenfeldt JO (2011) Separation of parasites from human blood using deterministic lateral displacement. *Lab on a chip* 11(7):1326-1332.
10. Holm SH, Beech JP, Barrett MP, & Tegenfeldt JO (2016) Simplifying microfluidic separation devices towards field-detection of blood parasites. *Anal Methods-Uk* 8(16):3291-3300.
11. Santana SM, Antonyak MA, Cerione RA, & Kirby BJ (2014) Microfluidic isolation of cancer-cell-derived microvesicles from heterogeneous extracellular shed vesicle populations. *Biomedical microdevices* 16(6):869-877.
12. Wunsch BH, *et al.* (2016) Nanoscale lateral displacement arrays for the separation of exosomes and colloids down to 20 nm. *Nature nanotechnology* 11(11):936-940.
13. Pariset E, Agache V, & Millet A (2017) Extracellular Vesicles: Isolation Methods. *Advanced Biosystems* 1(5):1700040.
14. Louterback K, *et al.* (2012) Deterministic separation of cancer cells from blood at 10 mL/min. *Aip Adv* 2(4).
15. Beech JP, Holm SH, Adolfsson K, & Tegenfeldt JO (2012) Sorting cells by size, shape and deformability. *Lab on a chip* 12(6):1048-1051.
16. Henry E, *et al.* (2016) Sorting cells by their dynamical properties. *Scientific reports* 6:34375.
17. Subik K, *et al.* (2010) The expression patterns of ER, PR, HER2, CK5/6, EGFR, Ki-67 and AR by immunohistochemical analysis in breast cancer cell lines. *Breast cancer: basic and clinical research* 4(4):35-41.
18. Geltmeier A, *et al.* (2015) Characterization of Dynamic Behaviour of MCF7 and MCF10A Cells in Ultrasonic Field Using Modal and Harmonic Analyses. *PLoS One* 10(8):e0134999.
19. Mansor MA & Ahmad MR (2015) Single Cell Electrical Characterization Techniques. *Int J Mol Sci* 16(6):12686-12712.
20. Hussein M, *et al.* (2019) Breast cancer cells exhibits specific dielectric signature in vitro using the open-ended coaxial probe technique from 200 MHz to 13.6 GHz. *Scientific reports* 9(1):4681.
21. Smolyakov G, *et al.* (2016) Elasticity, adhesion, and tether extrusion on breast cancer cells provide a signature of their invasive potential. *ACS Appl Mater Interfaces* 8(41):27426-27431.
22. Li QS, Lee GY, Ong CN, & Lim CT (2008) AFM indentation study of breast cancer cells. *Biochem Biophys Res Commun* 374(4):609-613.
23. Hou HW, Li Q, Lee G, & Lim CT (2008) Deformability study of breast cancer cells using microfluidics. *Biomedical microdevices* 11(11):557-564.
24. Kim YC, Park SJ, & Park JK (2008) Biomechanical analysis of cancerous and normal cells based on bulge generation in a microfluidic device. *Analyst* 133(10):1432-1439.
25. Guck J, *et al.* (2005) Optical deformability as an inherent cell marker for testing malignant transformation and metastatic competence. *Biophysical journal* 88(5):3689-3698.
26. Girardo S, *et al.* (2018) Standardized microgel beads as elastic cell mechanical probes. *Journal of Materials Chemistry B* 6(39):6245-6261.

Supplementary Information (SI)

Softness sorting for cancer cells in deterministic lateral displacement.

Trung S.H. Tran^a, Jason P. Beech^a, Bo Baldetorp^b and Jonas O. Tegenfeldt^a

(a) Division of Solid State Physics & NanoLund, Lund University

(b) Department of Oncology, Lund University

DLD device configuration

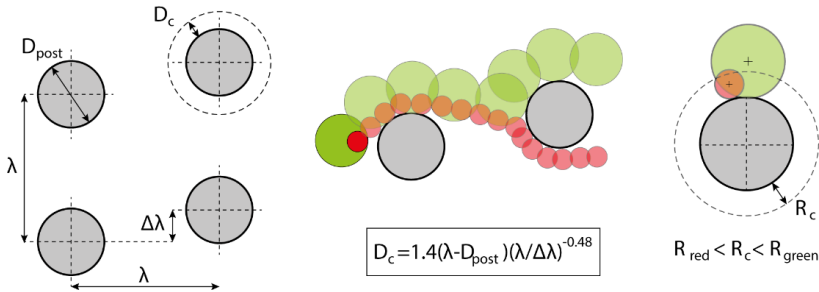
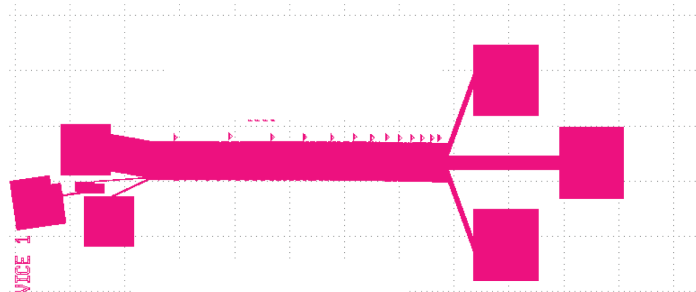


Figure 1. DLD design parameters

A DLD device, as shown in figure 1, consists of an array of posts with λ spacing between the centers, shifted laterally by a distance $\Delta\lambda = \lambda/N$, where N is usually an integer number ($2 \leq N \leq 100$). N is called the period of the array since the array repeats itself after N rows. Particles which are smaller than a critical size R_c flow in a zig-zagging pattern following the flow stream while ones whose size $R \geq R_c$ are transported in displacement mode at an angle defined by the obstacle array. The trajectories of different particles depending on their size. The critical diameter can be estimated using an empirical equation proposed by Davis (1):

$$D_c = 1.4GN^{-0.48}$$

The DLD device which was mainly used in the measurement and separation was shown in figure 2. The device has three inlets, 6 outlet and range of 13 critical sizes. To prevent the clogging of the sample, an upstream filter array is integrated into the device (inlet 2).



Gap	[Grid of small squares representing gap sizes]														
Dc	ln 1	ln 2	IN 3												
	<7.82	7.82	8.91	10.13	10.95	11.95	13.09	13.93	15.03	15.99	17	17.95	19	19.98	>20
	Outlet RE1		Outlet RE2			Outlet RE3		Outlet RE4		Outlet RE5			Outlet RE6		

Figure 2. Chirp DLD device was used in the experiments

Soft particles

Polystyrene and Polyacrylamide particles (both diameter $15\mu\text{m}$, and Young's modulus of $3\text{-}3.6\times 10^9\text{Pa}$ and $2.8\text{-}6.7\times 10^2\text{Pa}$) are used as a reference for the calibration process. While the rigid particles (Polystyrene) are unaffected when increasing flow rate, the soft particles (Polyacrylamide) are expected to deform and therefore be less displaced at higher shear rates.

Cell Characteristics

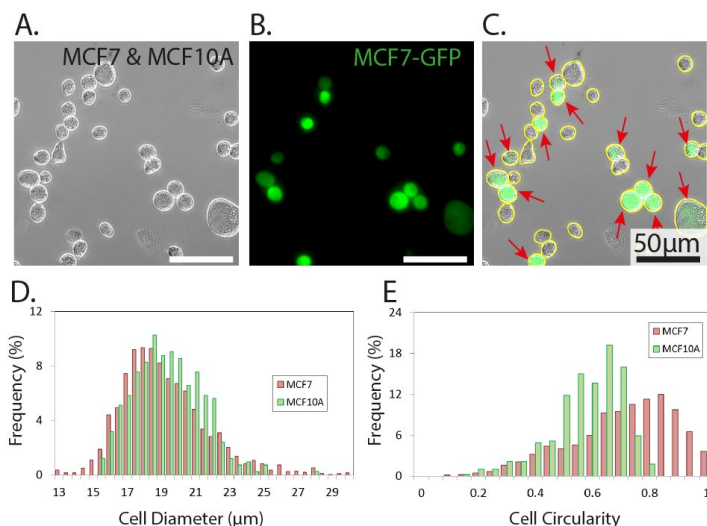


Figure 3. Microscopic inspection and analysis of MCF7 and MCF10A for size and shape. (A.) A bright-field image provides an overview of MCF7 and MCF10A cells which are similar in size and morphology. (B.) Fluorescence image of MCF7 (labeled with GFP) is used to identify MCF7 cells in the mixture. (C.) MCF7 cells labelled by green color (red arrows) are distinguished to MCF10A in a merged image. Cell boundary (yellow) are detected by image processing for size and shape measurements. (D.) Cell diameter and (E.) circularity distribution of both MCF7 and MCF10A cells were determined.

The size and shape of MCF7 and MCF10A cells was determined by optical microscopy of a suspended mixture of the two cell types (Fig 3). Our MCF7 cells express GFP and were identified using fluorescence (red arrows). The two cell types were classified into three groups (single cells, double cells and aggregates (three cells or more) and the cell area and circularity measured. Fig 3C shows cell area and circularity for a population of MCF7 cells after trypsinization to release them from culture flasks. Some rare aggregates were as large as $10\,000\ \mu\text{m}^2$ but for clarity the plot is limited to the range 0 to $3000\ \mu\text{m}^2$. Due to the spherical shape of suspended cells, a circularity number can present for cell shape or morphology.

Cell aggregation is a significant practical challenge for single cell analysis. Cancer cells which divide uncontrollably form aggregates or clusters more easily than normal cells (12% of cells in aggregates for MCF7 and only 3% for MCF10A for the present study). In microfluidics devices, cell aggregates are a common cause of clogging. To prevent clogging in the DLD array, an upstream filter array is integrated into the device, which captures aggregates. Single cells are able to pass the filter and are guided to the main DLD array for evaluation of deformation and for sorting.

The size distributions of MCF7 and MCF10 cells are presented in figure 3. The cells have the same average size ($D=17\mu\text{m}$) and shape (close to round with $C=0.8$). However, the variance in size and shape of the cancer cells is somewhat wider than for the normal cells (table in Fig.4). The variation in size and shape, as well as disorganized arrangement of a cancer cell, was mentioned in the “The hallmarks of cancer” (2). To summarize, suspended MCF7 cells easily form aggregates (12%) and they have a wider distribution in size ($D=19\pm 4\mu\text{m}$) with uniform shape ($C=0.76\pm 0.12$) while MCF10A are more uniform in size and shape and show less aggregation (3%).

Simulation

A simple model of DLD array was simulated to be able extract the shear and pressure gradient and distribution. Those parameters are believe as the factors of cell deformation. While the maximum shear is placed at the smallest distance between posts, the pressure gradient points out a position which cell was highest deformed.

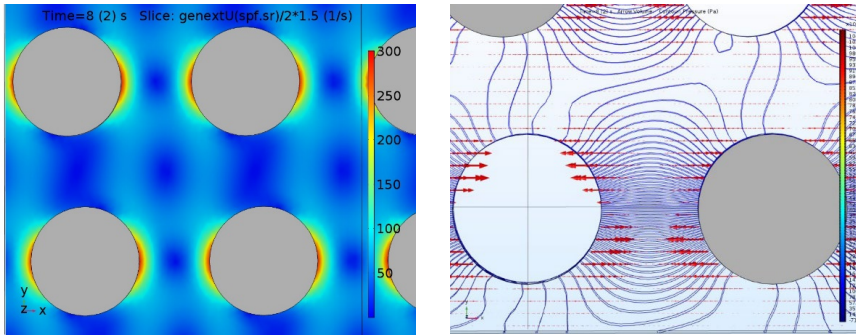


Figure 4. Simulation results of shear and pressure gradient in a DLD array. A) Shear gradient shows a highest value at the gap. B) Pressure gradient presents a largest effect before cell entering the gap.

Effect of pressure on cell size and viability

To avoid the contamination among the experiments or the effect of pressure change, each experiment was conducted in an unused DLD device. The quality of the sample as well as the sample size distribution are checked by size measurements at the end of array. Figure 4 shows size distribution data for MCF7 cells after being exposed to the DLD device at a variety of applied pressures. The results indicate that changing the applied pressures does not introduce a bias with respect to the size of cells that are collected at the end of the device.

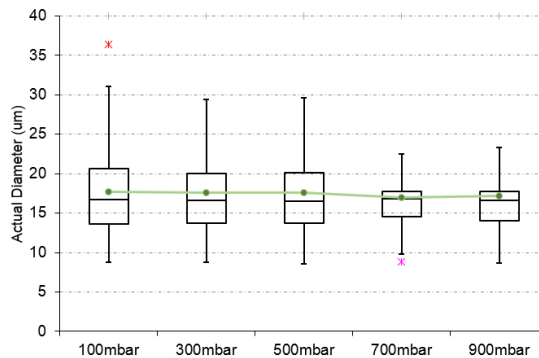


Figure 5. Equilibrium size of cells extracted from the device after being exposed to flow through the device at a range of pressure. For each pressure, a new device and new sample were used.

To confirm the effect of high pressure on cell viability, sorted cells were collected to perform the cell viability test and cultured in 3days to check the cell proliferation. No significant difference was recorded in viability tests as well as cell proliferation assay.

Cell distribution comparison

In separate experiment, we found that staining the MCF7 cells with the nuclear stain DAPI affected the apparent deformability of the cells as compared to MCF10A (Fig. 6). DAPI is a membrane impermeable dye although it can penetrate the membrane at high concentrations (300 nM DAPI stain solution in PBS). We therefore suspect that the DAPI-stained cells represent the dead MCF7 cells while the viable MCF7 cells are unstained. This may explain the large difference in deformability. The dead cells are highly deformable, while the MCF7 and MCF10A cells have overlapping deformability. Further investigations are necessary to establish the exact identity of the cells.

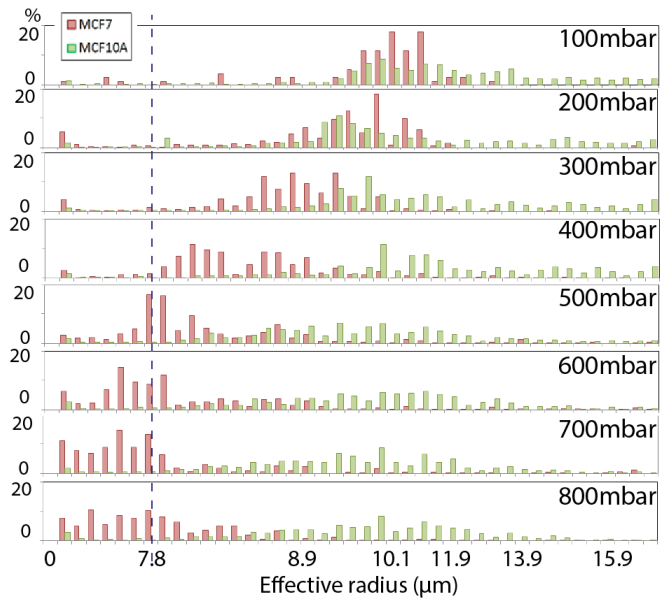


Figure 6. A comparison between stained MCF7 and MCF10A cells for different applied pressures. Soft stained MCF7 cells deform while the harder MCF10A cells are not very affected by the increased pressure. Sorting of the two cell types can be obtained from 400mbar.

References

1. Davis JA, *et al.* (2006) Deterministic hydrodynamics: taking blood apart. *Proceedings of the National Academy of Sciences of the United States of America* 103(40):14779-14784.
2. Hanahan D & Weinberg RA (2000) The Hallmarks of Cancer. *Cell* 100(1):57-70.

Paper III



Electrokinetic rotation of red blood cells in deterministic lateral displacement devices

Bao D. Ho,^a Trung S.H. Tran,^a Jason P. Beech, Jonas O. Tegenfeldt*

Division of Solid State Physics and NanoLund, Lund University, Professorsgatan 1, 22363 Lund, Sweden.

^(a): authors contributed equally

^(*)E-mail: jonas.tegenfeldt@ftf.lth.se

Abstract. *We demonstrate the use of electrokinetics to control the orientation of red blood cells in deterministic lateral displacement (DLD) devices. Selecting a specific orientation of a non-spherical particle in a DLD device makes it possible to select which dimension of the particle that determines its effective size. While geometry of the device, fluid shear forces and steric interactions with the pillars have been used to control the orientation of particles in previous work, the effect is not easily predicted, nor can it be easily turned on and off. Electrokinetics can be used in a well-controlled way to apply a force on particles that can be used to distinguish between particles with different dielectric and electrical properties. We will build on that, but instead use electrokinetics to impose an effective torque on the particles. In this way we impose the desired orientation so that the effective size of the particles reflects the dimension of interest of our particle. We demonstrate the basic principle on red blood cells, increasing their effective size by a factor of around 1.5, from below 3.47 μm to 4.44 μm . We expect that the ability to improve the contrast in separation parameters between RBCs and other cells based on their shape to find a wide range of applications in biological sorting, in particular for separation of RBCs from other kinds of cells and pathogens.*

1. Introduction

Particle separation is important for various applications ranging from clinical pharmacology to diagnostic devices in the field of medicine and biology. One particular sample widely used in clinical studies is blood, consisting of different cells such as white blood cells (WBCs) a.k.a leukocytes, red blood cells (RBCs) a.k.a erythrocytes, and platelets. Under different physiological circumstances, distinct morphological changes are observed in RBCs affecting the cells' deformability. The extent of this deformation varies for different disease pathologies. For instance, cancerous blood cells are known to have a more deformable phenotype as opposed to healthy cells [1] whereas a less deformable phenotype is observed in the case of Sickle-cell disease (SCD) and Malaria [2]. In malaria higher stiffness of the parasitized RBCs is exhibited for more advanced stages of the disease. In addition, the physical and mechanical properties of a cell change with its size. Therefore, valuable information about the state of health or the phase in cycle of an individual cell can be extracted by investigating the cells' physical properties.

The most common techniques used for blood cell separation are fluorescence activated cell sorting (FACS) and magnetic-activated cell sorting (MACS) yielding high resolution results with the downside that the necessary sample labeling may perturb the cells. In recent years different microfluidic particle separation devices have been introduced as cheaper, more flexible and less time-consuming alternative solutions. One particular advantage of these devices is the ability of working at nanometer or micrometer scale, close to the size of the particles being investigated.

Deterministic lateral displacement (DLD) is a microfluidic separation technique introduced by Huang *et al.* in 2004, where particle separation based on size was reported with resolution as low as 10 nm [3]. The particle separation in this passive device is based on interaction between particles, carried by a fluid stream, and an array of posts. One important characteristic of DLD is that, being a continuous method, it can easily be integrated with upstream and downstream processes. In the first instance, DLD was shown to be an extremely good size separation technique but advances in the method have since shown it to be rather versatile with demonstrated sorting based on factors such as shape [4-7] and deformability [5]. In 2008, Chang and Cho introduced a virtual DLD device with varying critical size [8]. This tunability was achieved by employing negative dielectrophoretic (DEP) forces in an array of virtual obstacles. In electrodeless or

insulator-based DEP (iDEP) the gradients in the electric field are created throughout the entire device by insulating microstructures between the electrodes using fabrication techniques such as soft lithography [9] or imprint lithography [10]. In this way the fabrication complexities involved with integrated microelectrodes and other limitations commonly encountered in the presence of electrodes are avoided. Besides, by using iDEP the device can be operated at DC fields as well as low frequencies without the need to be concerned about electrolysis where the separation takes place [11]. In 2003, Cummings *et al.* investigated the effect of iDEP in continuous separation of particles through an array of insulating obstacles in two separate studies [12, 13]. It was concluded that using DC fields, the flow of 200nm particles can be controlled from ideal electrokinesis to streaming DEP to trapped particles. In 2009 Beech *et al.*, introduced a method called DEP-DLD where DEP and DLD are integrated [14]. The particle separation behavior of the device was investigated using AC fields at low frequencies and it was shown that the critical size can be readily decreased by half or less. In a DEP-DLD device the high resolution of DLD is combined with the tunability of DEP. For example, by changing the applied frequency, different properties of the cells being investigated can be probed. In 2014 Kruger *et al.* investigated the possibility of separating red blood cells (RBC) in DLD devices in a simulation study and obtained promising results [15].

Controlling the orientation of particles in a DLD device gives greater control over separation behavior and can make it possible to separate populations that vary in shape in a way that is otherwise not possible using conventional DLD. The basic idea is to shift the orientation so that the dimension of interest determines the effective size of the particle. For example, RBCs can be described by two numbers, the thickness and the overall diameter. By orientating the RBC, one can decide which of the two numbers will correspond to the effective size of the cell. The effective size will finally determine the trajectory of the cell through the DLD array. Zeming *et al.* [16] used post shapes to gain some control over particle orientation and improve the separation of RBCs. Holm *et al.* used channel depth to control RBC orientation making it possible to choose to separate by cell diameter or cell thickness [7]. In the present work we show that we can use electrokinetic forces to control cell orientation and show also the effect that this has on cell behavior in DLD devices. Using electrokinesis in this way has the advantage over the geometry-based approaches in that it can be applied to any kind of existing DLD device fabricated in an insulating material independent on depth of the device. Finally, it can be switched on and off or tuned to optimize separations under varying conditions without the need to fabricate new dedicated devices.

2. Theory

Deterministic Lateral Displacement

A deterministic lateral displacement (DLD) device, as shown in Fig. 1, consists of an array of posts with λ spacing between the centers, shifted laterally by a distance $\Delta\lambda = \lambda/N$, where N is usually an integer number

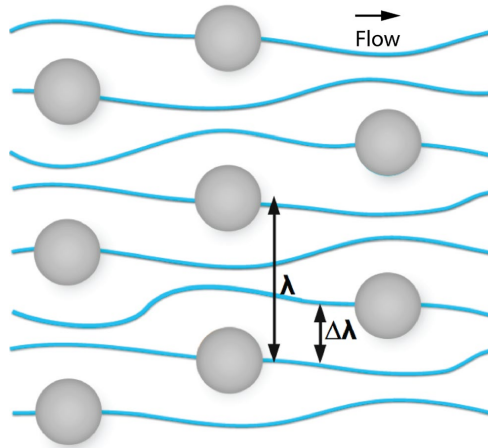


Fig 1 A simplified DLD array with distance λ between two posts. The row shift is $\Delta\lambda$ and the period N is 3.

($2 \leq N \leq 100$). N is called the period of the array since the array repeats itself after N rows.

Particles which are smaller than a critical diameter D_c flow in a zig-zagging pattern following the flow stream while ones whose size $D \geq D_c$ are transported in displacement mode at an angle defined by the obstacle array. Fig. 2(a) shows the trajectories of different particles depending on their size. The critical diameter can be estimated using an empirical equation proposed by Davis [17]:

$$D_c = 1.4GN^{-0.48} \quad (1)$$

Where G is the width of the gap between 2 posts ($G = \lambda - \text{Post Diameter}$).

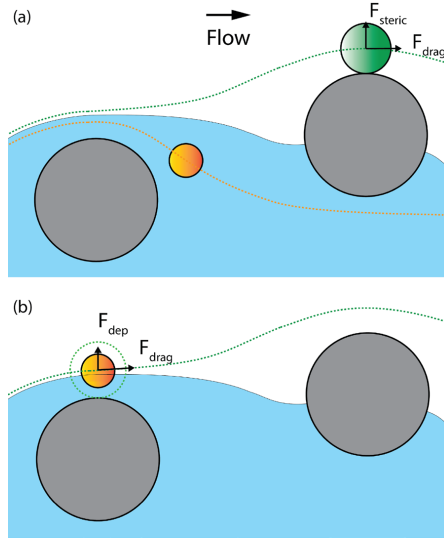


Fig 2 Sorting mechanism in a conventional DLD device and in an electrokinetic DLD device. (a) Trajectories of particles in a DLD device. The orange particle, which is smaller than the critical size, follows the stream while the big green particle “bumps” into the posts and switches to another stream. (b) Trajectories of a particle in a DLD device under DEP force. Although the particle is smaller than the critical size, the dielectrophoretic force makes it appear larger and travel in displacement mode.

Electrokinetics

In this paper, we refer to electrokinetics as a general term for all dynamic processes affecting particles when an electric field is applied along a DLD device. Dielectrophoresis (DEP) is the motion of particles subjected to a non-uniform electric field. The interaction of the field with the particle’s dipole moment exerts a force on the particle [18]. The force magnitude and direction are dependent on the particles’ geometry (size and shape), dielectric properties, and (at low frequency) electrical conductivity, in relation to the dielectric property and electrical conductivity of the buffer they are suspended in. This phenomenon can be employed in microfluidic separation and sorting techniques. Fig. 2(b) illustrates the case the particle experiences negative DEP in a DLD array. In particular, due to the presence of the PDMS posts inside the channel, the electric field is distorted around the posts and the maxima of electric field are at the sides of posts which are tangential to the flow. If the particle experiences negative DEP, it moves away from the posts that it approaches on its way through the device. In other words, although the particle is smaller than the critical diameter, it behaves like a larger particle and is deviated from the flow stream where it originally resided.

Although DEP has been cited as the cause of displacement enhancement in an electrokinetic DLD device [19], other electrokinetic phenomena take place simultaneously when the voltage is applied, including electrophoresis (motion of a particle in a field due to its charge) and electro-osmotic flow (motion of an ionic solution near a charged wall in a field). These phenomenon may also contribute to the net movement of particles in an electrokinetic DLD. In the scope of this work, we are interested in employing the total

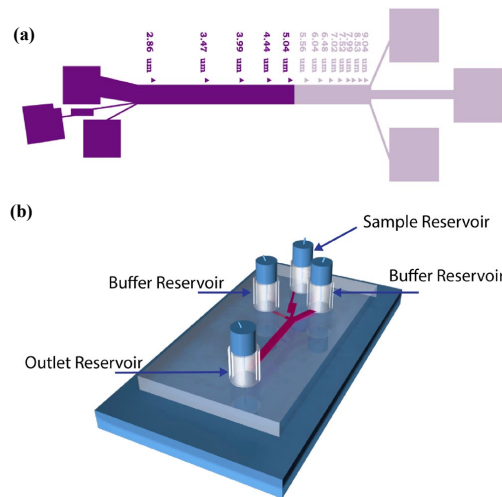
rotational effect of RBCs in an electrokinetic DLD device for cell sorting and leave more detailed characterization of the underlying principles for future work.

3. Experimental

Device

We used soft-lithography to make poly-(dimethylsiloxane) (PDMS) devices for our experiments. The detailed procedure can be found in Holm *et al* [7]. We modified the design by Holm for sorting blood and *Trypanosoma cyclops* to run our Electrokinetic DLD experiments with red blood cells. The layout of the original design is shown in Fig. 3(a). In order to achieve high electric field, we shortened the device by cutting it in half and pinched the outlet hole near the cut line.

The complete device after tubing is illustrated in Fig. 3(b). The device has four reservoirs: two buffer reservoirs, a sample reservoir, and an outlet reservoir. The four blue cylinders showed in the figures are parts of the tubes connecting to the pressure pump and the four small wires are platinum electrodes connected to the voltage source.



Equipment

The flow of blood sample and buffer inside the PDMS device was driven by a pressure gradient. Pressure at the sample reservoir and the two buffer reservoirs was regulated by an over-pressure controller (MFCS-4C, Fluigent, Paris, France) via three plastic tubes and connectors (Fig. 4). The controller maintained a stable pressure difference in the range of 0 – 60 mBar between the sample/buffer reservoirs and the outlet reservoir, which was left open to atmospheric pressure. To supply a high-voltage bias across the channel of the device, we used a function generator (33120A, Hewlett Packard, Palo Alto, CA, USA) together with a 100X amplifier (BOP 1000M, Kepco, Flushing, NY, USA), yielding a sinusoidal AC voltage of up to 1000 Vpp. One terminal of the voltage source was connected to the platinum electrodes immersed into the buffer reservoirs and the sample reservoir and the other terminal was attached to the platinum electrode embedded into the outlet reservoir. Since the cross-section of the buffer/outlet tubes is much larger than that of the microfluidic channel, the electrical impedance of these tubes is much lower than the channel impedance and the voltage difference provided by the voltage source is assumed to be distributed mainly across the channel. Blood cells in the device were imaged through an inverted microscope (Eclipse TE2000-U, Nikon Corporation, Tokyo, Japan) with a 10x objective (Nikon Plan Fluor 10x/0.30 DIC L/N1) or a 20x objective (Nikon Fluor 20x/0.50W DIC M/N2). The images and movies of the experiments were captured using a CMOS camera (Neo sCMOS, Andor Technology, Belfast, Northern Ireland).

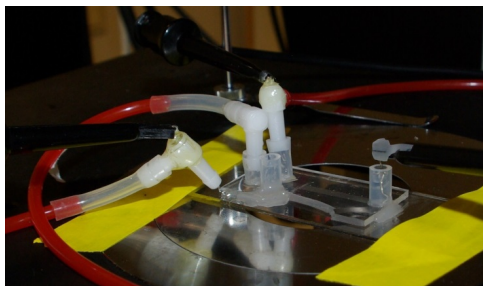


Fig 4 The Electrokinetic DLD device with microfluidic and electrical connections. The sample and buffer reservoirs (on the left of the device) were connected to an over-pressure pump by three plastic tubes; one of the tubes was unplugged for visibility of one of the reservoirs. The buffer reservoirs and the output reservoir (on the right of the device) are connected to the AC voltage source through platinum electrodes.

Sample preparation

The blood sample was extracted from healthy donors following a standard procedure. A sterile needle (Haemolance+ low flow, Haemedic, Sweden) is used to prick the donors' finger. The blood drop (10 μ L) is collected by a sterile pipette tip and then diluted into 1000 μ L of autoMACS[®] running buffer (#130-091-221, Miltenyi Biotec, Bergisch Gladbach, Germany). The buffer (pH 7.2) contains phosphate buffered saline (PBS), bovine serum albumin (BSA), EDTA, and 0.09% sodium azide.

Experimental procedure

Fifty μL of diluted blood sample was added to the inlet reservoir and the buffer reservoirs were filled with autoMACS[®] running buffer. The outlet reservoir was also filled with the buffer to allow for the electrical connection. The experiment could be run with or without an applied voltage. Movies were taken all over the device. However, to quantify the displacement and effective size of the RBCs, we focused on a small region near the outlet reservoir, which has the nominal critical size of $5.04\ \mu\text{m}$ (Fig. 5(a)). The AC voltage was ramped up from 0 V to 1000 Vpp, in steps of 200 Vpp. For each voltage value, we captured a corresponding microscopic movie. In each movie, we counted the number of RBCs passing through every gap between nearby posts of a chosen row. The cell counts were converted to percentage and plotted as a function of the displacement.

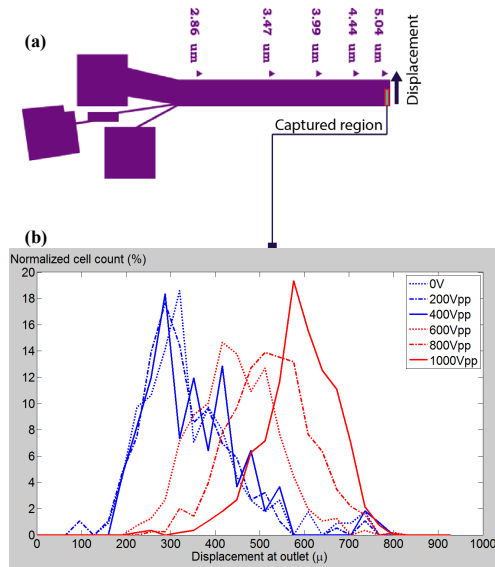


Fig. 5 Lateral displacement of RBCs in relation to applied voltage. (a) The captured region where displacement of RBCs were analyzed. (b) Distribution of RBCs at the captured region. The graph shows cell counts (%) as a function of lateral displacement at a row inside the captured region. There are six curves corresponding to six AC voltage values used in our experiments. The AC signals were sinusoidal and at 100 Hz.

4. Results and Discussion

Orientation of red blood cells in Electrokinetic DLD device

RBCs have the shape of a biconcave disk, with diameter of around $6 - 8 \mu\text{m}$ and thickness of around $2 - 2.5 \mu\text{m}$. Due to this specific geometry, orientation of the cells in a normal DLD device is dependent on the fluid stream they reside in. When RBCs travel in a straight channel or in the middle of two posts, they tend to align horizontally like Frisbees flying in mid-air. Looking at a microscopic image taken from the top of the device, one can observe the cells as circles. However, when the RBCs switch to fluid streams near a post, they are in favor of leaning against the post and orient vertically like bicycle tires. From the top of the device, one sees the cells as thin, rounded rectangles (Fig. 6 (a) and Movie 1). This phenomenon dictates the effective size of the cells in a DLD device, making them appear as small as their thickness [7].

With a sufficient electric field gradient applied across the device, this vertical orientation of the RBCs when they move near the posts is overridden. As can be seen in Fig. 6(b) and Movie 2, the cells appear consistently as Frisbees when they flow in the post array, disregarding their position with respect to posts. The effective size of the cells is approximately equal to their diameter.

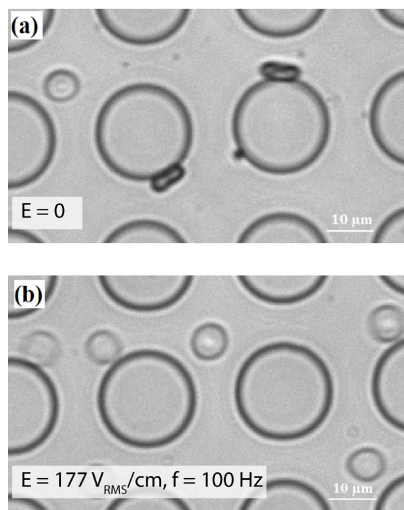


Fig. 6 Orientation of red blood cells in a DLD device. (a) In the absence of an AC field ($E = 0$), there are two types of orientation of RBCs depending on their positions with respect to a post. (b) When electric field was turned on ($V = 1000 \text{ Vpp}$, $|E| \approx 177 \text{ V}_{\text{RMS}}/\text{cm}$), RBCs orient horizontally like Frisbees flying in mid-air, disregarding the fluid stream they were in.

Distribution of red blood cells near the outlet reservoir

To quantify the effect of field strength on RBCs in Electrokinetic DLD devices, we analyzed the displacement of the cells at a region near the outlet. Fig. 5(b) shows the distribution of RBCs measured at the end of our device. There are six curves corresponding to the six AC voltage amplitudes we used, ranging from 0 to 1000 Vpp. As can be seen from the figure, when the applied voltage is increased to 600 Vpp, the displacement of the RBCs starts to change. This can be explained by the change in their orientation due to electrokinetic effects, making them appear larger when in contact with a post, forcing them to move in displacement mode throughout the device.

Effective size of RBCs in DEP-DLD

The bell-shaped curves in Fig. 5(b) can be fitted into normal distributions to estimate the effective size of the RBCs in the device (Curve Fitting application of MATLAB R2014a (The MathWorks, Natick, MA, USA)). Fig. 7 shows the fitted data. The blue diamond marks represent the mean displacement of RBCs at each voltage value and the error bars correspond to one standard deviation. We also show the critical diameter values indicated by the dotted lines to help estimate the effective size of the cells in our device. For example, by looking at the graph one can see that when a voltage of 600 Vpp was applied, RBCs behave as spheres of diameters in the range of 3.47 μm to 3.99 μm .

In Fig. 7, one can see that the error bars are significant in comparison to the change in effective size over the range of voltages used. There are two main possible factors causing this phenomenon. First, the RBCs already have their own size distribution, both in diameter and thickness. Second, as can be seen from Movie 3, the orientation of RBCs while moving in the DLD arrays is quite stochastic. In particular, in addition to pure vertical and horizontal orientations the RBCs may have intermediate orientations that put their effective size in the range between their thickness and their diameter. We believe that the second effect contributes the most to the variation seen in Fig. 7.

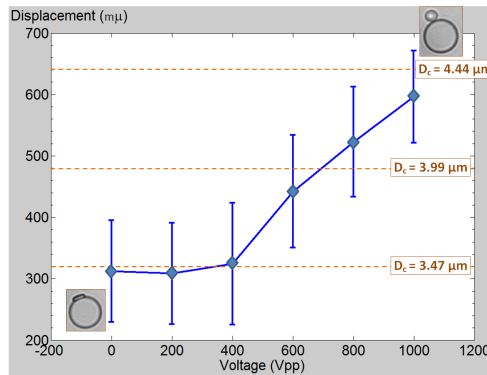


Fig. 7 The displacement of RBCs as a function of applied voltage, assuming they have normal distribution. The dotted lines marked with critical diameter values are included to help estimate the effective size of the cells in our device.

It should be noted that although the biggest size shown in Fig. 7 is 4.44 μm , it does not reflect the actual diameter of the RBCs. The reason for this is that we only use half of the device, which has highest critical size value of 5.04 μm , meaning that even if the cells were as large as 8 μm , they would be still displaced to the same position as the ones having the diameter of 5.04 μm . This drawback of the device can be avoided with a different design covering the full range of relevant effective sizes.

Effect of medium conductivity

Since AutoMACS® is a PBS-based medium for use with live cells, the ionic strength is high and thus, the electrical conductivity is relatively high, 1660 mS/m. The Joule heating is given by the power generated by unit volume:

$$\frac{\Delta P}{\Delta V} = E^2 \sigma$$

E is the magnitude of the electric field and σ is the conductivity. The effect raises the temperature of the devices and this can cause damage to the RBCs after the devices have been running for an extended amount of time (Movie 5, ESI).

To circumvent this issue, a medium with lower ionic strength can be used. To decrease the ionic strength but at the same time keeping the isotonic balance, a solution of sucrose 10% w/v was mixed with AutoMACS

at a ratio of 1:1. Unlike glucose, sucrose molecules do not penetrate the cell membranes and consequently a solution of sucrose at 10% w/v, which is isosmotic, is also isotonic. A small amount of NaOH was also added to keep the pH close to that of whole blood. The pH was measured at 7.37 and the conductivity was measured at 810 mS/m.

Red blood cells were run in the same device as shown in Figure 5a, in the AutoMACS-sucrose medium, at an applied pressure of 5 mBar and at applied AC voltages of 100 Hz, 0 – 1000 Vpp. During the course of the experiments, no cell damage was observed. The cell counts as a function of lateral displacement are shown in Figure 8. Similar to the trend shown in Figure 5b, as the applied voltage increased, the lateral displacement also increased. However, compared to Figure 5b, the displacement is less at the same voltages. At 800-1000Vpp, the cells appear to split into two populations: one that assumes maximum rotation moving in the displaced trajectory while the other only rotating half-way, moving in the zigzagging trajectory. This suggests that the conductivity of the medium or its constituents also affect the extent to which the RBCs rotate and get displaced. Further optimization of the running medium is required to maximize rotation effect of RBCs in electrokinetic DLD devices while at the same time minimizing the Joule heating that can cause damage to the cells.

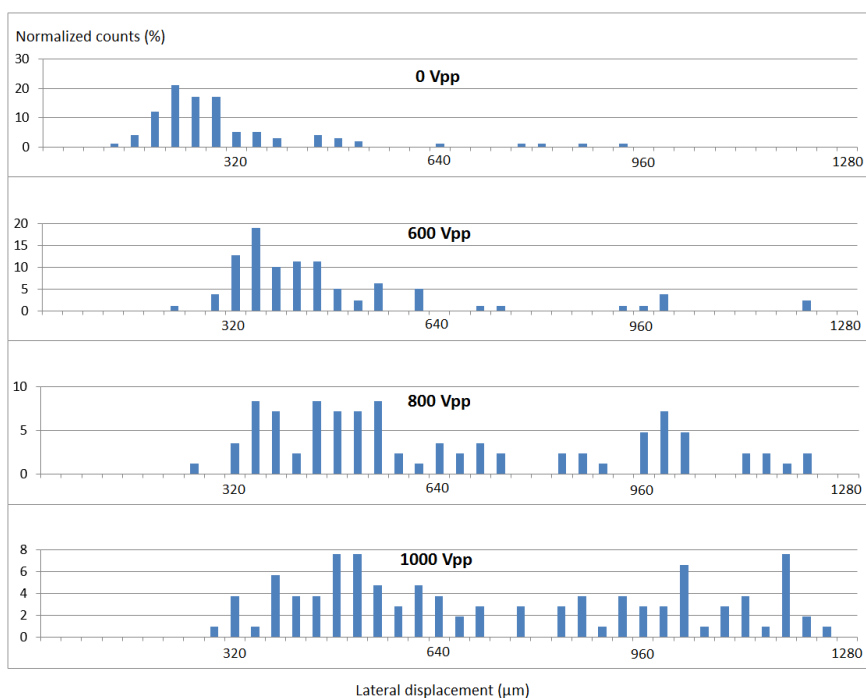


Fig. 8 The lateral displacement of RBCs at an applied pressure of 5 mBar and at different applied peak-to-peak voltages in a 810 mS/m isotonic medium (half AutoMACS, half sucrose 10%).

5. Conclusion and Outlook

In this work, we have shown the effect of electrokinetics on orientation of RBCs in DLD devices. This effect can be used as a tool to tune the effective size of RBCs by a factor of 1.5 (from below 3.47 μm to 4.44 μm in our work), which can be improved with more suitable design, keeping in mind that the diameter of the cells can be three times as large as their thickness. This phenomenon may open up for a wide range of applications in sorting RBCs from other kinds of cells and pathogens, thanks to the unique geometry of the RBCs.

There is plenty of room for future work. For example, modelling and simulation of RBCs in the devices could help us gain more insight into the mechanism behind the orientation of the RBCs. Wormlike parasites (e.g. Trypanosomes) can be tested in the same device and their displacement, as a function of voltage, can be compared with the current data of RBCs. If the difference in the effective critical diameter is significant, they can conceivably be separated by applying an AC voltage in DLD, as an alternative to fabricating DLD devices with specific depth [7], thereby opening up for increased throughput.

6. Acknowledgement

We are thankful to Hasti Yavari for her tremendous help with the experiments during the first stage of this work and to Stefan Holm for generously lending us the PDMS mold for fabricating DLD devices. This work was carried out within NanoLund at Lund University with funding from LAPASO (EU FP7 project 607350), the Child Cancer Foundation (MT2013-0031), and the Swedish Research Council (VR) grant no. 2015-05426. All device processing was conducted within Lund Nano Lab.

7. Electronic Supplementary Materials

A selection of videos of the results are available at <http://bit.ly/RBCRotationVideos> (case-sensitive)

Movie 1 - 0V_zoom_in.wmv: shows, at large magnification, the dynamics of RBC in the DLD device described in the main text with a pressure of 20 mBar applied across the device.

Movie 2 - 1000V_zoom_in.wmv: same as Movie 1, but with an additional AC voltage of 1000 V_{pp}, 100 Hz applied across the device.

Movie 3 - 0Vpp_large_FOV.wmv: same as Movie 1, only at a larger field of view.

Movie 4 - 1000Vpp_large_FOV.wmv: same as Movie 2, only at a larger field of view.

Movie 5 - Cell damage due to Joule heating: RBCs in irregular shapes after the device had been running for a while at an AC voltage of 1000 V_{pp}, 100 Hz. The applied pressure was 5 mBar. The video has been slowed down 2 times.

Movie 6 - Cell damage due to Joule heating (zoomed in).avi: same as movie 5, zoomed closer to the cells.

References

1. Guck, J., et al., *Optical Deformability as an Inherent Cell Marker for Testing Malignant Transformation and Metastatic Competence*. Biophysical Journal, 2005. **88**(5): p. 3689-3698.
2. Suresh, S., et al., *Connections between single-cell biomechanics and human disease states: gastrointestinal cancer and malaria*. Acta Biomaterialia, 2005. **1**(1): p. 15-30.
3. Huang, L.R., et al., *Continuous particle separation through deterministic lateral displacement*. Science, 2004. **304**(5673): p. 987-90.
4. Holm, S.H., et al., *Simplifying microfluidic separation devices towards field-detection of blood parasites*. Analytical Methods, 2016. **8**(16): p. 3291-3300.
5. Beech, J.P., et al., *Sorting cells by size, shape and deformability*. Lab on a Chip, 2012. **12**(6): p. 1048-1051.
6. Beech, J.P., et al., *Separation of pathogenic bacteria by chain length*. Analytica Chimica Acta, 2018. **1000**: p. 223-231.
7. Holm, S.H., et al., *Separation of parasites from human blood using deterministic lateral displacement*. Lab Chip, 2011. **11**(7): p. 1326-32.
8. Chang, S. and Y.H. Cho, *A continuous size-dependent particle separator using a negative dielectrophoretic virtual pillar array*. Lab on a Chip, 2008. **8**(11): p. 1930-1936.
9. Xia, Y.N. and G.M. Whitesides, *Soft lithography*. Annual Review of Materials Science, 1998. **28**: p. 153-184.
10. Chou, S.Y., P.R. Krauss, and P.J. Renstrom, *Imprint of Sub-25 Nm Vias and Trenches in Polymers*. Applied Physics Letters, 1995. **67**(21): p. 3114-3116.
11. Xing, X.X., M.Y. Zhang, and L. Yobas, *Interdigitated 3-D Silicon Ring Microelectrodes for DEP-Based Particle Manipulation*. Journal of Microelectromechanical Systems, 2013. **22**(2): p. 363-371.
12. Cummings, E.B., *Streaming dielectrophoresis for continuous-flow microfluidic devices*. IEEE Engineering in Medicine and Biology Magazine, 2003. **22**(6): p. 75-84.
13. Cummings, E.B. and A.K. Singh, *Dielectrophoresis in microchips containing arrays of insulating posts: Theoretical and experimental results*. Analytical Chemistry, 2003. **75**(18): p. 4724-4731.
14. Beech, J.P., P. Jonsson, and J.O. Tegenfeldt, *Tipping the balance of deterministic lateral displacement devices using dielectrophoresis*. Lab on a Chip, 2009. **9**(18): p. 2698-2706.
15. Kruger, T., D. Holmes, and P.V. Coveney, *Deformability-based red blood cell separation in deterministic lateral displacement devices-A simulation study*. Biomicrofluidics, 2014. **8**(5): p. 15.
16. Zeming, K.K., S. Ranjan, and Y. Zhang, *Rotational separation of non-spherical bioparticles using I-shaped pillar arrays in a microfluidic device*. Nature Communications, 2013. **4**.
17. Davis, J.A., *Microfluidic Separation of Blood Components through Deterministic Lateral Displacement*. Electrical Engineering. Vol. Doctors. 2008: Princeton.
18. Pethig, R., *Review Article-Dielectrophoresis: Status of the theory, technology, and applications*. Biomicrofluidics, 2010. **4**(2): p. 35.
19. Beech, J.P., P. Jonsson, and J.O. Tegenfeldt, *Tipping the balance of deterministic lateral displacement devices using dielectrophoresis*. Lab Chip, 2009. **9**(18): p. 2698-706.

Paper IV



Rapid duplication and alignment for multilayers of microfluidic PDMS devices

Trung S.H. Tran, Bao D. Ho, Oskar E. Ström, Jason P. Beech, and Jonas O. Tegenfeldt*

Division of Solid State Physics & NanoLund, Lund University, Professorsgatan 1, 22363 Lund, Sweden

(* E-mail: jonas.tegenfeldt@ftf.lth.se)

Abstract

Soft-lithography using polydimethylsiloxane (PDMS) cast on an SU-8 master is the most common approach to microfluidic device fabrication. While SU-8 master fabrication requires access to a cleanroom, the soft lithography can be performed in any lab. Masters degrade with use, however, and a return to the cleanroom is eventually necessary. We show a method to replicate masters with high resolution that is cheap, easy and does not require clean room access. We use PDMS devices as molds to “reverse mold” a master in UV curable optical glue. PDMS or Epoxy material has been used in a similar way but the approach is limited by duplication error and the need for anti-adhesion coatings. Replicating masters in UV curable glue instead allows us to produce identical, high resolution masters for soft lithography that do not require anti-adhesion treatments and that also allow multiple layers to be added to the master. Reservoirs can be added to the master and manual punching holes through PDMS, a source of inter-device variation, can thus be avoided. We successfully demonstrate functioning particle sorting in replicated devices based on deterministic lateral displacement (DLD). The high accuracy and precision of our replication process is especially important for DLD device because of their sensitivity to changes in their geometry.

Key words: Soft-lithography, secondary master, glue-mold, rapid duplication

Introduction

Microfluidics has been widely developed for chemical and biological applications. In the last decade, Micro total analysis system (uTAS) and lab-on-a-chip devices (1) have been rapidly developed and contributed to expand the field. Many of these devices have been fabricated by UV lithography processes on silicon or glass. These types of processes are quite expensive, complex and time consuming. In order to duplicate the device without repeating the lithography cycle, soft lithography technologies were introduced by Whitesides *et al.* (2). The advantage of soft lithography is that prototyping (using SU-8 master) is relatively simple and straightforward. For the typical research lab (1 to 100 devices) the startup costs are small (assuming a pre-existing clean room) and devices can be made one at a time as needed. Soft lithography has thus been applied in microfluidics (2), micro-optics (3), and BioMEMS (4).

In microfluidics fabrication, soft lithography based on Polydimethylsiloxane (PDMS) and SU-8 masters are commonly used. The advantages of optical transparency above 230nm (5) and easy fabrication (6), make the material mainly used for small scale fluidic systems (6) and surface replication(7). By using

commercial kits of PDMS, the process of replica molding is relatively cheap and accessible. The main difficulty of the fabrication is the production of masters. With standard lithography processes, the SU-8 masters achieve high-aspect-ratio microstructures but the wafers are fragile and the SU-8 polymer may detach after long term usage. Furthermore, the SU-8 masters are usually coated with an anti-adhesion layer before the soft-lithography process. So, the risk of damage to the master or loss of micro-patterns in the replication cycles limits the usefulness of the SU-8-master. Moreover, the requirement to make several SU-8 masters adds to the overall cost and it may cause additional repeatability of experiments.

In order to protect and extend the lifetime of the SU-8 master mold, a secondary mold is required. PDMS (8) and Epoxy (9) has been reported as useful options. For thermosetting polymers, the curing process is based on temperature and baking time. It has been reported that curing of the materials at elevated temperatures make the material shrink compared to the original mold dimensions (10). The influence of mixing ratio (base and curing agent) to the shrinkage is another consideration (10). Consequently, the duplication error of PDMS replicas between the original SU-8 structures and PDMS based mold was 24 μ m compared to 602 μ m width of channel (3.9%) and the minimum width was 101 μ m (8). In Epoxy-based mold, the error was observed 15 μ m compared to 518 μ m width of channel (2.9%) and the minimum gap was 75 μ m (9). Furthermore, the requirement of an anti-adhesion layer is usually required. To overcome these limitations, we propose an alternative material fabricated by a UV-curing process.

In our work, we are concerned about the duplication accuracy and its effect on a typical microfluidic sorting devices such as those based on deterministic lateral displacement (DLD). In this report, we have achieved a high-resolution replication by a UV-curable adhesive glue (duplication error less than 0.2 μ m compared to the channel width 540 μ m (0.03%) and the minimum gap was 3 μ m). Without the need of coating layer, independence of temperature as well as high stability and stiffness, glue-based mold is an attractive option for high resolution replication.

In addition to the robustness and absence of any anti-sticking requirements, many copies can be made and used in parallel increasing device fabrication turnover. Features at various scales (not easy to do in SU-8) can be selectively added, as needed for each application, such as reservoirs while the original SU-8 master can be stored and reused as backup if needed. For a PDMS device with few inlets and outlets, the punching process is quite simple and can be quickly done in a minute. Time consumption and punching errors are negligible unless a complicated device including a tens or hundreds of outlets are required. Furthermore, to achieve a high throughput in a sorting device, stacking multiple layers of devices is often necessary. However, the alignment process of PDMS devices is a practical challenge of repeatability, accuracy and time consumption. Rapid stacking (<1min for each layer) and precise alignment (layer difference error 100 μ m) are key benefits of our approach.

Experimental methods

Materials and instruments

In the lithography process, a master with a micro pillar array was fabricated. In a contact mask aligner (Karl Süss MJB3 and MJB4, Munich, Germany), negative photoresist SU8 (MicroChem, Newton, MA, USA) spun on a 3" silicon wafer was exposed to UV light through a chrome-mask designed in L-Edit 11.02 (Tanner Research, Monrovia, CA USA) and printed by Delta Mask (Delta Mask, Enschede, The Netherlands). For the soft lithography process, a 10:1 mixture (monomer: curing agent) of PDMS

(Sylgard 184, Dow Corning, Midland, MI, USA) was degassed, poured onto the glue-based mold then baked for 2 hours at 80°C.

UV-curable adhesive glue (Norland optical adhesive 63, NOA63, Norland, US), an UV light lamp (San Gabriel, CA 91778, US) and glass slides (Sigma-Aldrich) were used for the fabrication procedure. The glue-based molds were based on PDMS replicas of the SU-8 master.

Characterization was done by scanning electron microscopy (SU8010 Hitachi High-Technologies Corporation, Tokyo, Japan) of the PDMS stamps which were duplicated from the SU-8 master mold and the glue-based mold. Before electron microscopy imaging, a 10 nm thick layer of platinum and palladium (ratio 8:2) was sputtered onto the PDMS structures. Image analysis was conducted by ImageJ (National Institutes of Health, Bethesda, Maryland, US).

Fluorescently labelled polystyrene microspheres with diameters of 1 μm and 2 μm (Polyscience Inc.) were used to verify the sorting capability of the replicated devices. Particles were counted from images acquired using an inverted fluorescence microscope (Nikon Eclipse Ti, Nikon Corporation, Tokyo, Japan) and scientific CMOS camera (Flash4.0 V2, Hamamatsu, Japan). Particle tracking was analyzed by ImageJ (National Institutes of Health, Bethesda, Maryland, US).

Secondary glue-based mold

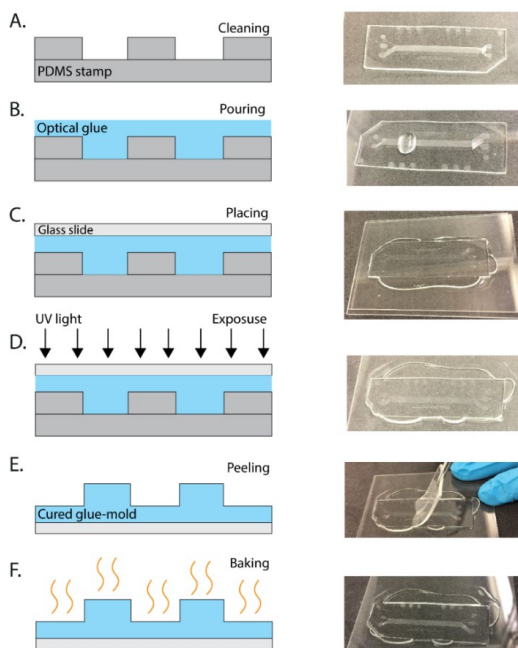


Figure 1. A fabrication process for a glue-based mold. A) Cleaning preparative step for the PDMS stamp; B) Pour glue on the PDMS surface; C) A second glass was placed on the top; D) UV exposure process; E) After the glue was cured, gently remove the first glass and peel off PDMS; F) A complete glue-based mold with micro structure replication.

The fabrication method is a one-step procedure once the PDMS replica has been prepared. After peeling off from the SU-8 master, it is important to clean the surface of the PDMS replica and ensure that no PDMS residuals or dusts are stuck inside (Fig.1A). A thin layer of UV-curable glue is poured to cover the entire microstructure (Fig.1B). Here, an additional step of removing air bubbles is sometimes required by placing a glass slide on the top (Fig.1C). In order to cure the glue it is exposed to UV light

(a recommended energy for full cure NOA63 is 4.5 Joules/sq.cm of ultraviolet light with maximum absorption in the range of 350-380nm). After approximately 30-40 minutes, 1mm glue is cured and the PDMS stamp is peeled off from the glue-mold (Fig.1E). Due to the remaining solvent or residuals on the surface, a baking step may be recommended for the glue-mold before it is ready to use in the soft-lithography process.

Additional features for the mold

Additional features are often desired on microfluidic device masters, for example, for integration with external equipment. In the SU-8 master, additional features are hard to add once it is fabricated. However, the glue-based mold is an accessible platform to integrate other parts to the device such as reservoirs or alignment pins according to the application at hand.

In a common soft-lithography procedure, a punching step right after peeling off PDMS stamps is necessary to generate inlets and outlets channels, and subsequently silicon tubes are attached to those holes by silicone glue to form the reservoirs. In the multi-hole devices, those steps may consume more time than is available and may even require additional technical skills due to the amount of inlets and outlets in a small punching space. Reservoirs built into the PDMS is a convenient way to reduce the required time for assembly and to simplify the fabrication process (Figure 4).

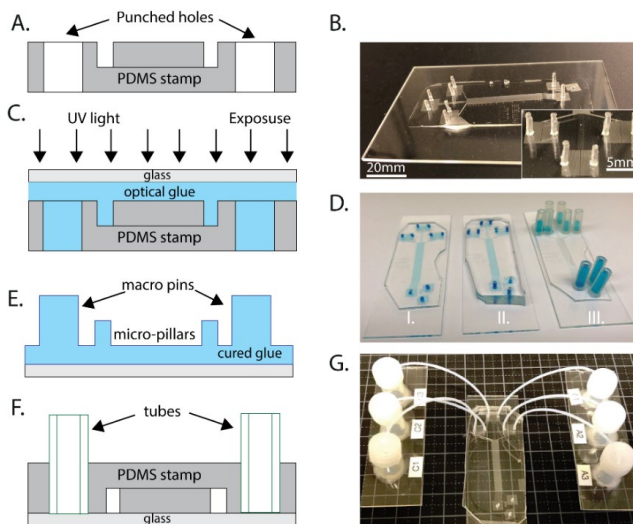


Figure 2. Macro pins for a glue-based mold procedure. A) The PDMS stamp is punched to generate a in and outlets channels. C) Pouring optical glue, then a cover of glass slide and UV light exposure for curing step. E) Cured mold includes micro-structure and macro pins. F) A complete device with tubes for the fluid connection. B) A practical glue-based mold with 6 inlets (6 pins, 1mm diameter and 5mm high). D) Three duplicated devices made from the glue-based mold (I. thin device, III. Thin device and attached reservoirs, II; Thick device without reservoirs). Three devices are tested with food color and a range of pressures for verification that the devices do not leak. G) Thick PDMS device (device III) connected to 6 sample collection.

The fabrication process requires only one extra step to prepare the PDMS replica. As an additional feature the reservoirs could be made by punching holes in the PDMS replica. After molding, those holes result in pins (macro sizes) that are hard, stable and replace completely the punching step in the final PDMS replicas made from the glue-mold.

Multiple layers for high throughput device

To align and assemble different layers, visual fiducial markers can be used. At the microscale, the process requires an optical microscopy and alignment tools (tweezers, holders, and markers) adding unnecessary practical challenges in terms of time consumption, alignment error as well as poor repeatability. Due to the exact duplication of the PDMS replicas including the holes, we demonstrate a simple process of stacking several PDMS layers together through the reference pins (Fig. 3A).

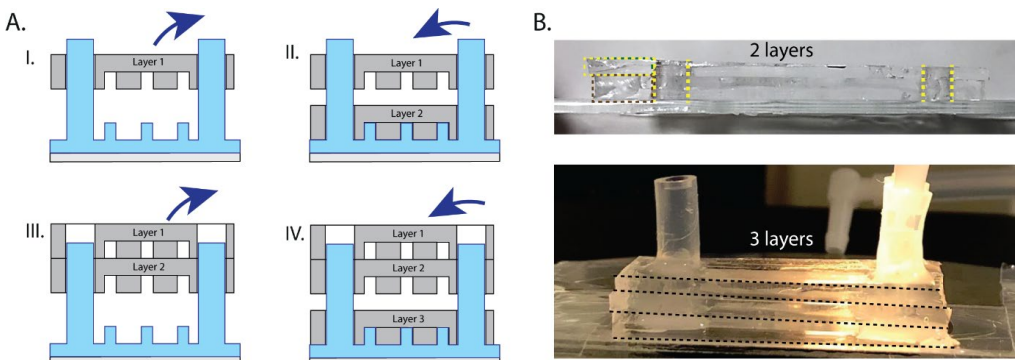


Figure 3. A new approach of stacking multiple microfluidic layers. A) Stacking process of three PDMS layers based on alignment pins. B) A two-layer device and a complete device with three layers.

The reference pins should be outside the device (with longest possible distance) to reduce alignment error. However, in this work, we use the reservoir pins as an alignment. The fabrication process is described in figure 3A. Two PDMS layers are treated by oxygen plasma and then bonded together while stacking according to the reference pins. The process is repeated until the expected number of layers are bonded completely. The final step is the bonding between the stack of device and a glass slide. Finally, reservoirs are attached using standard procedure by silicone glue as in the figure 3B.

Results and discussions

Device verification

After the soft-lithography process, a PDMS device duplicated by a glue-mold is checked under an optical microscopy to ensure that all pattern is faithfully replicated. Dimensions of features are measured with optical and scanning electron microscopy. In our experiments, different DLD microfluidic devices are fabricated and used to evaluate the reproducibility and accuracy of the technique. Figure 4 presents two typical pillar arrays (device 2 and 3 in the table 1). No pillars are missing and no pillars are damaged in the two cases.

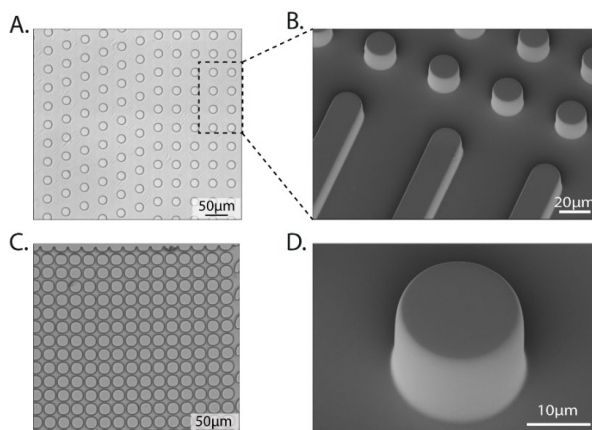


Figure 4. PDMS device verification by the optical and scanning electron microscopy. Two pillar arrays (A and C) are used to check the quality of the replication from a glue-based mold. B and D gives a better observation of pillar array and single pillar.

Secondly, the table of three devices with their calculated dimension and PDMS stamps in both of SU-8 mold and glue-mold. No significant differences are found in the measurements. Device 3 with a small gap size and dense pillars is sensitive to any size change. Its function will be verified with beads after leakage test.

Table 1. Comparison data (pillar diameter D, Gap between pillar G and pillar height h)

	Designed Dimension	PDMS replication From a SU8-mold	PDMS replication From a glue-mold
Device 1	D= 30 G= 31 h= 23	D=28.4±0.1 G=30.4 ±0.1 H=22.9	D=28.6±0.20 G=30.2 ±0.15 H=22.8
Device 2	D= 20 G= 20 h= 24	D=19.6±0.1 G=19.5 ±0.2 H=22.9	D=19.4±0.24 G=19.6 ±0.27 H=22.9
Device 3	D= 15 μm G= 3 μm h= 20 μm	D=14.7±0.1 G=2.94 ±0.1 H=19.6	D=14.8±0.13 G=2.74 ±0.17 H=19

Leakage check

The PDMS stamp is bonded to a glass slide or to a PDMS layer to form a complete microfluidic device. The leakage of sample from the device is often checked by hand using a syringe. However, for devices aimed for high flow rates, a leakage check is performed with a syringe pump. Figure 2D illustrates a typical leakage test with food color inside.

Our microfluidic devices are typically used for particle sorting. Therefore, to show proof of principle of functional devices we demonstrate sorting of particles using deterministic lateral displacement (DLD).

Particle separation and experiment repeatability

DLD is a highly precise sorting mechanism that is also very sensitive to errors in the device. If the replication is not faithfully performed it will then clearly show in the sorting results using DLD. The

behavior of different particles in the DLD device relies on the designed geometry of a pillar array. Figure 5 shows a DLD array (Device 3) which has a critical size of $1.65\mu\text{m}$ and two fluorescent particles of $1\mu\text{m}$ and $2\mu\text{m}$. As expected, the particles are completely separated through the array. The test is repeated several times successfully.

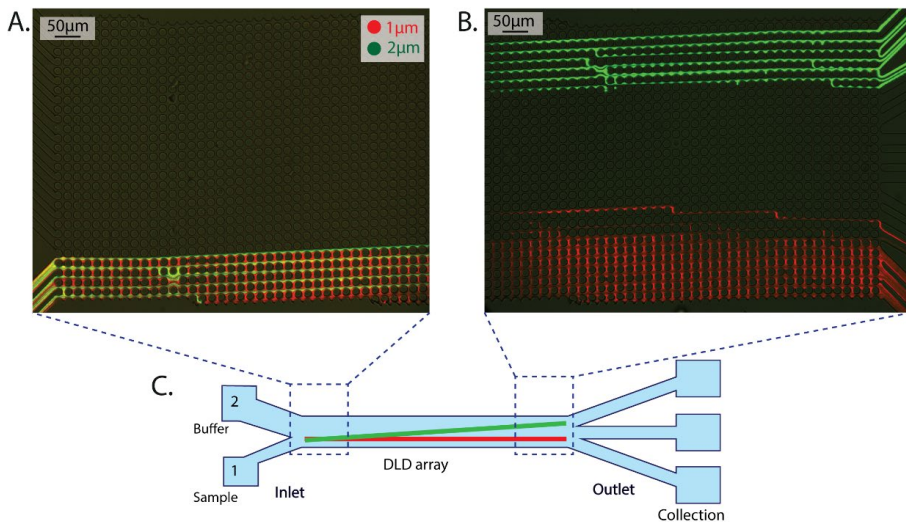


Figure 5 shows the sorting of two kinds of beads is an evidence of this attempt. The device 3 made from the glue-mold replicated from the SU-8 mold. A) The mixture of beads at the inlet showed an overlapped trajectories. B) The separation has occurred during the array and performed a clear result at the end. C) A sketch of DLD device.

Multiple layer testing

In order to facilitate high throughput microfluidic sorting organizing devices in parallel, stacking multiple device layers on top of each other is a convenient solution. With a simple approach based on reference pins, we can readily stack multiple PDMS layers in a precise alignment.

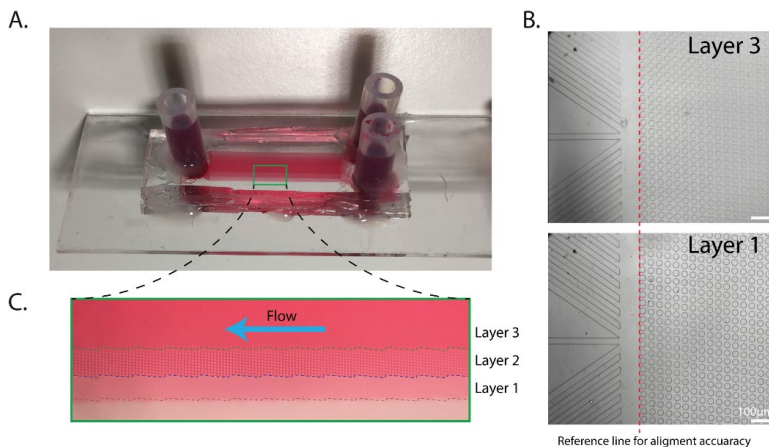


Figure 6. A complete 3-layer device. A) Leakage check with food color. B) By tilting the device 45° , three different layers of colors are observed. Images captured by cell-phone camera.

Figure 6 demonstrates an actual device with three layers. Any leakage is tested with food color to ensure the bonding efficiency. The pillar arrays of different layers are imaged by moving the sample in

the z direction in the optical microscope. A reference line identifies the small difference between layer 1 and layer 3. By merging the two images, the alignment error can be measured to less than 1 μ m and the angular error to less than 5°.

Conclusion

In this work, we successfully demonstrate a new method of making a secondary mold for PDMS replication. By considering the limits of previous work in terms of shrinkage, duplication error and anti-adhesion coating, our method not only presents high resolution duplication, but also gives more advantages of additional features and high resolution alignment. Besides, the capable of quick stacking multilayers may contribute a step forward to the high throughput for sorting applications.

Acknowledgement

This work was carried out within NanoLund at Lund University with funding from the Child Cancer Foundation (MT2013-0031), LAPASO (EU FP7 project 607350) and the Swedish Research Council (VR) grant no. 2015-05426. All device processing was conducted within Lund Nano Lab.

References

1. Manz A, Graber N, & Widmer HM (1990) Miniaturized total chemical analysis systems: a novel concept for chemical sensing. *Sensors and Actuators* 244-248.
2. Macdonal JC & Whitesides GM (2002) Poly(dimethylsiloxane) as a material for fabricating microfluidic devices. *Accounts of chemical research* 35(7):491-499.
3. Friese C, Werber A, Krogmann F, Mönch W, & Zappe H (2007) Materials, effects and components for tunable micro-optics. *IEEJ Transactions on Electrical and Electronic Engineering* 2(3):232-248.
4. Whitesides GM, Ostuni E, Takayama S, Jiang X, & Ingber D (2001) Soft lithography in biology and biochemistry. *Annu. Rev. Biomed. Eng.* 2:335.
5. Graubner V, *et al.* (2002) Incubation and ablation behavior of poly(dimethylsiloxane) for 266 nm irradiation. *Applied Surface Science* (197-198):786-790.
6. Gates BD, *et al.* (2005) New approaches to nanofabrication: molding, printing and other techniques. *Chem. Rev.* (105):1171-1196.
7. Elhadj S, Rioux RM, Dickey MD, DeYoreo JJ, & Whitesides GM (2010) Subnanometer replica molding of molecular steps on ionic crystals. *Nano Lett* 10(10):4140-4145.
8. Yang L, Hao X, Wang C, Zhang B, & Wang W (2013) Rapid and low cost replication of complex microfluidic structures with PDMS double casting technology. *Microsystem Technologies* 20(10-11):1933-1940.
9. Olmos CM, *et al.* (2019) Epoxy resin mold and PDMS microfluidic devices through photopolymer flexographic printing plate. *Sensors and Actuators B: Chemical* 288:742-748.
10. Madsen MH, Feidenhans'l NA, Hansen P-E, Garnæs J, & Dirscherl K (2014) Accounting for PDMS shrinkage when replicating structures. *Journal of Micromechanics and Microengineering* 24(12):127002.

Paper V



Tunable separation in deterministic lateral displacement by pressure control on varying PDMS stiffness

Trung S.H. Tran, Bao D. Ho, Jason P. Beech and Jonas O. Tegenfeldt *.

Division of Solid State Physics & NanoLund, Lund University, Professorsgatan 1, 22363 Lund, Sweden

(*) E-mail: jonas.tegenfeldt@ftf.lth.se

Abstract

Deterministic lateral displacement (DLD) has been widely reported as a powerful and promising technique in the field of label-free and passive separation. However, the operation of a DLD device is dependent on its fixed geometry. Therefore, fabricating a DLD device that works well with cells, which normally have rather broad and uncertain size distributions, requires considerable time and effort for optimization. To resolve this issue, we present a method to quickly verify and optimize designs, as well as repurpose devices for new samples that uses the deformability of PDMS under applied pressure to change device geometry and therefore separation behavior. Furthermore, a systematic survey of the effects of various material and device properties on the deformation of the pillars, and as a result, the critical diameters, was conducted.

Keywords: Glue-based mold, secondary mold, PDMS alignment, high throughput device

Introduction

In the field of label-free and passive cell sorting, DLD has shown much promise due to its high resolution (1, 2), capability of sorting small particles, high throughput (3) and integrability with other methods (4). The technique, which is based on laminar flow, relies on interactions between particles and a pillar array inside a microfluidic channel. In the seminal paper by Huang *et al.* (1), the authors demonstrated that particles smaller than a certain critical diameter (D_c) will follow the flow direction while particles larger than the critical size will be displaced and follow the angle defined by the array. The pillar array is characterized by pillar size, gap, and sorting angle which together define the critical diameter. The empirical equation derived by Davis *et al.* (5) has been widely used to predict D_c when designing devices.

$$D_c = 1.4GN^{-0.48} \quad (1)$$

Here, D_c is the critical diameter, G is the gap between two pillars, and N is the period of the array. The formula implies that the critical diameter is hardwired into the device and it is difficult to adapt the device to new samples. To overcome this limitation, Beech *et al.* stretched devices fabricated in PDMS during separation experiments, changing the gap G and therefore D_c (6). Stretching along the width of a device in this way increases the G (and D_c) and stretching along the length of the device decreases G (and D_c). The direction of the stretching force is in the plane of the array. In this paper, we show that also by stretching the array in the direction perpendicular to the plane of the array, we can tune the critical diameter of a DLD array. The out-of-plane stretching of the array can be achieved via a pressure difference between the inside and the outside of the DLD array, as illustrated in Figure 1. Since the pillars are stretched in the z-direction, they contract in the lateral (x and y) directions, due to the

Poisson effect, leading to an increase in gap width. According to Equation 1, this would result in an increase in critical diameter.

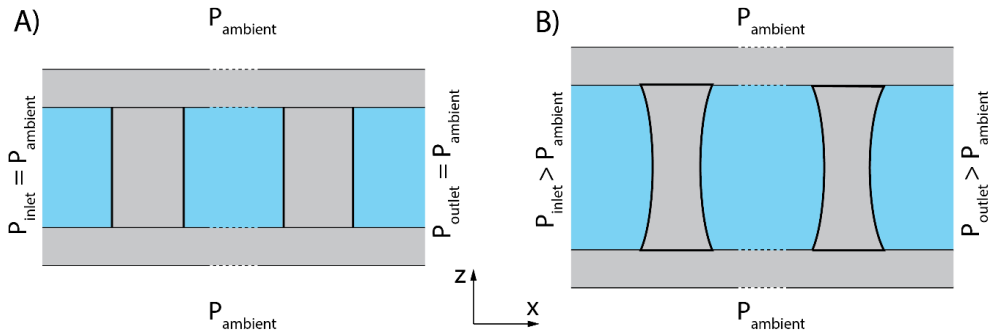


Figure 1. Mechanism of tuning D_c of DLD array using pressure (cross-section view). The pressure outside the array is the ambient pressure, while the pressure inside the array varies from P_{inlet} down to P_{outlet} . A) When the pressure inside and outside of the array are equal, the pillars and the gaps conform to the design. B) When the pressure inside is larger than the pressure outside, the pillars are stretched in z direction and compressed in x and y-direction, leading to an increase in the gap width and as a result, the critical diameter.

The stiffness of PDMS is central to our technique. In literature, it has been demonstrated that the stiffness of PDMS can be tuned from 800kPa to 1 MPa (1mm thickness of PDMS sample) (7). The result depends on mixing ratio, curing time and curing temperature. A variety of PDMS stiffness has been exploited in different applications to study cell behaviors or mechanobiology of fibroblasts (8), muscle and nerve cells (9) as well as bacterial adhesion (10). However, the effect of PDMS deformation has not been utilized in particle sorting. Figure 2 illustrates the application of our technique in tuning particle sorting in a DLD device. The device is designed so that the target particles are displaced along the DLD array, travelling from inlet 1 to outlet 5. At a high over pressure, however, due to the increase in critical diameter, the particles switch to zigzag mode and collect into outlet 3.

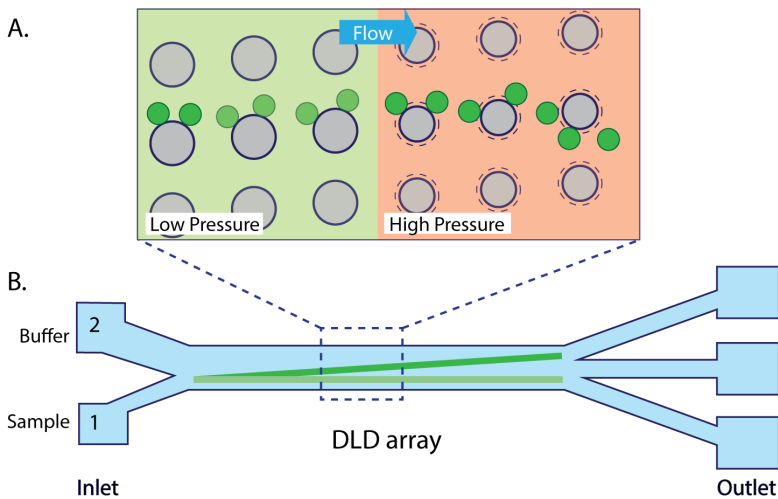


Figure 2. Application of pillar deformation in tuning critical diameter in DLD array. A) DLD array and particle trajectories at low and high overpressure. The dotted lines represent the original shape of the pillars. C) An overview of DLD device (2 inlets and 3 outlets).

The deformation of PDMS pillars in the lateral directions, as a function of mixing ratio, thickness, curing time and curing temperature, is quantified by optical measurements from the top view of the array. A variety of array geometry was investigated. Furthermore, reference particles – polystyrene beads with diameters of 5-15 μm and Young's moduli of 3-3.6 $\times 10^9\text{Pa}$ – were run in DLD devices at different applied pressures. In our setup, the inlet was connected to different overpressures while the outlet was simply exposed to the ambient. The correlation between displacement of the beads and pillar deformation was calculated to give a better understanding of the effect.

Results and discussion

Simulation result

To predict the effect of pressure on the pillar deformation, simulations were conducted. Figure 3 shows a model of a pillar array (pillar size 20 μm , height 25 μm and PDMS thickness 3mm) under low and high pressure differences between the inside and the outside of the DLD array (0.1 mbar and 100mbar). The simulation result confirms the intuitive sketch in Figure 1, showing the pillar shape changing from a perfect cylinder to a deformed cylinder with a waist when a considerable overpressure is applied inside the array. To accurately quantify the deformation of pillars as a function of the applied overpressure, a more comprehensive model which takes into account the border of the pillar is necessary.

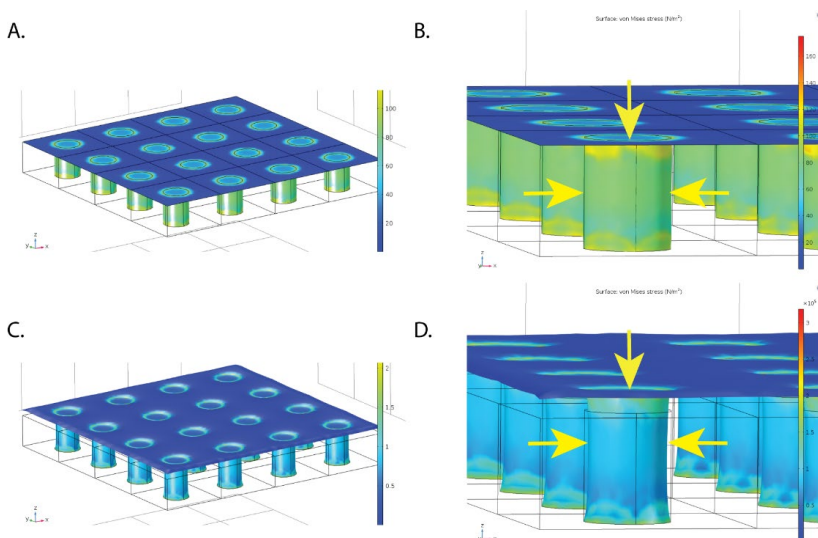


Figure 3. Simulation results of pillar deformation as a function of applied overpressure. A) & B) At the low overpressure of 0.1mbar, no deformation is visible. C) & D) At higher overpressure (100mbar), the PDMS ceiling is inflated and the pillars are stretched in z axis. As a result, the pillars shrink in the middle and the gap widths increase. Note that in all the figures, the 3-mm thick PDMS ceiling, which is out of proportion to the pillar array, has been cropped out for a better view of the geometry.

Pillar deformation

The deformation of pillars as a function of pressure difference is visible under optical microscope (Figure 4A-B). By measuring the intensity profile of the pillar and the gap at different applied pressures, the relative change of the gap width and the pillar size can be calculated (Figure 4C). According to Equation 1, an increase of critical size from the designed value, 14.5 μm (at 30mbar) to 16.9 μm (at 900mbar) is expected (Figure 4D).

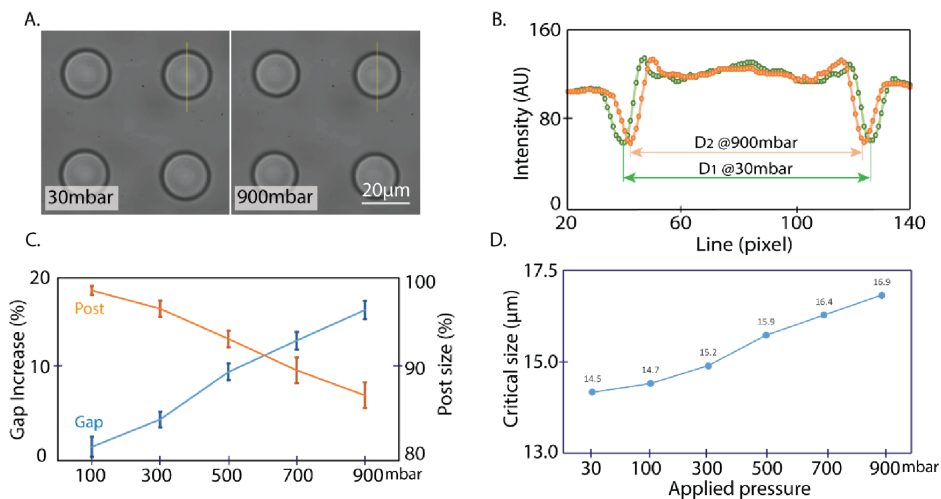


Figure 4. Optical measurement of pillar and gap change as a function of applied pressure. A) Top views of the pillars at 30 mBar and at 900 mBar. B) Intensity profiles along the yellow lines in Figure 4A. C) Percentage of pillar diameter and gap size change in relation to the applied over pressure. D) The critical sizes (diameters) calculated from the gap widths in Figure C. The experiment was conducted with 1-mm thick PDMS ceiling, mixing ratio of 10:1 and baking time of 1h at 80°C.

PDMS properties: mixing ratio and curing temperature

Using the method described above, the effect of mixing ratio, baking time, curing temperature, device length, thickness, and applied pressure on pillar deformation was also investigated.

The stiffness of PDMS and thus, the deformation of the pillars, can be controlled via PDMS mixing ratio and curing temperature. Firstly, the mixing ratio between PDMS base and PDMS curing agent was varied among 12:1, 10:1 and 8:1. An overpressure of 900mBar was applied and the change of the pillars' diameters was measured (Figure 5A). At the ratio of 10:1, which has been widely used to fabricate PDMS devices, the deformation was 12% on average. The ratio of 8:1 produces stiffer PDMS pillars with 5.5% deformation. Furthermore, as having been reported in literature, higher curing temperature makes PDMS stiffer, as shown in Figure 5B.

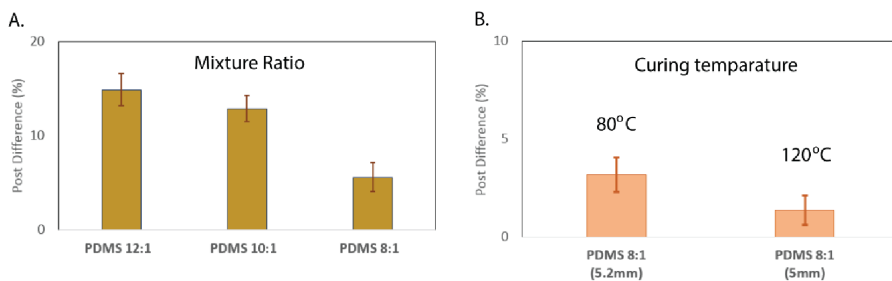


Figure 5. Pillar deformation depends on PDMS mixture ratio and curing temperature. A) Mixture ratio of 12:1; 10:1 and 8:1 were studied. B) Two curing temperatures of 80°C and 120°C were tested. An overpressure of 900 mBar was applied.

Device properties: thickness

The thickness of the PDMS ceiling above a DLD array (Figure 6A) also plays an important role in pillar deformation. As expected, a thick PDMS ceiling reduces the pillar stretching in the z-direction and as a result, reduces pillar deformation, Figure 6B.

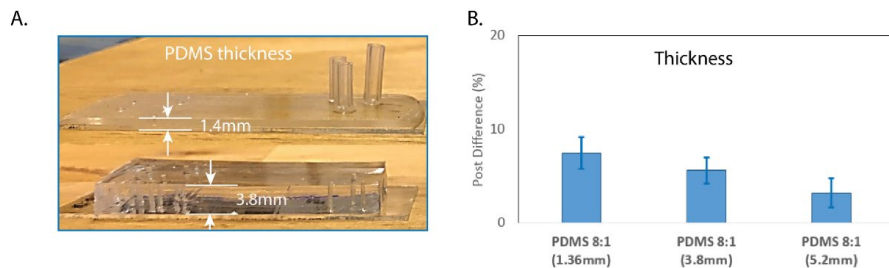


Figure 6. Effect of device thickness on pillar deformation. A) Examples of a thin and a thick PDMS device. B) Change in pillar diameter as a function of PDMS ceiling thickness. An overpressure of 900 mBar was applied.

Pressure drop and critical size change

In a typical DLD experiment, normally the outlet pressure is equal to the ambient pressure (the outlet reservoirs are simply let open to the ambient environment). In this particular setup, we observed that the deformation of pillars is dependent on their positions along the device (Figure 7A). This is because the pillar deformation is dependent on the pressure difference between inside and outside of the array. The pressure outside of the array is the atmospheric pressure while the pressure inside the array decreases along the length of the array (Figure 7B), from the applied overpressure at the inlet to the ambient pressure at the outlet. Therefore, the pillars observed at the first position in Figure 7A should be deformed more than at the middle and at the end position. This prediction is confirmed by the measured pillar size change in Figure 7C. Figure 7D shows the calculated critical diameters based on measured gap widths along the length of a DLD array. The DLD array has 13 sections, the gap widths are the same in all sections but the period is decreasing from the inlet to the outlet and as a result, the critical diameter is increasing from the inlet to the outlet (the blue line). The calculated critical diameters along the device at different PDMS mixing ratio have also been added. The DLD array molded from hard PDMS (mixing ratio of 8:1) experienced a small change in the critical diameter while the soft array (mixing ratio of 12:1) shows a higher increase in critical diameter.

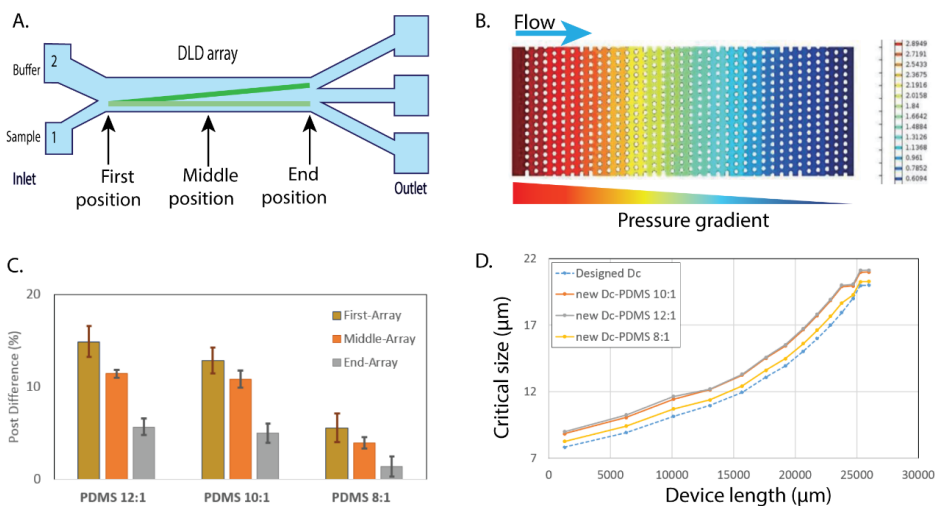


Figure 7. Pressure gradient and its effect on critical size. A) A sketch of a DLD device, the pillar measurement takes place in different positions along the length of array. B) The pressure gradient inside the array. C) The effect of position on the deformation of pillars. The effect of PDMS mixing ratio is also shown. D) The initial critical diameters and the critical diameters when running at 900mbar, at different PDMS mixing ratio.

Critical size correction in relation to pillar deformation

As mentioned in the above section, a new critical size of the array should be quoted when taking into account the deformation of the device, especially at high applied pressures. The critical diameter of a DLD device can be calibrated using reference particles. In this section, we demonstrate the calibration of the critical diameter of a deformed DLD device using hard polystyrene beads ($15\ \mu\text{m}$). The beads were run in a (relatively) hard PDMS device (mixture ratio 8:1, thickness 5.2mm and baking at 120°C in 1 hour). We use two terms to describe the size of the particles: apparent size and effective size. The apparent size of a bead is its actual size and was measured based on microscopic images capture by a high-speed camera. The effective size of the bead is calculated based on its lateral displacement at the end of the DLD array (Fig. 8C). Since in a chirped DLD device – a DLD device which has many sections, each section corresponding to a critical diameter – a particle is expected to travel in displacement mode until its diameter is smaller than the critical diameter, its lateral displacement at the outlet of the device can be used to reverse-calculate its size.

The apparent size of polystyrene beads (Young's modulus $3\text{-}3.6 \times 10^9\text{Pa}$) was expected to be insensitive to the applied pressures and was used as a control for the calibration. Their effective size, however, would reflect the change in critical diameter due to pillar deformation. At low pressure (100mbar) when the pillar deformation was small, the distributions of the effective size and the apparent size overlapped (Figure 8A). Conversely, a significant difference of those values was observed at higher pressure (900mbar) (Figure 8B). The change in critical diameter of the device was visible although all parameters in favor of stiff PDMS array had been employed. The correction of critical diameter can be done by measuring the gap width and from that calculating the new effective diameter. The matching between the apparent size and the effective size in Figure 8D confirms the validity of our calibration.

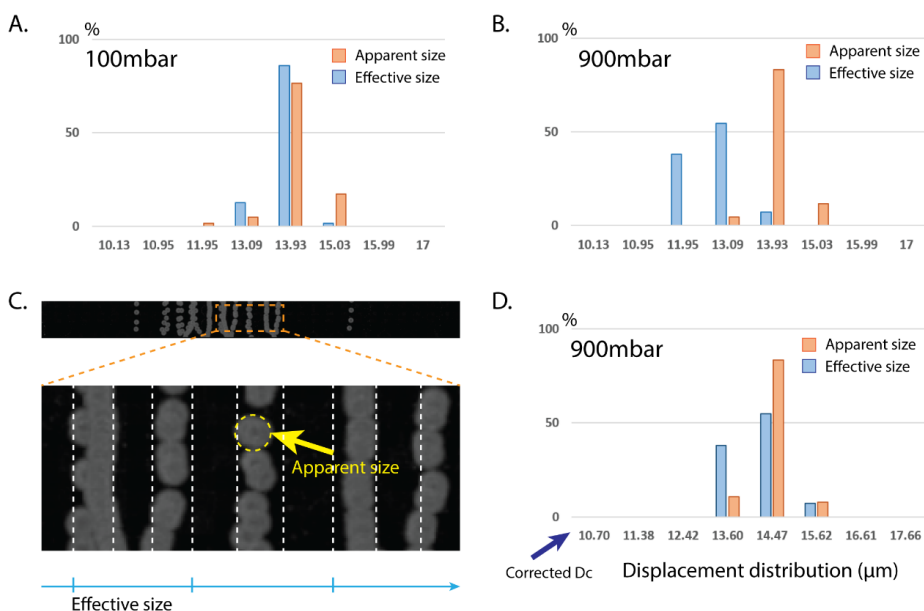


Figure 8. Comparison between effective size and apparent size to correct for the critical diameter of DLD array. A) At low pressure (100mbar), the two sizes have similar distributions. B) At high pressure (900mbar) there is a difference between those values, although all options in favor of stiff PDMS have been chosen. C) Polystyrene beads, $15\ \mu\text{m}$, was tested in a chirped DLD device (the one used in Figure 7). Apparent size of particles was extracted from optical images while effective size based on the lateral displacement and the design. D) After the critical diameter was corrected, the newly calculated effective size matched with the apparent size, confirming the validity of the correction.

Materials and instrument

The main material in this work is PDMS, a widely used soft polymer in microfluidics (Elastic modulus around 1MPa). A two liquid component kit, Sylgard 184 Elastomer, was purchased from Dow Corning Corporation, USA. The kit contains the vinyl-terminated base and methyl hydrogen siloxane curing agent. By mixing the base and the curing agent together at different ratios, we prepare the PDMS mixture for different polymer stiffnesses. The recommended ratio is 10:1 from the company data sheet and is widely used to make PDMS based microfluidics. To investigate the effect of PDMS stiffness on the pillar change, the three ratios were explored: 12:1, 10:1 and 8:1.

A SU8 mold master, which contained a DLD pattern, was coated with an anti-sticking layer. PDMS was poured on the SU8 mold and baked in 1h at 70°C. After the reservoir hole punching process, the PDMS stamp was bonded to a glass slide by oxygen plasma. The device was complete after attachment of the reservoirs tubes. A pressure controller (Fluigent) was used to precisely adjust the applied pressure.

To investigate the change of dimensions of device features on the microscale, an optical microscopy (Nikon Eclipse Ti, Nikon Corporation, Tokyo, Japan) with a high magnification object (60X) was used. For high frame rate imaging, we used an EoSens mini MC-1370 fast camera (Mikrotron GmbH, Unterschleissheim, Germany). ImageJ software, downloaded from the National Institutes of Health, was used for image analysis and the preparation of the figures.

To calibrate the device, polystyrene beads 15um with Young's modulus of $(3.3\pm 0.3)\times 10^9$ Pa (Polyscience Inc.) were used

Conclusion

In this work, a survey of PDMS stiffness as a function of PDMS mixture ratio, device thickness, curing time, curing temperature as well as the effect of pressure drop has been conducted. We show that by controlling the applied pressure, we can tune the critical size or sorting threshold in a device. The relationship between applied pressure and change in critical sizes of a device can be used for correcting the change in the size ranges for the different fractions resulting from a DLD sorting at different applied pressures. This is especially relevant for deformability-based sorting where the fractionation takes place at a wide range of pressures. The results of this work will help us decouple the effects of the deformation of the device and the deformation of the cells.

Conversely, our results can be used to minimize device deformation in order to achieve stable separation. Thick devices that are made using lower PDMS mixing ratios and cured at higher temperatures than those usually recommended by PDMS manufacturers yield stiffer devices that deform less and are therefore more stable across a range of driving pressures.

Furthermore, we propose a new way to obtain a continuously decreasing critical size by applying a relatively high pressure along a DLD device with a single critical size. This opens up for obtaining high resolution separation of particles, for example for biological applications.

Acknowledgement

This work was carried out within NanoLund at Lund University with funding from the Child Cancer Foundation (MT2013-0031), LAPASO (EU FP7 project 607350) and the Swedish Research Council (VR) grant no. 2015-05426. All device processing was conducted within Lund Nano Lab.

Reference

1. Huang LR, Cox EC, Austin RH, & Sturm JC (2004) Continuous particle separation through deterministic lateral displacement. *Science* 304(5673):987-990.
2. Wunsch BH, *et al.* (2019) Gel-on-a-chip: continuous, velocity-dependent DNA separation using nanoscale lateral displacement. *Lab on a chip* 19(9):1567-1578.
3. Louthback K, *et al.* (2012) Deterministic separation of cancer cells from blood at 10 mL/min. *AIP Adv* 2(4):42107.
4. Beech JP, Jonsson P, & Tegenfeldt JO (2009) Tipping the balance of deterministic lateral displacement devices using dielectrophoresis. *Lab Chip* 9(18):2698-2706.
5. Davis JA, *et al.* (2006) Deterministic hydrodynamics: taking blood apart. *Proc Natl Acad Sci U S A* 103(40):14779-14784.
6. Beech JP & Tegenfeldt JO (2008) Tuneable separation in elastomeric microfluidics devices. *Lab Chip* 8(5):657-659.
7. Seghir R & Arscott S (2015) Extended PDMS stiffness range for flexible systems. *Sensors and Actuators A: Physical* 230:33-39.
8. Park JY, *et al.* (2010) Increased poly(dimethylsiloxane) stiffness improves viability and morphology of mouse fibroblast cells. *BioChip Journal* 4(3):230-236.
9. Palchesko RN, Zhang L, Sun Y, & Feinberg AW (2012) Development of polydimethylsiloxane substrates with tunable elastic modulus to study cell mechanobiology in muscle and nerve. *PLoS One* 7(12):e51499.
10. Song F & Ren D (2014) Stiffness of cross-linked poly(dimethylsiloxane) affects bacterial adhesion and antibiotic susceptibility of attached cells. *Langmuir : the ACS journal of surfaces and colloids* 30(34):10354-10362.

